Evaluation of Synthetic Zeolites for Enhanced Water Adsorption in the Sabatier Reaction

J.N. Poortman

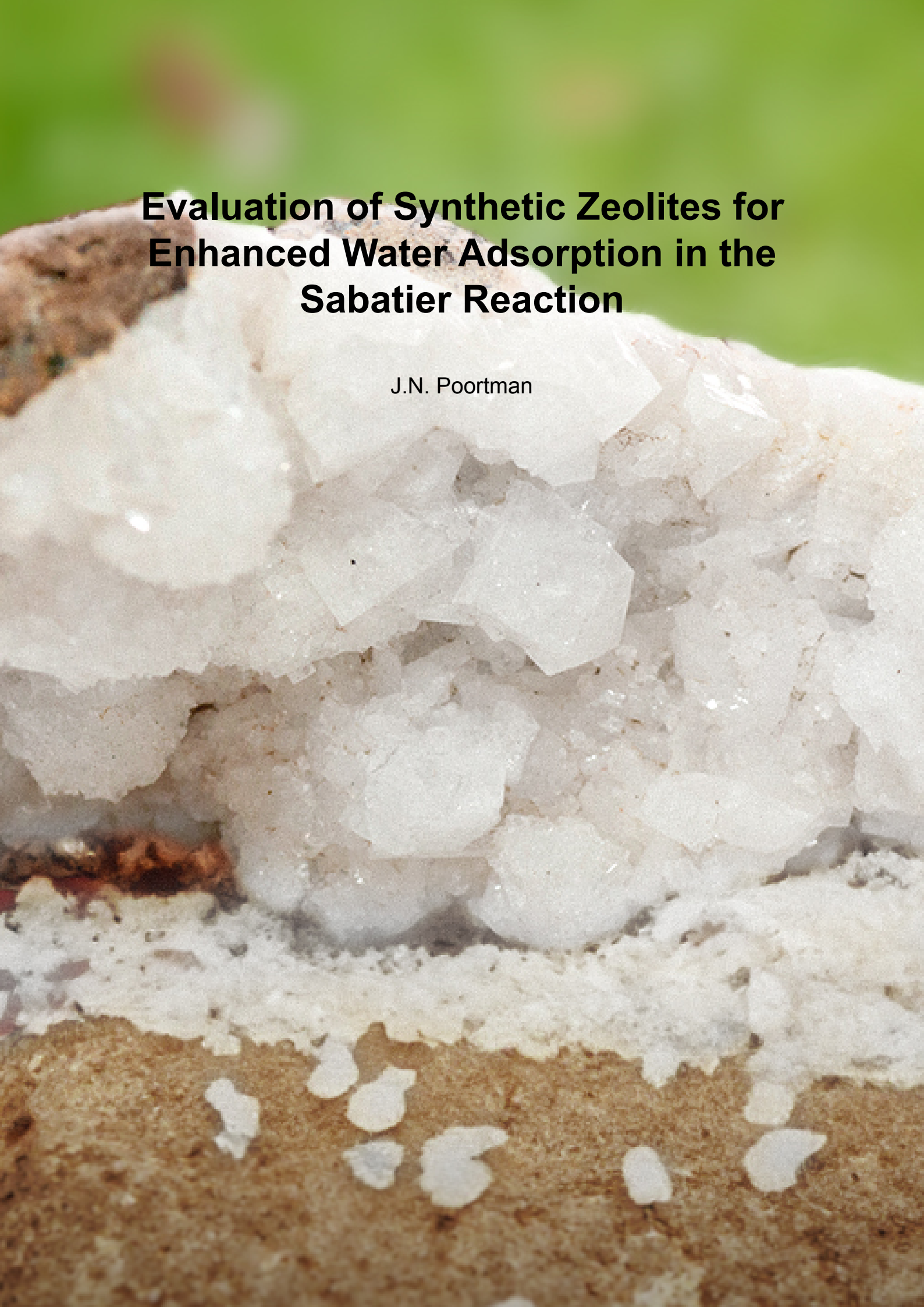

Evaluation of Synthetic Zeolites for Enhanced Water Adsorption in the Sabatier Reaction

Mechanical Engineering: Master Thesis

J.N. Poortman (6047173)

Monday 9th March, 2026

TU Delft
Delft University of Technology

Abstract

The increased emission of carbon dioxide (CO_2) derived from the use of fossil fuels has a major influence on global warming and climate change. In order to reduce these emissions, carbon dioxide can be capture from the air and converted into useful products. This can be done for example using the Sabatier reaction, in which CO_2 and hydrogen (H_2) are converted into methane (CH_4) and water (H_2O). This reaction is reversible and it is therefore desirable to adsorb the water to shift the reaction equilibrium to the product side, applying Le Chatelier's principle. Water adsorption is achieved using zeolites, which are hydrated minerals with an open crystal structure. There are many zeolite types, both natural and artificial. This study will focus on determining which zeolite type is the most suitable for water adsorption in the Sabatier reaction at relevant process circumstances and which properties account for this superior performance.

The software RASPA is used to carry out simulations that determine the amount of adsorption of each of the components in the Sabatier reaction in a certain type of zeolite. The simulations are conducted at two different temperatures, namely 455 K and 635 K, and at pressures ranging from 10 to 50 bar. Monte Carlo simulations with the grand-canonical ensemble are applied. The software Zeo++ is used to determine the inaccessible pores per zeolite and RefProp is used to determine the correct fugacity coefficient of each component at a given temperature and pressure. This is done in combination with the equilibrium constant, which is used to calculate the gascomposition of the mixture. At T = 455 K, the zeolites are simulated again with a higher Si/Al ratio. In order to keep the framework neutral, sodium cations are distributed in the zeolite. The zeolites that are examined are selected and divided into categories based on their similarities to the zeolite type FAU and whether they have large in- or external pores. The simulated zeolite types are FAU, JSR, BOZ, SBT, EMT, SAO, SBE, SBS, IRR, ITT, BPH, AFY, AFR and BEA.

To determine the most suitable zeolite, the adsorption of water as well as the co-adsorption of the other components is examined. Additionally, the enthalpy of adsorption is used to give an indication of the desorption capabilities of the zeolite.
The adsorption isotherms of each zeolite show that an increase in pressure increases the water adsorption capacity. An increase in temperature decreases the adsorption capacity. An Si/Al ratio in the range of 15-25 shows a rapid increase in the water adsorption capacity for all zeolites compared to the frameworks without aluminum. Zeolites that have large cavity diameters, large accessible pore volumes and many cages connected with large channels have the highest water adsorption capacity. In this study, these zeolites are FAU, EMT, JSR, IRR and SBS, where FAU has the highest water adsorption capacity of those five types, which is 174 g/kg-framework at 455 K and 50 bar. Co-adsorption of methane is low for each zeolite compared to the water adsorption and the adsorption of carbon dioxide and hydrogen is negligible. Additionally, all zeolites have an enthalpy of adsorption that indicates that desorption is possible. It does not seem to be crucial for adsorption capacities whether zeolites have internal or external pores. In conclusion, a zeolite with many large cages connected with large channels, a high accessible pore volume and an Si/Al ratio between 15-27 is likely to have a high water adsorption capacity. High pressure and low temperature will further enhance the adsorption.

Acknowledgement

This Master's thesis would not have been successfully conducted if it weren't for certain people who helped me along the way. I would therefore like to give my acknowledgment to all these people who helped me conduct and complete this research.
Firstly, I want to thank my supervisors Thijs Vlugt and Wiebren de Jong, for giving me the opportunity to work on this interesting topic and for their assistance and guidance along the way. Their knowledge on numerous topics in this research has been of the utmost importance to me, and I would not have been able to complete this research if not for their help. I also want to thank Lorenzo Botto for assisting them in the Assessment Committee.
I also want to express my gratitude to Shrinjay, Darshan and Jelle for helping me install RASPA and showing me how to use it. RASPA was essential for conducting the simulations, so their help and instructions have been crucial for this research. Additionally, I want to thank Eric for his help with Zeo++. This was necessary for making the simulations more realistic, so I am thankful that he showed me how to install and use this program. I also received useful feedback on my code in RASPA from David Dubbeldam, for which I am also very grateful.
Furthermore, I would like to give a shout out to the teachers at TU Delft who helped me combine my courses with my full-time job. I really appreciate their efforts at making this possible for me.
I also want to thank my family and friends for their support and for believing in me, with a special thanks to my loving fiancé Stefan. He has always supported me and shown me that he is proud of what I have accomplished, and I would not have been able to do this without him.
Last but not least, I want to thank God for the possibilities that He gives me and the strength and intelligence to take them on. Everything that I have accomplished, I have accomplished because of Him.

Contents

List of Figures

List of Tables

Nomenclature

Latin Symbols

ΔU	Energy change [J]
f	Fugacity [bar]
f^o	Standard fugacity [bar]
H	Enthalpy [kJ/mol]
k	Binary interaction parameter [-]
k_B	Boltzmann constant [1.381 $\cdot 10^{-}23$ J/K]
N	Number of particles [-]
n	number of moles [mol]
P	Pressure [bar]
P_c	Critical Pressure [bar]
P_{delete}	Probability of deleting particle [-]
P_{insert}	Probability of inserting particle [-]
q	Particle charge [C]
R	Universal gas constant [8.314 J/K· mol]
r	Particle radius [Ä]
T	Temperature [K]
T_c	Critical Temperature [K]
U_{Coulomb}	Electrostatic energy [J]
U_{LJ}	Lennard-Jones potential [J]
V	Volume of simulation box [m^3]
V_m	Molar volume [m^3/mol]
x	Amount of moles converted [mol]
y	Mole fraction [-]
Z	Compressibility factor [-]
z	Amount of moles converted [mol]
Å	Ångstrom [10·10^{-10} m]

Greek Symbols

β	$1/kT$ [1/J]
ϵ	Minimum energy of Lennard-Jones potential [J]
ϵ_0	Electric constant [8.854 $\cdot 10^{12}$ F/m]
μ	Chemical potential [J/mol]
μ^o	Standard chemical potential [J/mol]
ν	Stoichiometric coefficient [-]
ω	Acentric factor [-]
ϕ	Fugacity coefficient [-]
σ	Particle size [Ä]

1 Introduction

1.1. Context

On an annual basis, 35 billion tons of carbon dioxide (CO_2) are released into the atmosphere of the Earth due to human impact [32]. Since the start of the industrial revolution in 1760, the amount of carbon dioxide in the atmosphere has risen from roughly 280 to 425 parts per million [38]. After the invention of the combustion engine in the late 19th century, the emitted CO_2 started to increase even more rapidly.
CO_2 is a greenhouse gas and has a major influence on global warming and climate change. The increase of atmospheric CO_2 has led to a global temperature rise of nearly 1.2 °C [30]. This temperature rise can have catastrophic consequences for many ecosystems and drastically change life on Earth.

Fortunately, many sustainable inventions have been realized and applied in industries to reduce their CO_2 emissions. However, for certain industrial sections, such as aviation and shipping, it is challenging to reduce CO_2 emissions without compromising on efficiency or simply because sustainable alternatives are infeasible with a system. These industries rely heavily on fossil fuels, for example for internal combustion engines and gas turbines. Environmental friendly alternatives, such as electric engines or the usage of hydrogen, are not suitable for all applications without drastically changing a design or losing on efficiency.

To prevent the CO_2 these industries exhaust from being released into Earth's atmosphere, CO_2 capture for storage or utilization can be applied. In this method, CO_2 is captured from the air and either stored directly or converted into other products which are stored or used for other purposes. This way, CO_2 cycles are either neutralized or negative, consequently preventing more CO_2 release into the atmosphere.

A method to convert CO_2 into useful products is the Sabatier reaction. This reversible reaction converts CO_2 and hydrogen (H_2) into methane (CH_4) and water (H_2O) using for example a nickel (Ni) catalyst [18]. The produced methane can be used for other applications, such as natural gas and hydrogen production [42]. To prevent the reverse reaction from occurring, it is necessary to adsorb the water and shift the reaction equilibrium to the product side. This can be achieved by using a hydrophilic zeolite [18]. Although there are many types of zeolites, only some of the most common types are studied in combination with the Sabatier reaction. Furthermore, knowledge on beneficial zeolite properties or design for water adsorption as well as co-adsorption is limited. This knowledge is required to determine the most suitable zeolite for the Sabatier reaction and consequently convert the highest amount of CO_2.

1.2. Background information

This section of the report gives a short description of important terms and concepts that are used in the study, namely the Sabatier reaction, zeolites and Monte Carlo simulations.

1.2.1. The Sabatier reaction

This study focuses on the Sabatier reaction. This reaction converts CO_2 into methane according to the following reaction:

$$CO_2 + 4\ H_2 \leftrightarrow CH_4 + 2\ H_2O \tag{1.1}$$

The Sabatier reaction is a reversible and exothermic process. The enthalpy change is equal to [36]:

$$\Delta H = -165 \text{ kJ/mol}$$

The reaction takes place at elevated temperatures and pressures around 573 - 673 K and 20-30 bar, respectively [52]. Several types of catalysts can be used for the reaction, such as nickel, ruthenium or bimetallic catalysts. Ni-based catalysts are the most widely used for the Sabatier reaction due to their low cost and high activity [46].

The Sabatier reaction is used for many applications, for example on board the International Space Station. The CO_2 the astronauts exhale is used for the reaction to produce drinkable water and methane for heating and rocket propellant [40]. Additionally, the Sabatier reaction can be used to convert excess renewable energy, such as hydrogen, into methane, which is suitable for storage and transportation through existing natural gas infrastructures.

As mentioned before, the Sabatier reaction is a reversible reaction. To prevent the products from converting back to CO_2 and H_2, the reaction equilibrium needs to shift to the product side. This can be achieved by changing the conditions according to Le Chatelier's principle, which states that the position of equilibrium will shift to counteract the changing conditions and restore a new equilibrium [50]. By adsorbing (part of) the produced water in the Sabatier reaction, the equilibrium will shift to the product side to counteract the change in the amount of water by producing more water and restore equilibrium. This concept is explained further in Chapter 2.1.4.

1.2.2. Zeolites

The water on the product side of the Sabatier reaction can be adsorbed using a zeolite. Zeolites are hydrated aluminosilicate minerals consisting of silicon (SiO_4) and aluminum (AlO_4) [58]. They are solids with a relatively open crystal structure. This structure is a tetrahedral framework with an oxygen atom shared by two tetrahedra, which can either be silicon or aluminum. The Silicon/Aluminum (Si/Al) ratio differs per zeolite. The presence of aluminum creates a charge imbalance that requires the presence of other metal ions to restore this imbalance. Natural zeolites usually contain mono- or di-valent ions such as magnesium, calcium or sodium [10].

Zeolites can form different crystalline structures with large cavities. There are roughly 40 natural zeolites, one of which can be seen in Figure 1.1, and 150 artificial, synthetic zeolites [58]. Zeolite types are denoted using a three-letter code, as shown in Table 1.1. The zeolites in this table are a selection of the 150 artificial zeolites that will be examined in this study. As the table shows, the selection is based on zeolites that have properties similar to the zeolite type FAU and types that have large internal or external pores. Chapter 3.3 elaborates further on why these are the reasons these zeolites are selected for the study.

Figure 1.1: Natural zeolite Chabazite [55]. Zeolites have a crystal-like appearance on the inside. The size of the zeolite in the picture is 72x54x30 mm.

Table 1.1: Zeolite types for which the adsorption isotherms will be generated with simulations. The table shows the total volume, accessible pore volume, largest cavity diameter and restricting pore diameter for each zeolite.

Zeolites	Vol. [Å^3]	Access. Pore Vol. [cm^3/g]	Largest Cavity D. [Å]	Restrict. Pore D. [Å]
Similar FAU				
FAU	14428.771	0.3723	10.696	6.950
BOZ	7112.097	0.3558	8.305	4.518
JSR	7815.473	0.4221	7.431	4.542
SBT	10501.091	0.3410	10.397	6.944
Int. pores				
AFR	2109.810	0.2618	7.816	6.573
BEA	4178.433	0.2716	6.118	5.634
Ext. pores				
AFY	1132.679	0.3380	7.422	5.502
BPH	1914.802	0.3023	9.108	5.614
IRR	4422.866	0.4838	13.915	11.716
ITT	3586.511	0.4094	12.771	11.602
In- and ext. pores				
EMT	7207.302	0.3711	11.001	6.967
SAO	3948.063	0.3371	8.206	6.298
SBE	9320.777	0.3386	12.097	6.835
SBS	6997.151	0.3422	10.977	6.867

The properties of the zeolites in Table 1.1 can be described as follows:

- **Volume**: Total volume of the unit cell.
- **Accessible pore volume**: Volume of the zeolite that is accessible to other components. It thus specifies how dense a zeolite is and how much open space it has.
- **Largest cavity diameter**: The diameter of the largest cavity in the zeolite. The cavities are cage-like spaces in the zeolites that are larger than its channels.
- **Restricting pore diameter**: The largest pore diameter through which a molecule can enter the zeolite. If this diameter is smaller than the size of the molecule, the molecule cannot enter the zeolite and will therefore not be adsorbed.

The cage-like framework of zeolites makes them suitable for adsorption of molecules, such as water. They can also exchange their metal ions for other positively charged ions, which is known as cation exchange. The large cavities allow for smaller molecules to pass through while trapping larger ones. For this reason, zeolites are sometimes used as molecular sieves [58].
Additionally, zeolites have certain properties that make them attractive for usage in the aforementioned applications. They have high melting points (around 1900 K [9]) and can resist high pressures. They do not dissolve in inorganic solvents or water or oxidize in air. In addition, they are highly unlikely to have a harmful environmental impact since they are based on natural minerals [58].
The International Zeolite Association (IZA) has a database of zeolite structures where information can be found on the framework types that have been approved by the Structure Commission (IZA-SC) [3].

1.2.3. Monte Carlo simulations

Adsorption of components in a zeolite can be examined experimentally. However, examining this for a large number of zeolites is time-consuming and requires acquiring samples of each of the zeolite types to be examined. It is more efficient to test the adsorption in zeolites with numerical simulations. A computer simulation calculates the adsorption loading based on information on the zeolite structure, components, thermodynamic laws and properties. Certain numerical methods are not time-dependent, which makes it much faster to acquire the equilibrium situation in the zeolite and the associated adsorption loading in contrast to experimental methods.

An example of a time-independent numerical simulation is the Monte Carlo (MC) simulation. MC simulations are a powerful method to determine macroscopic properties of a system, such as pressure or energy, using microscopic properties [23].
A system consisting of many molecules has an extremely high number of possible configurations. For each configuration, the macroscopic properties can be determined, for example by using the Lennard-Jones potential. The average of all the configurations is the value of this property for this particular system. However, it is impossible to calculate this for all the possible configurations, since the necessary computing power is simply not available [23]. Additionally, not all configurations are equally likely to occur, depending on the energy of each configuration. Configurations with a low energy are more likely to occur than configurations with high energy [19]. In a Monte Carlo simulation, only the most likely configurations are considered and their properties determined.

Multiple ensembles can be used with MC simulations, such as the NVT-ensemble (canonical ensemble), which keeps the number of molecules, volume and temperature constant. This is for example suitable for a non-isolated, closed system. Another ensemble is the NPT-ensemble (isobaric-isothermal ensemble), which keeps the number of molecules, pressure and temperature constant and is for example suitable for systems with fluctuating volume.
For adsorption in a zeolite, the μVT-ensemble, also known as the grand-canonical ensemble, is the most suitable [34] [23]. This ensemble keeps the chemical potential, volume and temperature constant. Using this ensemble, the zeolite is simulated as a box in which molecules can be inserted or removed. An implicit reservoir mimics the bulk gas, in which all components are at equilibrium. For the bulk gas and zeolite to be in equilibrium, the chemical potentials of both bulk gas and adsorbed gas have to be equal and the components in the zeolite are also in chemical equilibrium [23]. This concept is shown in Figure 1.2. Chapter 3.4 explains this further.

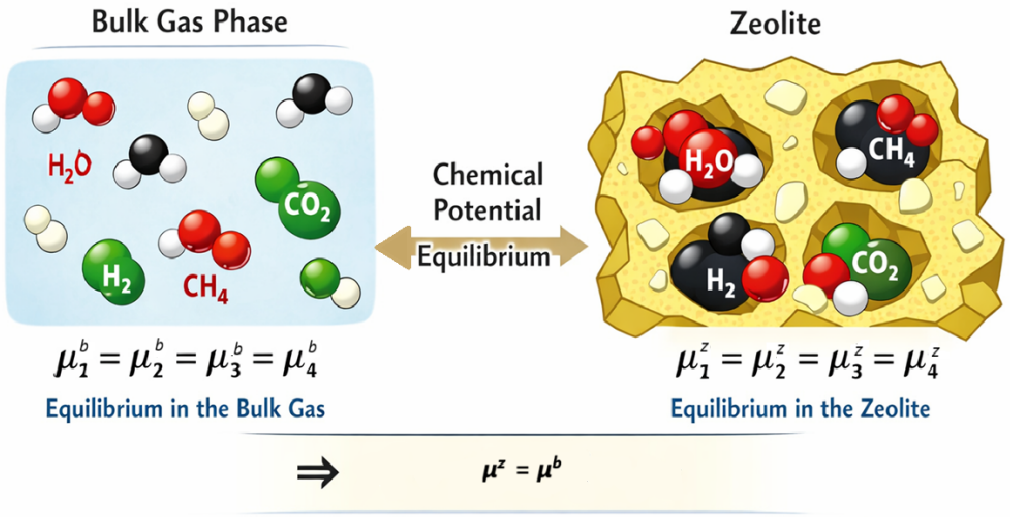

Figure 1.2: Adsorption equilibrium between zeolite and bulk gas leading to chemical equilibrium between the components in the zeolite using the μVT -ensemble.

The simulation will insert or remove molecules from the zeolite to get to this equilibrium. The simulation is conducted according to the following steps:

- The fugacity, and therefore chemical potential, of the bulk gas is determined using the fugacity coefficient ϕ:

$$f = \phi P \tag{1.2}$$

$$\mu = \mu^o + RT \ln(\frac{f}{f^o}) \tag{1.3}$$

Fugacity is an effective partial pressure, which is used for real gasses instead of ideal gasses. Fugacity is equal to the pressure of an ideal gas at the same Gibbs free energy and temperature as the real gas. For an ideal gas, fugacity and pressure are equal and therefore ϕ = 1. Appendix B shows how the fugacity coefficient for a component in a mixture can be calculated using the Peng-Robinson Equation of State.

- The energy of the current configuration is calculated in the simulation. This energy is equal to:

$$U_{\text{total}} = U_{\text{LJ}} + U_{\text{Coulomb}} \tag{1.4}$$

In which U_{LJ} is the Lennard-Jones potential, given by [12]:

$$U_{\text{LJ}}(r) = 4\epsilon[(\frac{\sigma}{r})^{12} - (\frac{\sigma}{r})^{6}] \tag{1.5}$$

The electrostatic energy $U_{\text{Coulomb}}(r)$ is given by [27]:

$$U_{\text{Coulomb}}(r) = \frac{q_i q_j}{4\pi\epsilon_0 r} \tag{1.6}$$

This energy is determined using the interaction between all components in the bulk gas.

- A molecule is randomly inserted into the zeolite and the energy change ΔU due to the insertion is calculated.
- The move is accepted according to the following probability [23]:

$$P_{\text{insert}} = \text{min}(1, \frac{fV}{(N+1)}\text{exp}[-\beta\Delta U]) \tag{1.7}$$

- The same is done for the removal of molecules from the zeolite, according to the probability [23]:

$$P_{\text{delete}} = \text{min}(1, \frac{N}{fV}\text{exp}[-\beta\Delta U]) \tag{1.8}$$

- These steps are repeated for a large number of cycles. Consequently, the system settles into a state that corresponds to the fixed μ. The box and reservoir are now in equilibrium.
- The output of the simulation gives the number of molecules that are adsorbed into the zeolite, which can be used to plot an adsorption isotherm for multiple fugacities.

Equations 1.7 and 1.8 show that the energy change of a move and the fugacity of the system determine whether insertion or removal of a molecule from the zeolite is either rejected or approved. In case the energy change after a move is negative, the exponential will be larger than 1, so the move is always accepted. When the energy change is positive, the value of the exponential term decides the probability that this move is accepted or rejected. This equation resembles reality, since a system will want to convert to lower energy states, so moves that decrease the energy are always favorable.

This MC simulation uses the concept of detailed balance. This implies that the rate of transitions between two states is equal to each other, so the probability of being in state A and switching to state B is equal to the probability of being in state B and switching to state A [23]. Although detailed balance is not strictly necessary to have a correct sampling, using it will ensure that the sampling is correct.
The software RASPA will be used in this research to conduct the MC simulations using the grand-canonical ensemble.

2
Literature Review

This chapter reviews previous research and analyses the research gap that follows from this review. The thesis framework, including the objective, research questions and scope, will also be discussed.

2.1. Previous research

Several studies have been conducted to improve certain aspects of the Sabatier reaction in combination with a zeolite. The following section gives a brief overview of potentially relevant studies for this research.

2.1.1. 13X and 5A zeolites

Delmelle et al. (2016) discovered that the zeolite framework 5Ni/13X showed improved performance (135% at 300 °C) compared to 5Ni/5A and can be operated nearly three times longer when pre-dried under an oxidizing atmosphere. This is most likely due to the larger pores that allow for better water and air transport [18].
Wei et al. (2020) performed a study to examine if modification with nickel and/or ruthenium (Ru) of 5A and 13X zeolites improved the methanation and adsorption process. When considering conversion, this study concluded that 13X outperforms 5A zeolites. Adding ruthenium does not improve CO_2 methanation, but a pure Ru catalyst does increase the selectivity of 13X zeolites and decreases selectivity for 5A zeolites [56].
Wei et al. (2021) concluded in a successive study that Ni precursors have an influence on the performance of 13X and 5A zeolites. The 13X zeolite with a nickel citrate modified catalyst showed high activity and selectivity towards methane and the catalyst is stable under the experimental circumstances [57].

2.1.2. Zeolite & reaction properties

Li et al. (2021) conducted a study on the adsorption and desorption characteristic of hydrophobic zeolites. This study concluded that a low Si/Al ratio increases the hydrophilic capacity of a zeolite, while a high Si/Al ratio increases the hydrophobic capacity [37].
The shape selectivity of zeolites is studied by Sharma et al. (2024). This study shows that the shape of a zeolite has an impact on the hydroisomerization of linear alkanes, especially when concerning cage or channel-like structured zeolites. Additionally, zeolites favor certain isomers less or more than others for adsorption [51].
Grevil (2020) uses grand-canonical Monte Carlo simulations in RASPA to determine the NO_x gas mixture adsorption in five different zeolites, namely FAU, FER, MFI, MOR and TON. FAU showed the highest adsorption loading for all NO_x components due to a high specific volume and number of pockets. Before the GCMC simulation was carried out, the inaccessible pockets in FAU and FER were determined and blocked to avoid incorrect adsorption in these pockets [13].
As mentioned in chapter 1.2.1, the Sabatier reaction takes places at 573 - 673 K. However, high temperatures negatively influence desorption. Liangyuan Wei et al. (2021) show that a temperature of 453 - 633 K can be applied when using zeolites that have catalytically active metal, such as Nickel, directly loaded onto them. This lower temperature enhances the adsorption of components onto the zeolite [57].

2.1.3. Pore size

Granitsiotis (2017) proved that the amount of nickel catalyst on the surface of the zeolite influences the performance of the reaction. The two examined zeolites were 3A and 4A, and from the experiment it followed that smaller catalyst pellets in combination with larger-pore zeolites (4A) increase and stabilize conversion rates, since the nickel catalyst manages to get further inside the zeolite pores compared to 3A [29].
Azad (2020) studied the sorption enhanced methanation for large-pore zeolites. Zeolite L was examined in comparison with zeolite 5A and 13X. The experiment showed that the zeolite L activity is in between the 5A and 13X activity, despite the larger pore size. A possible explanation for this would be the higher Si/Al ratio of zeolite L, which increases the hydrophobic capacity of a zeolite. Furthermore, it was found that zeolite L does not show significant sorption enhancement after catalytic impregnation, whereas 5A and 13X do show improved sorption enhancement. Azad (2020) indicates that this might be due to non-optimal circumstances with regards to pressure and temperature for zeolite L, which causes it not to adsorb water properly [4].
Van Kampen (2021) examined the properties of 3A (LTA) zeolites as part of a study on efficient carbon utilization to DME by steam adsorption enhancement. 3A shows adequate adsorption capacities for water, since the small pore size of 3A (2.9 Å) excludes many components from being adsorbed, such as CO2 (3.4 Å) [31].

2.1.4. Equilibrium constant

The equilibrium constant K of a chemical reaction denotes the ratio between reactants and products and shows whether a reaction under certain conditions favors the products (large K) or the reactants (small K). As explained in chapter 1.2.1, the goal of adsorbing water from the products is to shift the reaction equilibrium towards the product side. The effect of water adsorption on the reaction is shown by Granitsiotis (2017) [28]. The equilibrium constant K for an ideal gas ($\phi = 1$) is calculated as follows [43]:

$$K = \frac{y_C^{\nu_C} y_D^{\nu_D}}{y_A^{\nu_A} y_B^{\nu_B}} \left(\frac{p}{p_{\text{ref}}}\right)^{\nu_C+\nu_D-\nu_A-\nu_B} \tag{2.1}$$

With p_{ref} = 1.01325 bar. Using the stoichiometric Sabatier reaction (Equation 1.1), the amount of mole for each component on the product side can be expressed using x, where x denotes the amount of methane produced:

$$\mathsf{n}_{\mathsf{CO_2}} = 1 - x$$
$$\mathsf{n}_{\mathsf{H_2}} = 4 \cdot (1 - x)$$
$$\mathsf{n}_{\mathsf{H_2O}} = 2 \cdot x$$
$$\mathsf{n}_{\mathsf{CH_4}} = x$$
$$\mathsf{n}_{\mathsf{tot}} = \mathsf{n}_{\mathsf{CO_2}} + \mathsf{n}_{\mathsf{H_2}} + \mathsf{n}_{\mathsf{H_2O}} + \mathsf{n}_{\mathsf{CH_4}} = 5 - 2x$$

And for the mole fractions:

$$y_{\mathsf{CO_2}} = \frac{1 - x}{\mathsf{n}_{\mathsf{tot}}}$$
$$y_{\mathsf{H_2}} = \frac{4 \cdot (1 - x)}{\mathsf{n}_{\mathsf{tot}}}$$
$$y_{\mathsf{H_2O}} = \frac{2 \cdot x}{\mathsf{n}_{\mathsf{tot}}}$$
$$y_{\mathsf{CH_4}} = \frac{x}{\mathsf{n}_{\mathsf{tot}}}$$

In equation 2.1, A & B indicate the reactants CO_2 & H_2 and C & D indicate the products CH_4 & H_2O, respectively. This means that ν_A = 1, ν_B = 4, ν_C = 1 and ν_D = 2.

Inserting this in equation 2.1 and rewriting gives:

$$K = \frac{4x^3(5-2x)^2}{(1-x)(4-4x)^4} \cdot \frac{P_{\text{tot}}}{P_{\text{ref}}}^{-2} \tag{2.2}$$

Using the partial pressure of water, the following is applied:

$$\frac{P_{H2O}}{P_{tot}} = y_{H_2O} = \frac{2x}{5-2x}$$

Inserting this in equation 2.2 and rewriting gives:

$$K = \frac{x(\frac{P_{H2O}}{P_{\text{tot}}})^2(5-4x)^4}{(1-x)(4-4x)^4(1-\frac{P_{H2O}}{P_{\text{tot}}})^4} \cdot \frac{P_{\text{tot}}}{P_{\text{ref}}}^{-2} \tag{2.3}$$

Since K is fixed, reducing the partial pressure of water needs to be compensated by increasing x and thus the reaction equilibrium is shifted towards the product side, which proves that water adsorption enhances CO_2 conversion in the Sabatier reaction [28].

2.1.5. Adsorption isotherms

Multiple works have determined adsorption isotherms of several zeolites with several adsorbed components at various pressures and temperatures. Even though the simulation- or experimental properties are not completely similar to the ones used in this research, it is important to check for certain trends that are to be expected.
In various papers it can be seen that the adsorption of components increases as pressures increases. Additionally, it is expected that the adsorption decreases as temperature increases. For example, in Gholipour et al. [26] it is seen that both the adsorption of CO_2 and CH_4 on zeolite FAU increases as the pressure increases from 0 to 10 bar. Also, the adsorption capacity decreases as the temperature increases from 273 to 323 K. The same trend is shown in García-Sánchez et al. [25], where the adsorption isotherms of CO_2 on FAU are computed using both experiments and simulations. This also shows an increase in the adsorption as pressure increases from 0 to 100 kPa. Again, the temperature increase from 253 to 303 K causes an adsorption decrease. This trend is also seen on different zeolites, such as LTA in Duan et al. [20], where the adsorption of CO_2 increases as pressure increases form 0 to 4 MPa, whereas the adsorption decreases as temperature increases from 278 to 328 K. Water shows the same trends according to Zhang et al. [59], where the adsorption of water on MFI zeolites increases as the pressures increases.

The simulation properties of this research differ from ones in the discussed literature. However, the trends that are seen for the adsorption isotherms regarding pressure and temperature are also expected in the results from this research.

2.2. Research gap

Section 2.1 shows that several studies have been performed on adsorption of certain components in the presence of a zeolite. This previous research indicates that several factors contribute to the suitability of a zeolite for adsorption, such as pore size, Si/Al ratio, shape, reaction conditions, inaccessible pockets and the location and amount of the nickel catalyst on the surface and the inside of the zeolite. It should be noted that the majority of these studies focuses on only a few types of zeolites, mainly 13X (FAU) and 5A (LTA). These zeolites belong to the synthetic zeolite groups A and X, which are widely known and used for many applications [41]. However, it is not proven that these types are the most suitable in combination with the Sabatier reaction. No studies have been conducted to determine the most beneficial properties of a zeolite that make it a suitable adsorber of the produced water and consequently aid converting the highest amount of CO_2.

2.3. Thesis framework

2.3.1. Objective

Using the contributing factors mentioned in chapter 2.2, this study will focus on determining the most beneficial qualities of a zeolite that make it suitable for use in the Sabatier reaction and consequently convert the highest amount of CO_2. The main objective is to point out the most suitable zeolites for this application from the list of synthetic zeolites [3] and establish what properties make these zeolites the best option for adsorption of water in the Sabatier reaction.
It is important to note that desorption of zeolites is crucial to enable regeneration. In the remainder of this report, desorption is included when considering the suitability of zeolite types. Additionally, co-adsorption of CO_2 is also determined in the simulation, since this can cause the equilibrium to shift to the reactant side in case the co-adsorption is too high. A suitable zeolite will have a balance between water and CO_2 adsorption that will cause the equilibrium to shift to the product side.

2.3.2. Research questions

The main question to be answered in this study is:

- Which types of synthetic zeolites exhibit the highest suitability for water adsorption in the Sabatier reaction, and what specific properties account for their superior performance?

This question can be answered by answering the following subquestions:

1. Which synthetic zeolite types have the highest adsorption capacity for water in combination with suitable desorption and low co-adsorption capabilities in the Sabatier reaction?
2. What properties do these zeolite types have that differ from the less suitable types?
3. Which of these properties account for their superior performance in adsorbing water in the Sabatier reaction?
4. At what temperature and pressure is the adsorption of water in the zeolite further enhanced?

As explained in chapter 1.2.3, Monte Carlo simulations will be used to answer these questions. In this type of simulation, many different zeolites can be examined. Additionally, the simulation is time-independent, so the time a system needs to get to the equilibrium state is irrelevant. Therefore, many zeolites can be tested within a much shorter time range in contrast to experimental methods. Furthermore, Monte Carlo simulations have been proven to be both mathematically and thermodynamically accurate, since only the most likely microscopic states of the system are considered (see chapter 1.2.3). More information on the research methodology can be found in chapter 3.

2.3.3. Scope

This study focuses on determining the most suitable zeolites for the adsorption of water in the Sabatier reaction. Additionally, the properties that account for this suitability are identified. The most optimal temperature and pressure will also be established. As mentioned in chapter 2.3.1, desorption also plays a role in determining the suitability of a zeolite for use in the Sabatier reaction. Desorption will therefore also be examined for multiple zeolites. Also, co-adsorption of the other components besides water will be determined.
Multiple types of catalysts can be used for the Sabatier reaction. However, their suitability will not be discussed in this study. Furthermore, only existing synthetic zeolite types are examined in the simulation. Hypothetical zeolites are not considered. Based on the results of this study, hypothetical zeolites with the correct properties for water adsorption could be created in successive studies.

3
Research Methodology

This chapter focuses on the research methodology. First, the approach to answer the questions from chapter 2.3.2. is discussed. Second, the simulations necessary to answer these questions are explained. Furthermore, component properties and important aspects to be considered during the simulation are explained. Additionally, the RASPA software used to conduct the simulations is discussed.

3.1. Approach

The main objective of this study is to determine the most suitable zeolites for water adsorption in the Sabatier reaction. To achieve this, multiple simulations are necessary in which the adsorption and desorption of each component in the Sabatier reaction in a zeolite are assessed. Multiple zeolites will be used under various pressures and temperatures to get adsorption isotherms for each zeolite. This approach is conducted using the following steps:

1. Retrieve necessary property values of water, methane, carbon dioxide and hydrogen from the literature for the RASPA simulation (for RASPA: see chapter 3.8).
2. Determine the correct fugacity coefficient and gas composition for each component at the correct temperature and pressure.
3. Determine inaccessible pores in the zeolite using Zeo++.
4. Set up the RASPA simulation code including the necessary files and component properties.
5. Fill in properties and information of the system in the RASPA simulation code, including the correct file for the zeolite to be simulated and the inaccessible pores.
6. Run the simulation for all zeolite types in Table 1.1 at various pressures, temperatures and Si/Al ratios and generate the adsorption isotherms and the adsorption energy.
7. Determine which zeolites have optimal combinations of adsorption isotherms and adsorption energy for use in the Sabatier reaction.
8. Determine for which properties these zeolites significantly differ from the types with less optimal results and establish which of these properties are the reason for increased performance.

This approach results in an overview of the adsorption isotherms and adsorption energy of all selected zeolite types and a conclusion on the most optimal zeolite type for water adsorption in the Sabatier reaction. By comparing the properties of the zeolites and noting where they differ significantly, conclusions can be drawn on which properties are important for the suitability of a zeolite for water adsorption.

3.2. Properties of water, methane, carbon dioxide and hydrogen

The properties for water, methane, carbon dioxide and hydrogen are given in Table 3.1[54][16][1][5][39][48][14][53][15][8][17][11]. These properties are necessary for the Peng-Robinson Equation of State that will be used later in this research and for defining the components in RASPA.

Table 3.1: Necessary properties of water [54][16][1][5], methane [39][48][14][53], carbon dioxide [15][8] [39] and hydrogen [17][11] for the PR EoS. The properties include critical temperature and pressure, acentric factor, molar mass, atoms and diameter.

Property	**Water (H_2O)**	**Methane (CH_4)**	**Carbon dioxide (CO_2)**	**Hydrogen (H_2)**
T_c [K]	647.096	190.564	304.128	33
P_c [Pa]	$22.064 \cdot 10^6$	$4.599 \cdot 10^6$	$7.377 \cdot 10^6$	$1.3 \cdot 10^6$
Acentric factor [-]	0.344	0.011	0.224	-0.219
Kinetic diameter [pm]	265	380	330	289
Molar mass [g/mol]	18.015	16.042	44.009	2.016
Atoms	H O	H C	C O	H
Diameter [Ä]	3.0	3.8	3.3	2.89

3.3. Zeolite types and simulation conditions

In the simulation, four conditions can be altered, namely:

- Pressure
- Temperature
- Si/Al ratio
- Zeolite type

As mentioned in chapter 1.2.2, there are roughly 150 artificial zeolites. For this research, a selection is made of the zeolite types that will be examined for water adsorption. This selection can be seen in Table 1.1 in chapter 1.2.2 and is based on several considerations. First, zeolites that have similar properties as the FAU type are selected. As can be read in the literature review on previous research (Chapter 2.1), the FAU type is known to be suitable for adsorption in the Sabatier reaction. The types that have similar properties will therefore be considered in this research to see if they have similar or better performance compared to FAU. Additionally, certain types are selected based on their restricting pore diameter. Since all four components need to be able to enter the pores and move through the zeolite, only zeolite types with pores larger than 5 Å are considered. These types are divided into those with internal or external pores, or both. Internal pores are pores that run through the zeolite. External pores run along the surface of the zeolite. Figure 3.1 shows this difference for the AFR and IRR zeolite. The figures are generated with iRASPA (see chapter 3.9).

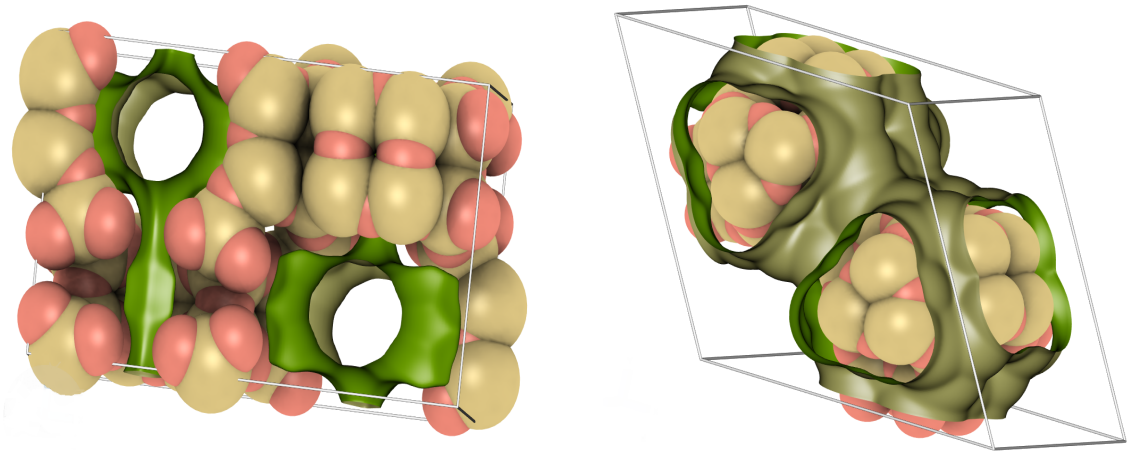

(a) AFR **(b)** IRR

Figure 3.1: (a) AFR with internal pores (> 5 Å) and (b) IRR with external pores (> 5 Å). Internal pores pass through the zeolite and external pores run across the surface of the zeolite. The simulation will indicate if this has an influence on the suitability for use in the Sabatier reaction.

The simulation will be conducted at different pressures and temperatures for each zeolite. As mentioned in chapter 1.2.1, the Sabatier reaction typically takes place at temperatures between 573 -673 K and pressures between 20-30 bar [52]. However, at lower temperatures, adsorption can be further enhanced. These temperatures can be applied when the zeolite is loaded with catalytically active metal [57]. Even though this loading cannot be simulated, the lower temperatures (453 - 633 K) will be used in the simulations, with pressures varying from 10 to 50 bar. These conditions are shown in Table 3.2.

Table 3.2: Conditions for the simulations. At two different temperatures, the adsorption isotherm is generated at pressures varying from 10 to 50 bar.

Temperature [K]	**Value [bar]**				
455	10	20	30	40	50
635	10	20	30	40	50

3.4. Fugacity coefficient & Gas composition

As mentioned in chapter 1.2.3, the chemical potential is calculated with the fugacity, which is determined by the fugacity coefficient and the pressure. As can be seen in chapter 3.3, various pressures and temperatures are used for the simulations. It is important that the correct fugacity coefficient for each component is used, corresponding to the pressure and temperature of that particular simulation. The program RefProp is used for determining the correct fugacity coefficients for the components [35]. RefProp applies the Helmholtz Free Energy Equation of State to determine the fugacity coefficient in mixtures, which is thermodynamically rigorous and accounts for residual parts and mixing rules [47]. In order to have RefProp determine the correct fugacity for each component, the gas composition of the mixture has to be known. This is determined using the equilibrium constant K. This procedure is explained further in chapter 4.2. In this process, the composition of the bulk gas is determined. This is directly applicable to the composition in the zeolite, since bulk gas and zeolite reach an adsorption equilibrium. This means that the chemical potential in both bulk gas and zeolite are equal to each other. Since the components are in equilibrium in the bulk gas, the components automatically also have to be in equilibrium in the zeolite to have adsorption equilibrium. Figure 1.2 in chapter 1.2.3 shows this graphically. In Appendix A, Tables A.1 to A.4 show the fugacity coefficient and gas composition for the components for each temperature-pressure combination, respectively.

3.5. Si/Al ratio and charge

As explained in chapter 1.2.2, zeolites mainly consist of silicon or aluminum in combination with oxygen. The Si and Al atoms are interchangeable and effect the suitability for the zeolite regarding water adsorption. A higher Si/Al ratio makes the zeolite more hydrophobic, while a low Si/Al ratio makes it more hydrophilic [37].
In RASPA, the Si/Al ratio can be adjusted. It is important that charge compensation is also applied when interchanging Si and Al atoms. Every SiO_2 tetrahedral site is neutrally charged. Since Al has a different charge, every AlO_4 site has a negative charge. It is therefore important to add charge-balancing cations. For this research, Na^+ cations are used [58]. These cations need to be placed in realistic sites in the zeolite to balance the negatively charged AlO_4 sites. Additionally, oxygen atoms linking Al and Si atoms have a slightly different charge than oxygen atoms linking Si with other Si. Table 3.3 shows the applied charges for each molecule [2].

Table 3.3: Applied charge for each molecule present in the zeolite [2].

Molecule	**Charge [e]**
Si	0.78598
Al	0.48598
O (Si-Si)	-0.39299
O (Al-Si)	-0.41384
Na^+	0.3834

Furthermore, Al atoms cannot be placed next to each other, since this will weaken the structure. This is called the Löwenstein rule [22]. This also determines the maximum number of Si atoms that can be replaced by Al. A Python script using the software Porran is written in which Si atoms are replaced by Al obeying the Löwenstein rule and that adjusts the adjacent O atoms to the correct charge. The script is shown in Appendix D. For each zeolite, the simulations will be conducted using the structure with no Al atoms and additionally for the structure with an Si/Al ratio between 15-27. Table 3.4 shows the Si/Al ratio for each zeolite. An Si/Al ratio of 20 is a realistic number for each of the zeolites and by taking the same ratio for all types, the results can be compared. However, the ratio cannot be the exactly 20 for each zeolite, because the number of Si atoms is different for each type and the interchanged number of atoms needs to be a whole number. Therefore, the Si/Al ratio is chosen to be as close to 20 as possible for each zeolite type.

Table 3.4: Si/Al ratio for each zeolite.

Zeolite	**Si/Al ratio**
FAU	20.3
BOZ	22
JSR	23
SBT	19.6
AFR	15
BEA	20.3
AFY	15
BPH	27
IRR	25
ITT	22
EMT	18.2
SAO	17.7
SBE	20.3
SBS	18.2

3.6. Inaccessible pores

Certain zeolite types have inaccessible pores. This means that the pore size is large enough for the components to move through, but the entrance to the pore is not on the surface of the zeolite and therefore not accessible to the molecules. Additionally, there are spaces in the zeolite that would be large enough for the components, but the channels leading to the spaces are too small or they are not connected to channels, which makes these spaces inaccessible as well.
To gain realistic results for the adsorption isotherms, it is important to determine these inaccessible pores and have RASPA block these pores for the simulation, so molecules are not inserted in these pores. With the software Zeo++, the inaccessible pores in a zeolite are determined and blocked [33]. This information is used in RASPA to make sure the simulation does not place molecules in inaccessible regions. Using iRASPA, the position of the blocked pores can be made visual by adding molecules at these positions to the zeolite CIF file. This is done using Argon molecules, because their size and color in iRASPA make them distinguishable in the framework, as can be seen in Figure 3.3. The figure shows excellent agreement between the position of the blocking pores in iRASPA and the ones determined with Zeo++.

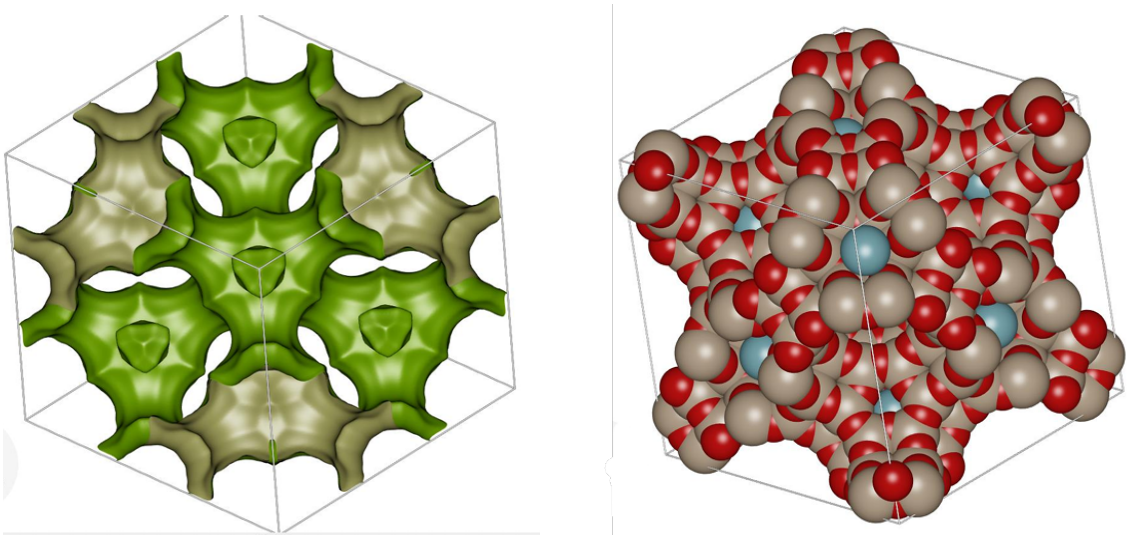

(a) Channels in FAU

(b) Blocked pores using Argon in FAU

Figure 3.2: Figure a shows channels in zeolite FAU, made visual with iRASPA. 4 of the 8 inaccesible pores are visible. Figure b shows the inaccesible pore locations in FAU according to Zeo++, denoted with an Argon molecule (blue), made visual with iRASPA. The Argon molecules correspond to the location of the inaccessible pores in Figure a.

3.7. Desorption

The water and methane that are adsorbed by the zeolite, need to be retrieved through desorption. If not, the water and methane cannot be used for useful purposes and the zeolite will become saturated, in which case it will no longer adsorb water. To determine if desorption is possible, the adsorption energy is reviewed. The adsorption energy is the extent to which molecules are attached to the zeolite. A large negative adsorption energy means the molecules attach to the zeolite easily and are hard to desorb. The value for the enthalpy of adsorption for which desorption is relatively simple typically ranges from -8 to -40 kJ/mol [45]. Between -40 and -80 kJ/mol, desorption becomes harder and above -80 kJ/mol, desorption becomes nearly impossible. It is therefore desirable that the most suitable zeolite has an adsorption energy between -8 to -40 kJ/mol.

3.8. RASPA

RASPA is a software package designed to simulate adsorption and diffusion of molecules in flexible nanoporous materials, such as zeolites [21][49]. The software uses Monte Carlo simulations as explained in chapter 1.2.3. This study uses RASPA with the interface Visual Studio Code. In this chapter, an overview on RASPA is given. Additionally, the necessary input and output files for the adsorption simulation in RASPA are explained.

3.8.1. Overview

RASPA is written in C++23 and uses configurational-bias Monte Carlo (CBMC) and continuous fractional component Monte Carlo (CFCMC) simulations. For electrostatics it uses the Ewald summation and Molecular Dynamics (MD) calculations are based on symplectic and measure-preserving integrators [21]. Transition-matrix MC is used to compute free energies and density of states [49]. These choices provide the best accuracy and correctness out of the options available in the literature. Several experimental studies show a high level of agreement with results from RASPA simulations.
For particles, RASPA uses three different types, namely framework atoms, adsorbates and cations. This has the advantage that the different components of the total energy can be used and its interactions examined.
RASPA puts no restriction on the number of components or molecules used in a simulation. The C-convention is used to number components, frameworks etc., which means they start at zero. Additionally, RASPA uses the Peng-Robinson Equation of State (PR EOS) to convert pressure to fugacity

if no fugacity coefficient is given in the input [7][21].
The following units are standard units in RASPA:

- Unit of length l_0 is Ångstrom ($l_0 = 10^{-10}$ m)
- Unit of time t_0 is picosecond ($t_0 = 10^{-12}$ s)
- Unit of charge q_0 is the proton charge ($m_0 = 1.602 \cdot 10^{-19}$ C)

All other units follow from these standard units [21].

3.8.2. Force field
The force field of a simulation is crucial in determining the energy of each cycle. The energy calculation is given in chapter 1.2.3. In the RASPA file for the force field, the self interactions between molecules can be specified by defining the correct type, such as Lennard-Jones. The values for the Lennard-Jones parameters can also be assigned in this file for each component. Additionally, the pseudo atoms, their mass and electrostatic charge can be defined.

3.8.3. Components
In another file, the components can be defined by assigning their critical temperature, critical pressure, acentric factor and bonding type. Also, the position of the atoms relative to each other and their bonds are defined. The force field of each component is included in this file by calling this component from the force field file.

3.8.4. Zeolite
For simulations including a zeolite, the zeolite type must also be defined. This can be done using iRASPA (see chapter 3.3). From this software program, a cif-file with information on a certain zeolite can be exported to RASPA. This file contains the cell lengths, angles and cell volume. It also documents all the atoms present in the zeolite and their position in a grid.

3.8.5. Simulation
The aforementioned files are important for the simulation file. In this file, the simulation type (in this case Monte Carlo), the number of cycles and initialization cycles are defined. The zeolite is specified by calling this file and defining the number of unit cells along the crystallographic axis, the external temperature and external pressure. The force field is included by directing RASPA to the correct file in the directory. The components are included by calling these files and specifying the fugacity coefficient, the translation-, reinsertion- and swap probability and the number of these molecules that the simulation has to create. In case of adsorption, this number is set to zero, which means there are initially no molecules present in the zeolite. The simulation inserts or removes zeolites using swap moves.

3.8.6. Output
After conducting the simulation, RASPA gives an output file. In this file, RASPA gives the used units and constants. It also gives an overview of the input files, such as the pressure and temperature imposed on the system, the components and their properties and the zeolite.
The RASPA file also shows the results of the simulation. It gives the interim results after a certain number of cycles, which is specified in the simulation file. At the end of the simulation, an overview is given of the end results per component. This includes energy statistics, MC-moves statistics and the absolute and excess loading.

Figure 3.3 gives a schematic overview of the input and output files and the information in those files. The input block represents the information that needs to be inserted in the files and the output block represents the information that is displayed in the output file.

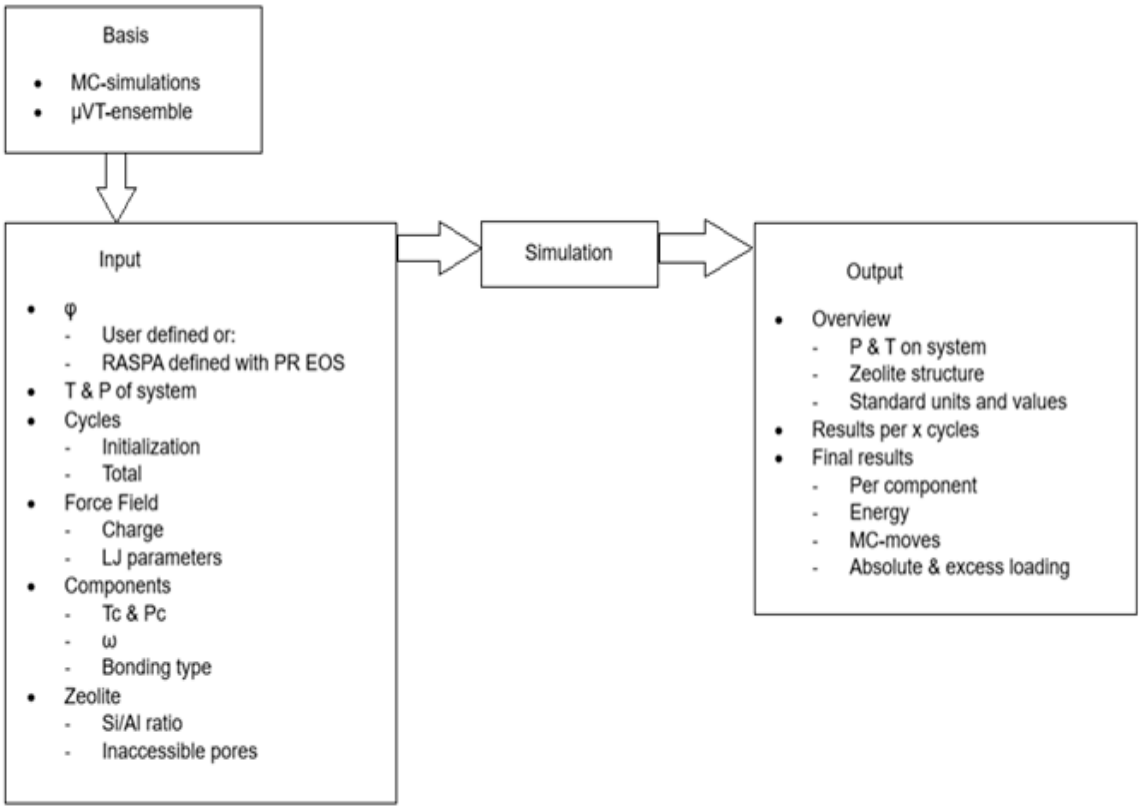

Figure 3.3: Block scheme with input and output information for the Monte Carlo simulation in RASPA.

3.9. iRASPA

iRASPA is the visualization software package for RASPA, that gives many options for visualizing and editing materials. Specific to this study, iRASPA is used to visualize zeolites and transfer the associated cif-files to RASPA for the simulation. Additionally, iRASPA can show where the adsorbed molecules are located in the zeolite framework. Figure 3.4 shows the visualization of zeolite type FAU in iRASPA. It can be seen that the zeolite structure, atom positions and pores are easily examined using this visualization. The visualization can be adjusted, for example by only showing the atoms or the channels, and in different lay-outs.

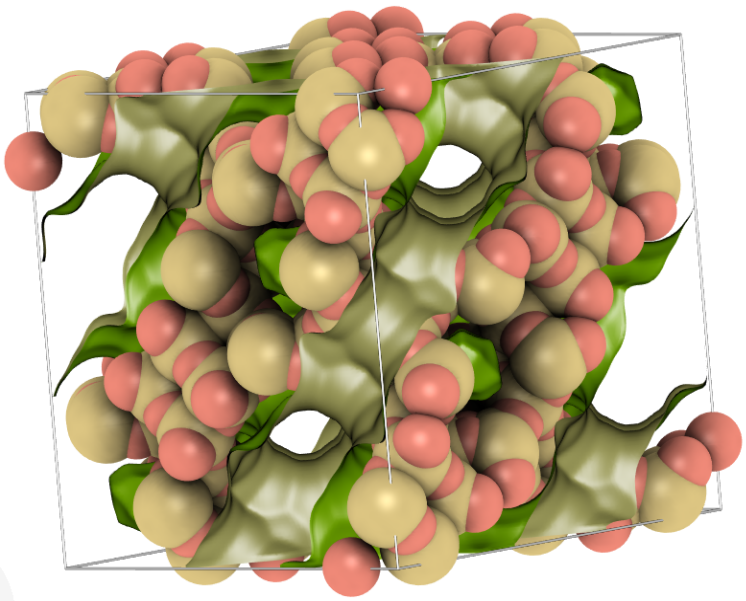

Figure 3.4: Example of a zeolite visualization in iRASPA. The zeolite in the picture corresponds to FAU. These visualizations clearly indicate the position of the atoms, pores, pore sizes and channels.

4
Simulation Preparation

This chapter shows the preparation for the simulations. First, the comparison between the fugacity coefficient from RefProp and Peng-Robinson is discussed. After this, the results of the calculation for the gas composition are shown. Also, the number of initialization cycles is determined and a comparison is made to a previous adsorption simulation to check resemblence.

4.1. Fugacity Coefficient

4.1.1. RefProp and Peng-Robinson comparison

For the fugacity coefficient of the components at every selected temperature and pressure, the program RefProp can be used. However, the validity of RefProp needs to be determined by comparing the values for the fugacity coefficient to the ones calculated in the Peng-Robinson Equation of State (PR EoS) for mixtures [6]:

$$\ln \phi_i = \frac{b_i}{b_{\text{mix}}}(Z-1) - \ln(Z-B) - \frac{A}{2\sqrt{2}B}\left(\frac{2\sum_j x_j a_{ij}}{a_{\text{mix}}} - \frac{b_i}{b_{\text{mix}}}\right)\ln\left(\frac{Z+(1+\sqrt{2})B}{Z+(1-\sqrt{2})B}\right) \tag{4.1}$$

The full PR EoS including mixing rules can be found in Appendix B. In a Matlab script, the fugacity coefficient of each component in the Sabatier reaction at every temperature and pressure in the simulation is calculated and plotted against the value from RefProp. The results for T = 455 K can be seen in Tables 4.1 and 4.2.

Note that the calculation is done for a mixture excluding water, which is CO_2, H_2 and CH_4, and including water, which is CO_2, H_2 and CH_4 and H_2O. The reason for this is that water is polar, whereas the other three components are non-polar. The Peng-Robinson EoS is less suitable for polar components. Therefore, the comparison to RefProp is made both for a mixture with and without water to see if this has a large impact on the difference between the two values for the fugacity coefficient. For the mixture without water, the mole fraction of each component is $y = 0.33$ and with water $y = 0.25$.

Table 4.1: Difference between fugacity coefficients calculated in RefProp and from the Peng-Robinson Equation of state at T = 455 K for a mixture without water.

Pressure [bar]	**Component**		
	CH_4	CO_2	H_2
10			
PR	0.9965	0.9897	1.0057
RefProp	0.9991	0.9912	1.0084
Deviation [%]	0.3	0.2	0.3
20			
PR	0.9932	0.9797	1.0114
RefProp	0.9983	0.9826	1.0168
Deviation [%]	0.5	0.3	0.5
30			
PR	0.9900	0.9700	1.0171
RefProp	0.9977	0.9742	1.0252
Deviation [%]	0.8	0.4	0.8
40			
PR	0.9871	0.9607	1.0229
RefProp	0.9971	0.9661	1.0337
Deviation [%]	1	0.6	1.1
50			
PR	0.9843	0.9517	1.0286
RefProp	0.9967	0.9582	1.0422
Deviation [%]	1.3	0.7	1.3

Table 4.2: Difference between fugacity coefficients calculated in RefProp and from the Peng-Robinson Equation of state at T = 455 K for a mixture with water.

Pressure [bar]	**Component**			
	CH_4	CO_2	H_2	H_2O
10				
PR	0.9971	0.9877	1.0109	0.9620
RefProp	0.9991	0.9907	1.0146	0.9780
Deviation [%]	0.2	0.3	0.4	1.7
20				
PR	0.9944	0.9758	1.0221	0.9252
RefProp	0.9987	0.9809	1.0300	0.9554
Deviation [%]	0.4	0.5	0.8	3.3
30				
PR	0.9920	0.9641	1.0337	0.8897
RefProp	0.9984	0.9713	1.0457	0.9333
Deviation [%]	0.6	0.7	1.2	4.9
40				
PR	0.9899	0.9528	1.0456	0.8554
RefProp	0.9982	0.9618	1.0617	0.9116
Deviation [%]	0.8	0.9	1.5	6.6
50				
PR	0.9881	0.9417	1.0578	0.8224
RefProp	0.9982	0.9526	1.0780	0.8905
Deviation [%]	1	1.2	1.9	8.3

The tables show a value difference below 2% for the pressure range 10 - 50 bar, except for water. Water has the largest value difference between the PR EoS and RefProp, which increases with increasing

pressure.
From the tables, it can be concluded that the difference between the values from the PR EoS and RefProp is small for both mixtures and RefProp can therefore be used to determine the fugacity coefficients for the simulations. Water is the component that has the highest difference between both values, but since RefProp takes into account the polarity of water and PR EoS does not, it is valid and more suitable to use RefProp for the fugacity coefficients of water as well.

4.1.2. Force field and RefProp comparison

As explained in chapter 3.4, the chemical equilibrium between the bulk gas and the zeolite is driven by fugacity. This process relies on the assumption that the fugacity determined from the force field in RASPA is equal to the one determined in RefProp under the same conditions. This can be verified with a simulation without the zeolite, so the components mimic the bulk gas. In Table 4.3 the comparison between both methods can be seen. The selected temperature is T = 455 K and the number of molecules is equal to 100 per component. The components are simulated as pure components.

Table 4.3: Comparison between the fugacities from RefProp and using force fields in RASPA for each component.

f_i **[bar]**	**Component**			
	CH_4	H_2O	CO_2	H_2
RefProp	1.5331	1.5201	1.5283	1.5356
Force Field	1.5336	1.535	1.5303	1.5355
Deviation [%]	0.03	0.97	0.13	0.65

As can be seen in the table, the deviations between the fugacities for each component are negligibly small, proving that the chosen force field in RASPA calculates the correct fugacities for each component.

4.2. Gas composition

4.2.1. Calculation

To determine the gas composition of the gas mixture, the equilibrium constant is calculated.

The equilibrium constant K can be determined by either using the Gibbs free energy or the fugacities of each component. Equation 4.1 en 4.2 show the calculation for the equilibrium constant using the Gibbs free energy.

$$K = \exp(-\frac{\Delta \mathring{G}}{RT}) \tag{4.2}$$

With:

$$\Delta G = (\sum \nu \overline{h}_{f,\text{products}} - \sum \nu \overline{h}_{f,\text{reactants}}) + (\sum \nu \Delta \overline{h}_{\text{products}} - \sum \nu \Delta \overline{h}_{\text{reactants}}) - T \cdot (\sum \nu \overline{s}_{\text{products}} - \sum \nu \overline{s}_{\text{reactants}}) \tag{4.3}$$

Appendix C, Table C.1 and C.2 show the values for the enthalpy and entropy for each component at the applied temperature and pressure [44] [24].

Equation 4.3 shows the calculation using the fugacities of each component.

$$K = \left[\frac{(f_C)^{\nu_C}(f_D)^{\nu_D}}{(f_A)^{\nu_A}(f_B)^{\nu_B}}\right]\left[\frac{(\mathring{f}_A)^{\nu_A}(\mathring{f}_B)^{\nu_B}}{(\mathring{f}_C)^{\nu_C}(\mathring{f}_D)^{\nu_D}}\right] \tag{4.4}$$

This equation is suited for non-ideal mixtures including polar components, such as water. It therefore differs from equation 2.1, which is only applicable for ideal gasses. Since the Sabatier reaction is a non-ideal mixture including polar component, equation 4.3 is applied.

K is calculated using the Gibbs free energy at a certain temperature and RefProp is used to generate the fugacities at given temperature, pressure and reference pressure (P = 1.01325 bar). In RefProp,

the mixture and its composition need to be specified. This is the initial guess for the composition. Then, K is determined using the fugacities and the gascomposition is adjusted so K fits the value determined from the Gibbs free energy. These new values for the gascomposition are put into RefProp to generate the new fugacities for this new composition. Then, K is calculated again and the gascomposition is adjusted so K fits the value from the Gibbs free energy. This iterative process is repeated until the values for the gascomposition in RefProp and the calculation are equal and fit the value for K determined from the Gibbs free energy.

The composition is determined for each temperature and pressure in the simulation, according to Table 3.2. The results for the fugacity and the gascomposition per component can be seen in Appendix A.

4.2.2. Comparison to Lewis-Randall

For components in an ideal gas mixture at moderate pressures, the Lewis-Randall rule can be applied to determine the fugacity of each component:

$$f_i = y_i f_i^{\text{pure}}(T, P) \tag{4.5}$$

This rule states that the fugacity of a component in an ideal gas mixture is directly related to its mole fraction in the mixture. In Equation 4.3, the fugacities are directly taken from RefProp, so the Lewis-Randall rule is not invoked. To verify this choice, the fugacities from RefProp at T=455 K and pressures between 10-50 bar are compared to the fugacities calculated with the Lewis-Randall rule. In Table 4.4, the percentage derivation between these two methods is shown.

Table 4.4: Percentage derivation between fugacity coefficients from RefProp and calculated using Lewis-Randall.

Pressure [bar]	**Component**			
	CH_4	H_2O	CO_2	H_2
10				
RefProp	1.025	0.947	1.001	1.095
Lewis-Randall	0.998	0.938	0.989	1.004
Deviation [%]	3	1	1	9
20				
RefProp	1.055	0.894	0.999	1.209
Lewis-Randall	0.997	0.492	0.978	1.009
Deviation [%]	6	82	2	20
30				
RefProp	1.089	0.841	1.000	1.347
Lewis-Randall	0.995	0.329	0.968	1.013
Deviation [%]	9	156	3	33
40				
RefProp	1.13	0.789	1.004	1.514
Lewis-Randall	0.994	0.248	0.957	1.017
Deviation [%]	14	218	5	49
50				
RefProp	1.179	0.737	1.012	1.722
Lewis-Randall	0.993	0.199	0.947	1.022
Deviation [%]	19	270	7	69

It can be seen clearly that at higher pressures, the deviations start to increase rapidly, especially for H_2O. The reason for this is that water is strongly polar, and thus behaves highly non-ideal. Additionally, the components from the Sabatier reaction form a non-ideal mixture and are simulated at high pressures. From Table 4.4, the conclusion can be drawn that for the components in the Sabatier reaction the Lewis-Randall rule does not give reliable results for the fugacities and is therefore not applied in the calculation.

4.3. Initialization cycles

After a certain number of cycles, the energy of the system starts to fluctuate around one value, which means the system has reached equilibrium. The cycles that are conducted before this equilibrium is reached, have energies that are too high or low compared to the equilibrium value. Therefore, these cycles give unrealistic values for the properties of the system and should therefore not be taken into account when calculating the value of these properties. In RASPA3, these cycles are denoted as initialization cycles. To determine how many initialization cycles are needed, an initial simulation is conducted from which the energy is plotted versus a large number of cycles to check when the system starts to fluctuate around the same value. This plot can be seen in Figure 4.1.

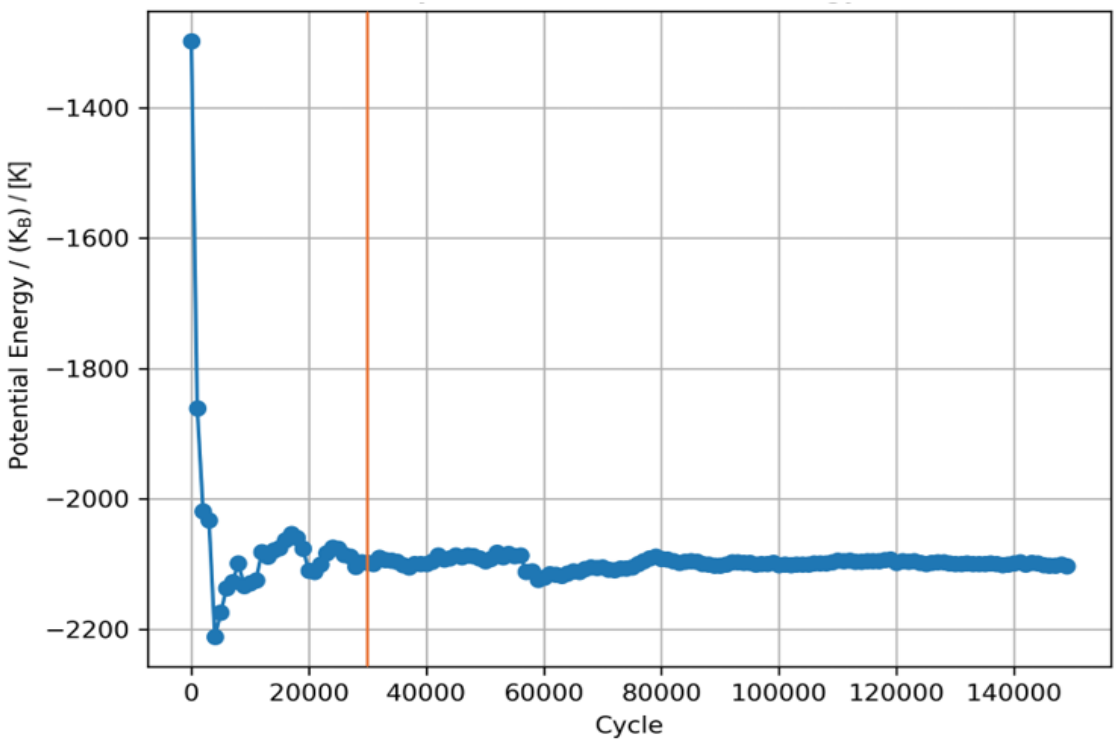

Figure 4.1: Potential energy versus number of cycles for T = 455 K & P = 10 bar in zeolite FAU.

The figure shows that the system starts to equilibrate after 30000 cycles, denoted by the vertical orange line. Taking into account a margin, 40000 initialization cycles will be used in the simulations.

4.4. Literature comparison

In order to check whether the simulation conditions are correct, it is important to compare the results to the literature [25], as can be seen in Figure 4.2. This figure shows the adsorption isotherms for CO_2 in FAU for a simulation (red) and experiment (blue) conducted by García-Sánchez et al [25]. The results for the RASPA3 simulation (green) are plotted for comparison.

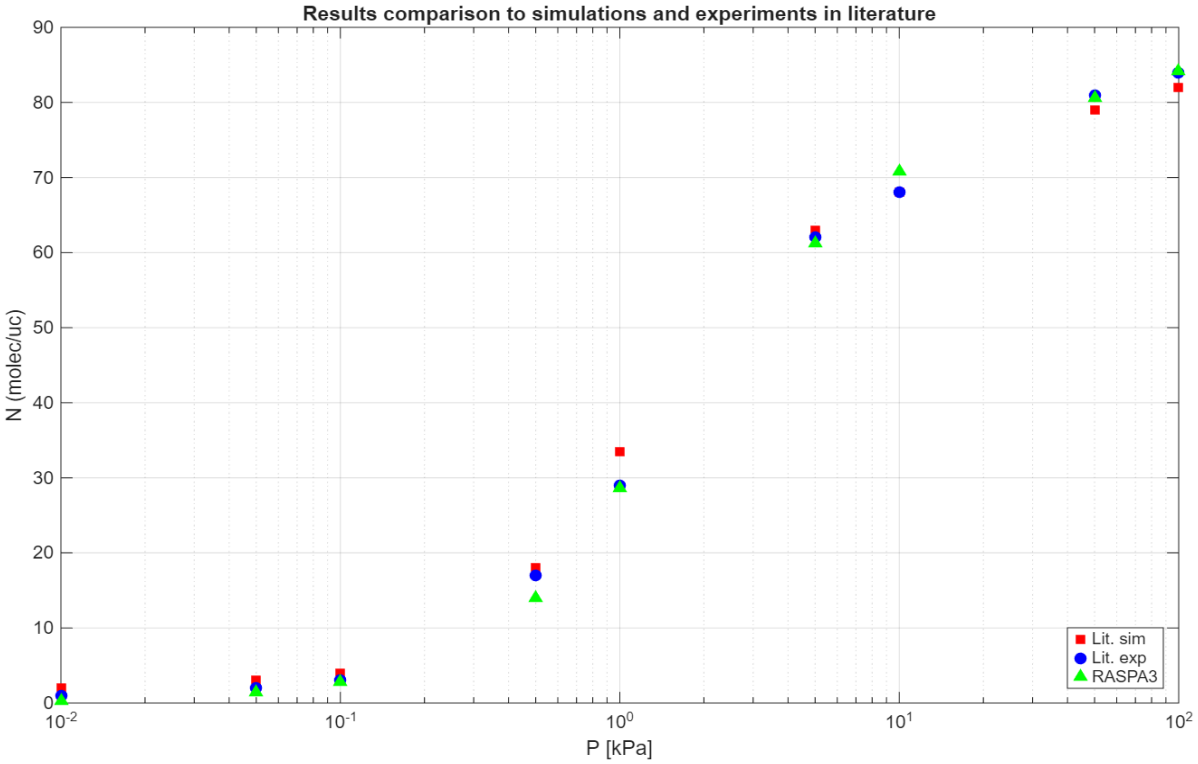

Figure 4.2: Results from the RASPA3 simulation (green) compared to simulations (red) and experiments (blue) from literature for CO_2 in FAU [25].

The figure shows agood agreement between the results from the literature and the RASPA3 simulations. The adsorption increases with increasing pressure in the same order of magnitude for the RASPA3 simulation as it does in the literature. The small deviation between the results is most likely due to the fact that not all simulation conditions used in the literature are reported, such as the swap- or reinsertion probabilities, so these cannot be copied into the RASPA3 simulation. However, the deviations are negligible, which leads to the conclusion that the simulation conditions are correct and lead to the expected results, based on literature.

5
Results

In this chapter the results from the simulations are displayed and discussed. Firstly, the adsorption isotherms of each component in all-silica zeolites at 455 K and 635 K are shown, respectively. Then, the adsorption isotherms of each component in zeolites including aluminum at 455 K are shown. Finally, the enthalpy of adsorption of each component in the zeolites is displayed as a measure for the desorption capabilities of the zeolites. The numerical results for each simulation can be found in Appendix E.

5.1. Adsorption isotherms in all-silica zeolites at 455 K

This section shows the adsorption isotherms of H_2O, CH_4, CO_2 and H_2 in several zeolite types at 455 K, respectively. The zeolites are all-silica and contain no aluminum.

5.1.1. Adsorption isotherm of H_2O

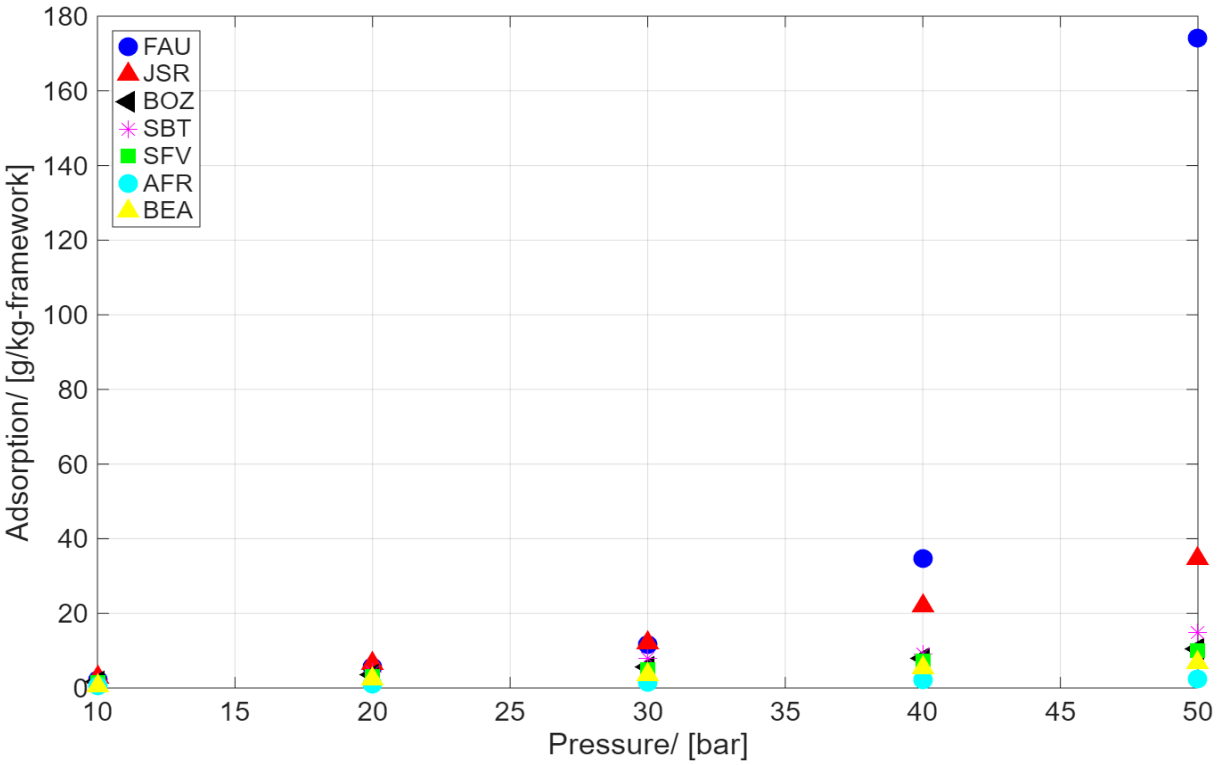

Figure 5.1: Adsorption of H_2O in zeolites that have similar properties as FAU and large internal pores in the pressure range 10 - 50 bar at T = 455 K.

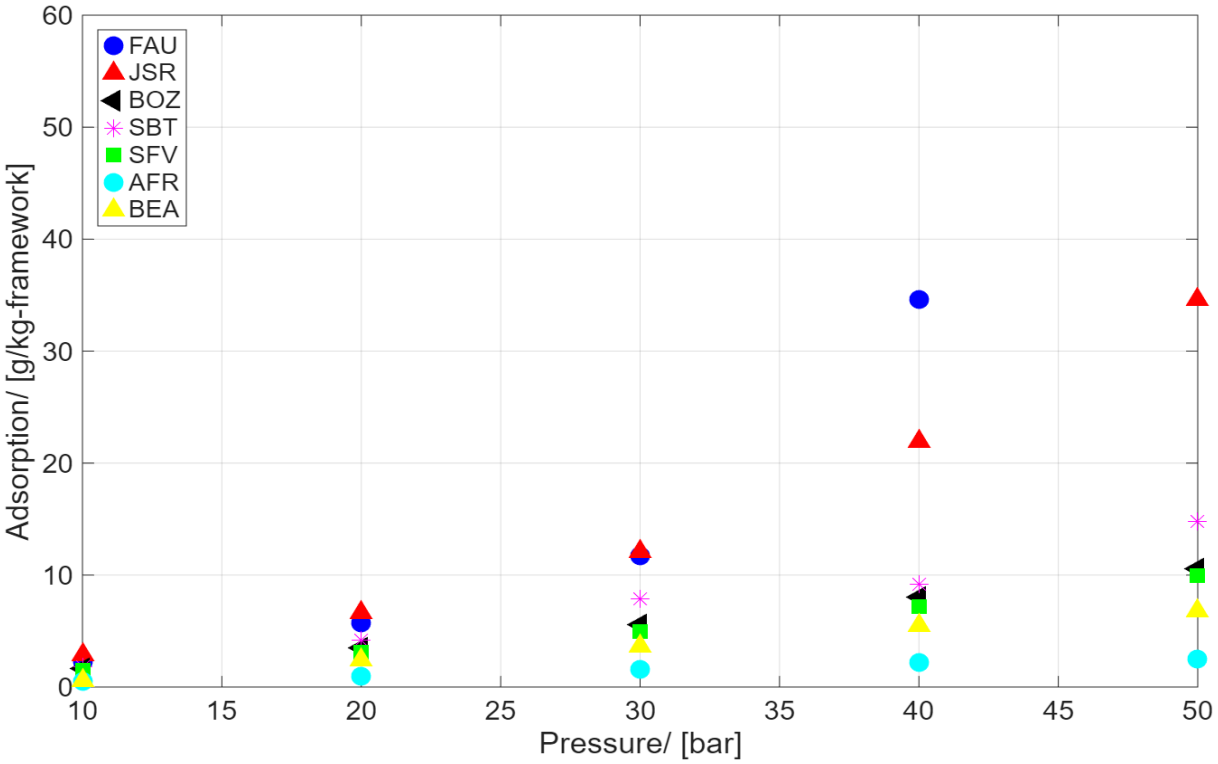

Figure 5.2: Adsorption of H_2O in zeolites that have large external pores and both large in- and external pores in the pressure range 10 - 50 bar at T = 455 K, zoomed in.

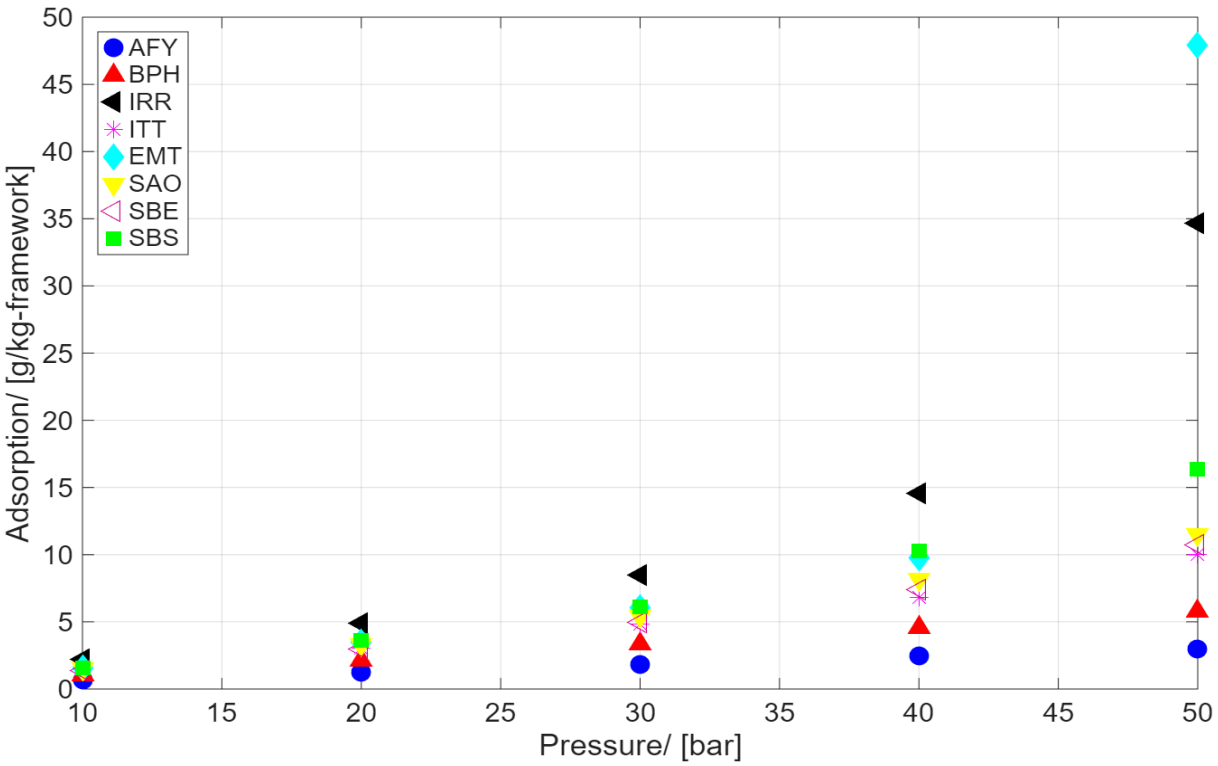

Figure 5.3: Adsorption of H_2O in zeolites that have large external pores and both large in- and external pores in the pressure range 10 - 50 bar at T = 455 K.

5.1.2. Adsorption isotherm of CH_4

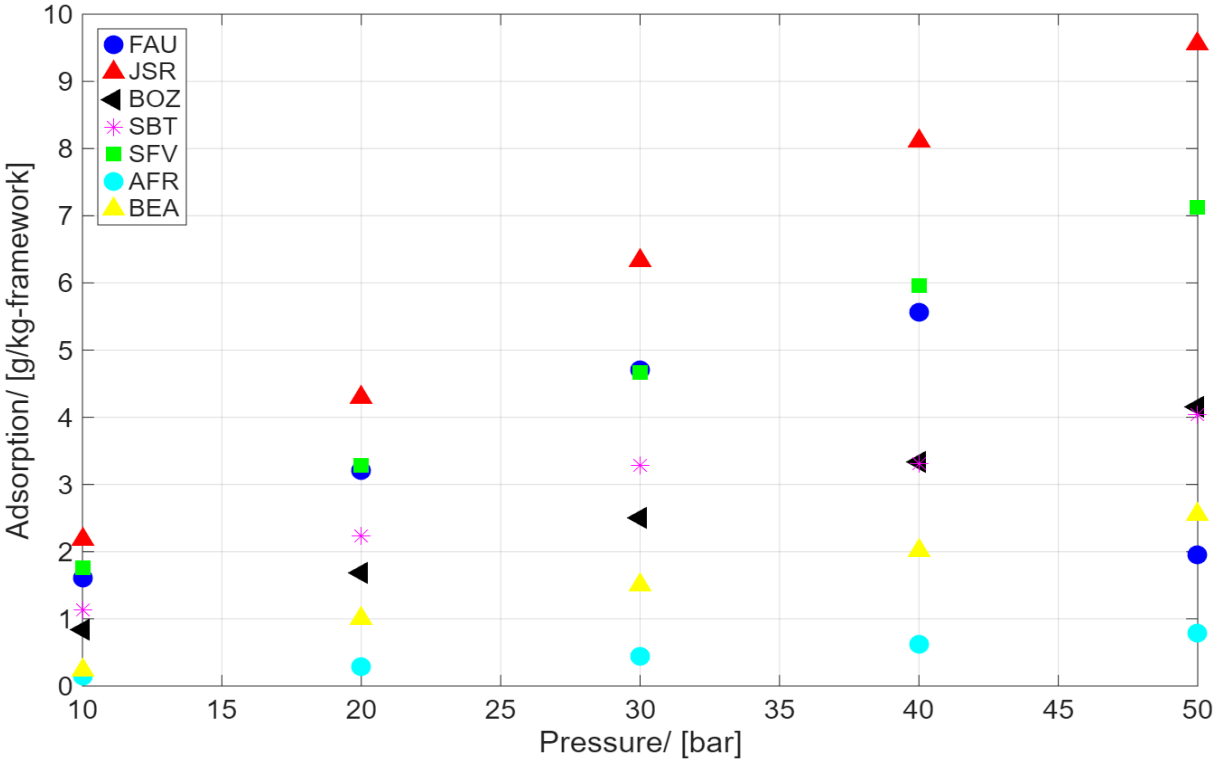

Figure 5.4: Adsorption of CH_4 in zeolites that have similar properties as FAU and large internal pores in the pressure range 10 - 50 bar at T = 455 K.

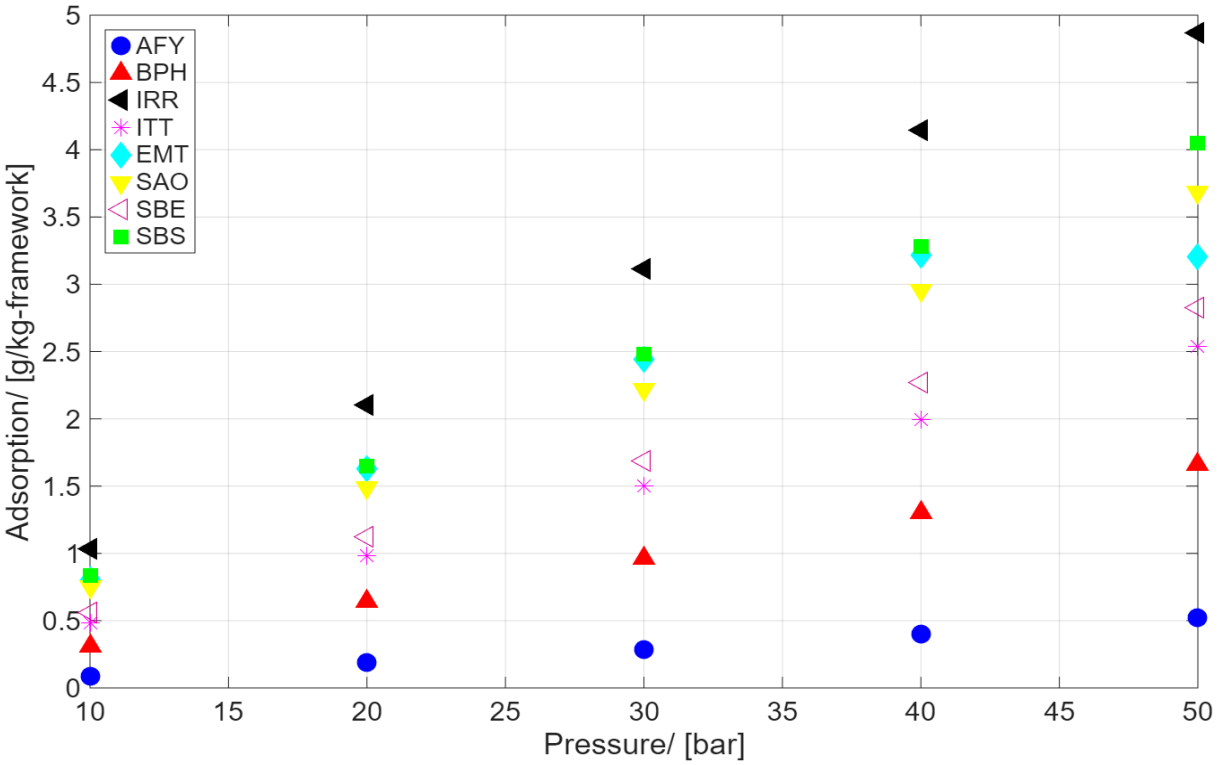

Figure 5.5: Adsorption of CH_4 in zeolites that have large external pores and both large in- and external pores in the pressure range 10 - 50 bar at T = 455 K.

5.1.3. Adsorption isotherms of CO_2

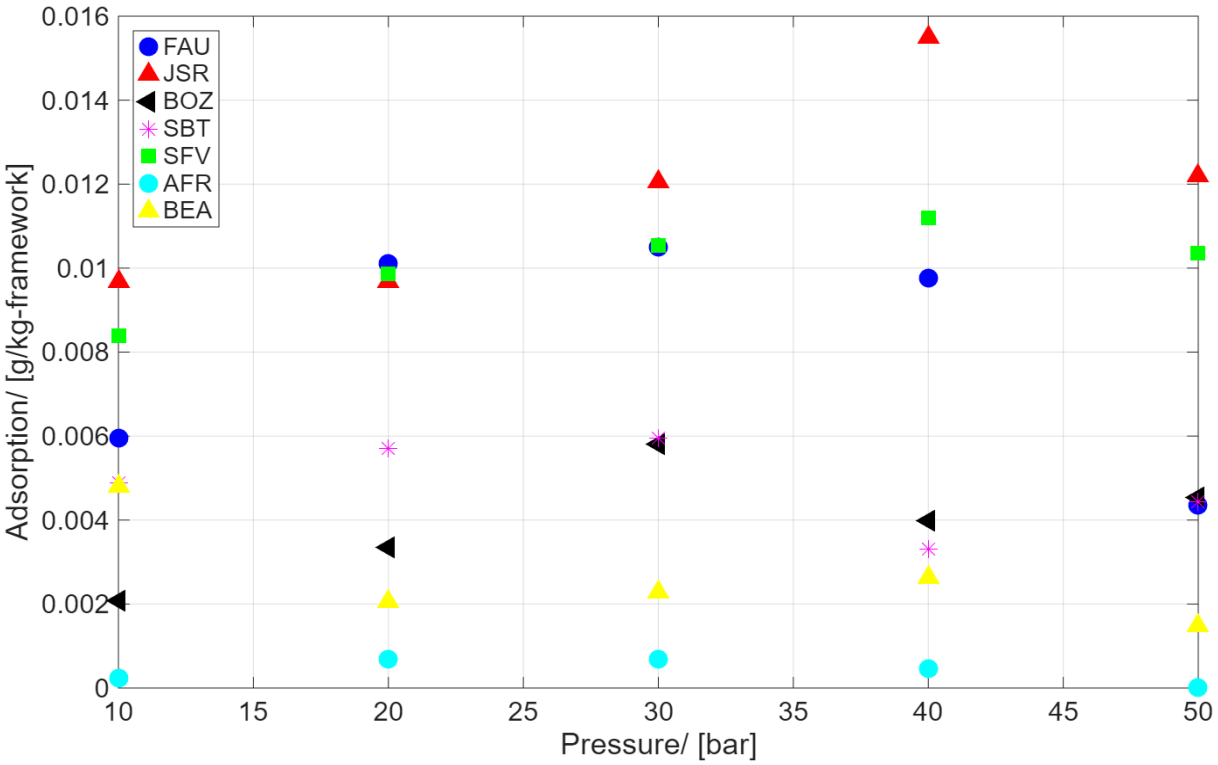

Figure 5.6: Adsorption of CO_2 in zeolites that have similar properties as FAU and large internal pores in the pressure range 10 - 50 bar at T = 455 K.

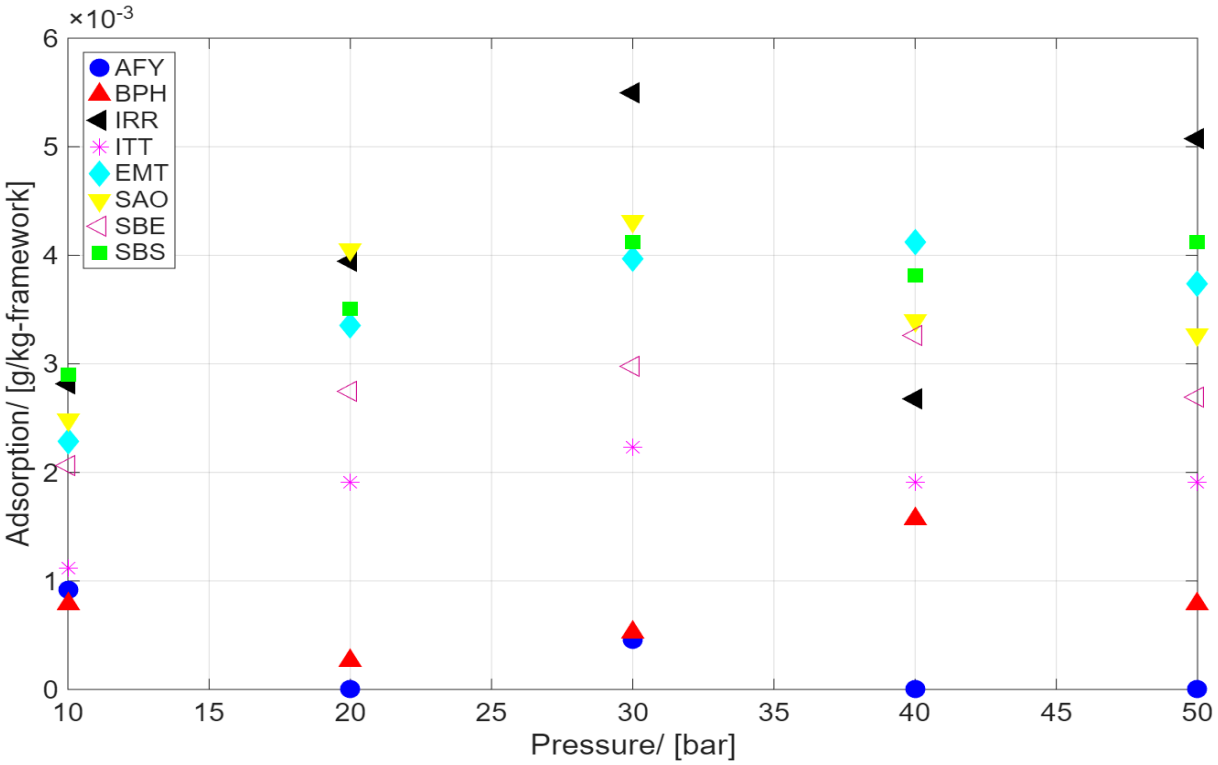

Figure 5.7: Adsorption of CO_2 in zeolites that have large external pores and both large in- and external pores in the pressure range 10 - 50 bar at T = 455 K.

5.1.4. Adsorption isotherms of H_2

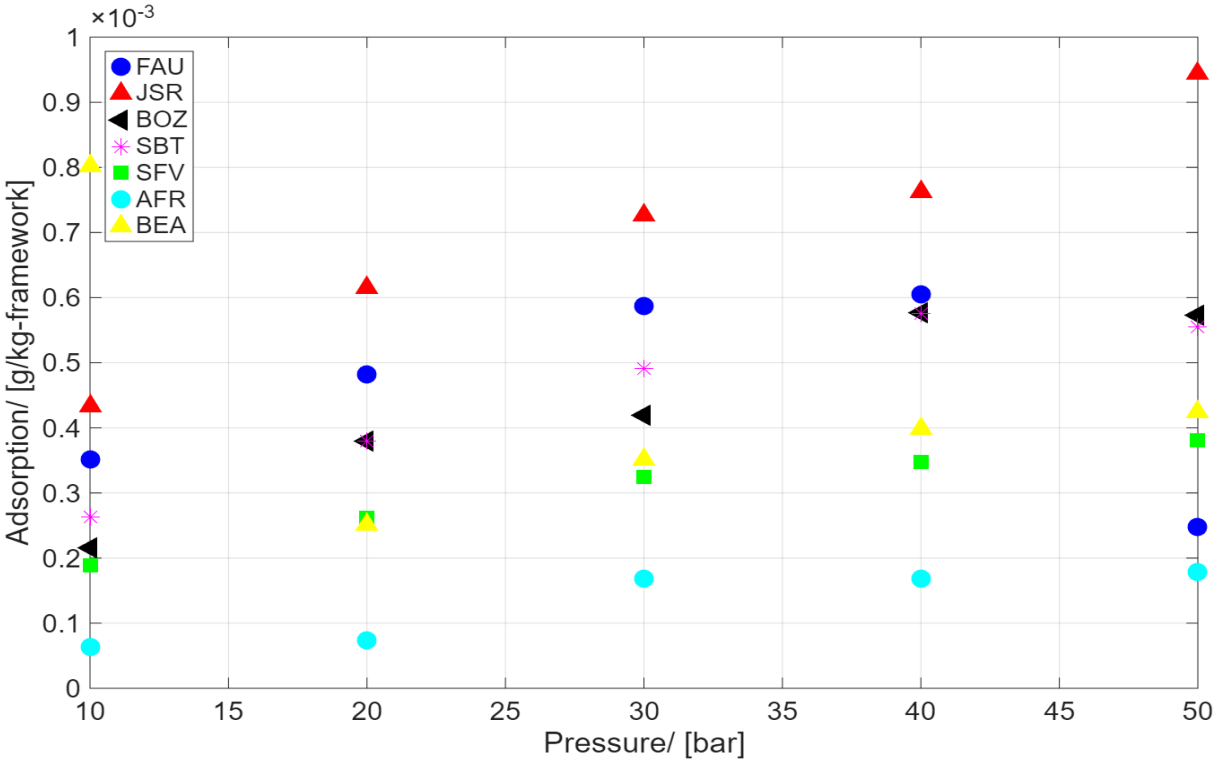

Figure 5.8: Adsorption of H_2 in zeolites that have similar properties as FAU and large internal pores in the pressure range 10 - 50 bar at T = 455 K.

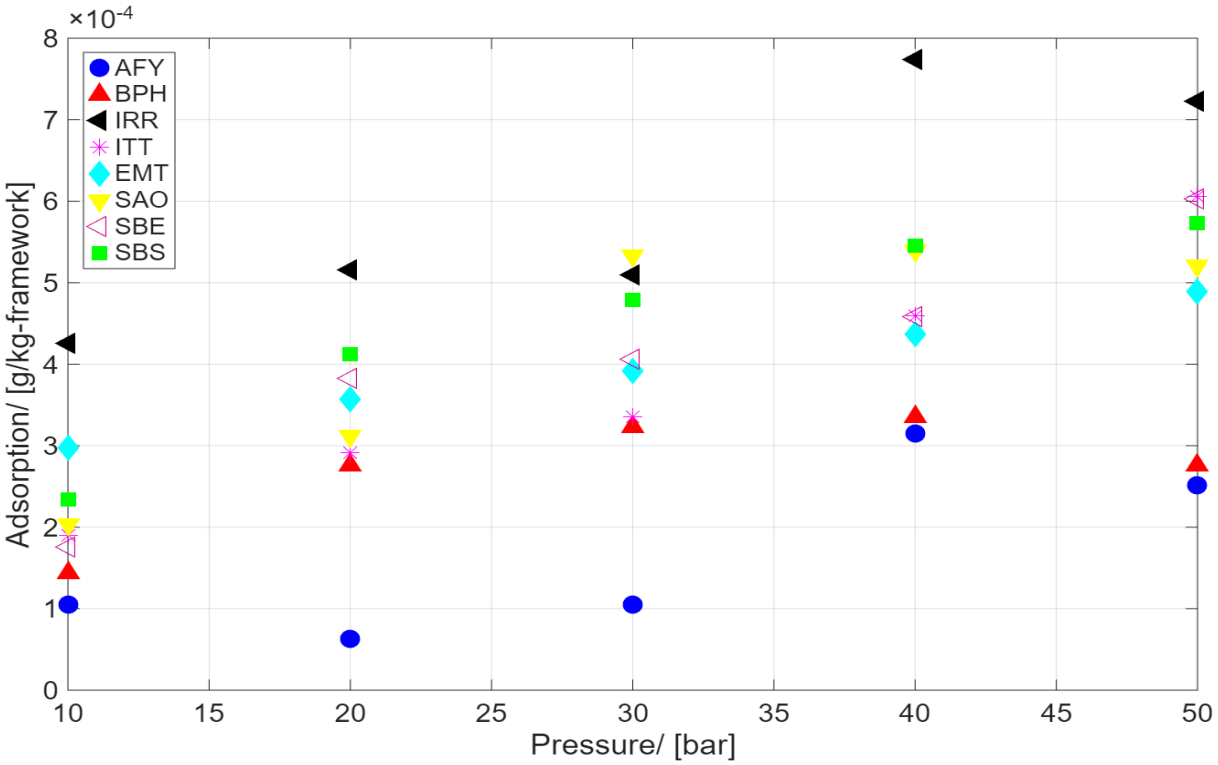

Figure 5.9: Adsorption of H_2 in zeolites that have large external pores and both large in- and external pores in the pressure range 10 - 50 bar at T = 455 K.

As can be seen in figures 5.1 to 5.3, the adsorption of water onto the zeolites increases as pressure increases. This is because at higher pressure, there are more molecules per unit volume and more collisions with the surface, in this case the zeolite. The figures 5.4 and 5.5 show that the adsorption of methane also increases slightly as pressure increases, except for certain zeolites that have a high water adsorption at high pressures, which are FAU and EMT. The reason for this is that the water in these zeolites dominates at high pressures and is able to form stable structures, which prevents other components from entering the zeolite. It is also noticeable that the adsorption isotherms for CO_2 and H_2 in figures 5.6 to 5.9 show a less consistent trend than H_2O and CH_4 and have a low adsorption. This is because CO_2 and H_2 are present in the gas mixture in a much smaller amount than the other two components, which means there are less molecules of CO_2 and H_2 available to be adsorbed. Furthermore, as can be seen for several zeolites, the adsorption of CO_2 and H_2 drops even further at higher pressures, since water dominates the adsorption.

5.2. Adsorption isotherms in all-silica zeolites at 635 K

This section shows the adsorption isotherms of H_2O, CH_4, CO_2 and H_2 in the zeolites at 635 K, respectively. The zeolites are all-silica and contain no aluminum.

5.2.1. Adsorption isotherm of H_2O

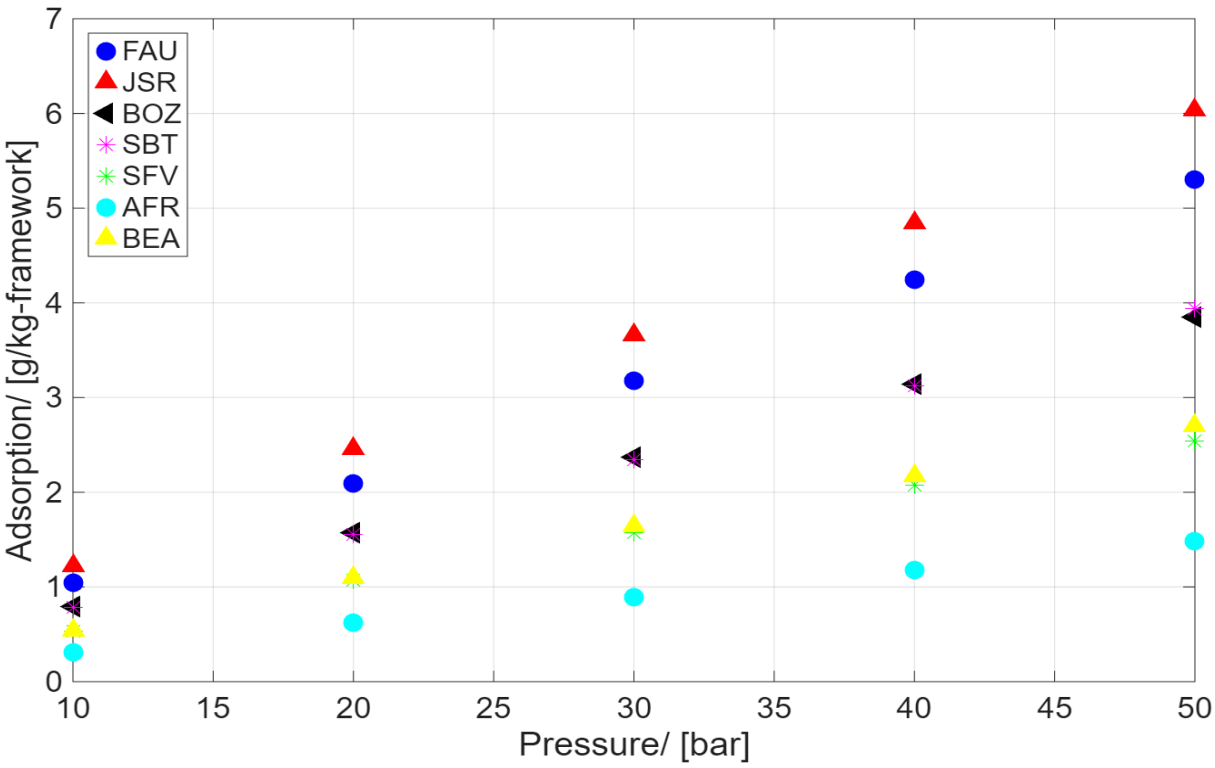

Figure 5.10: Adsorption of H_2O in zeolites that have similar properties as FAU and large internal pores in the pressure range 10 - 50 bar at T = 635 K.

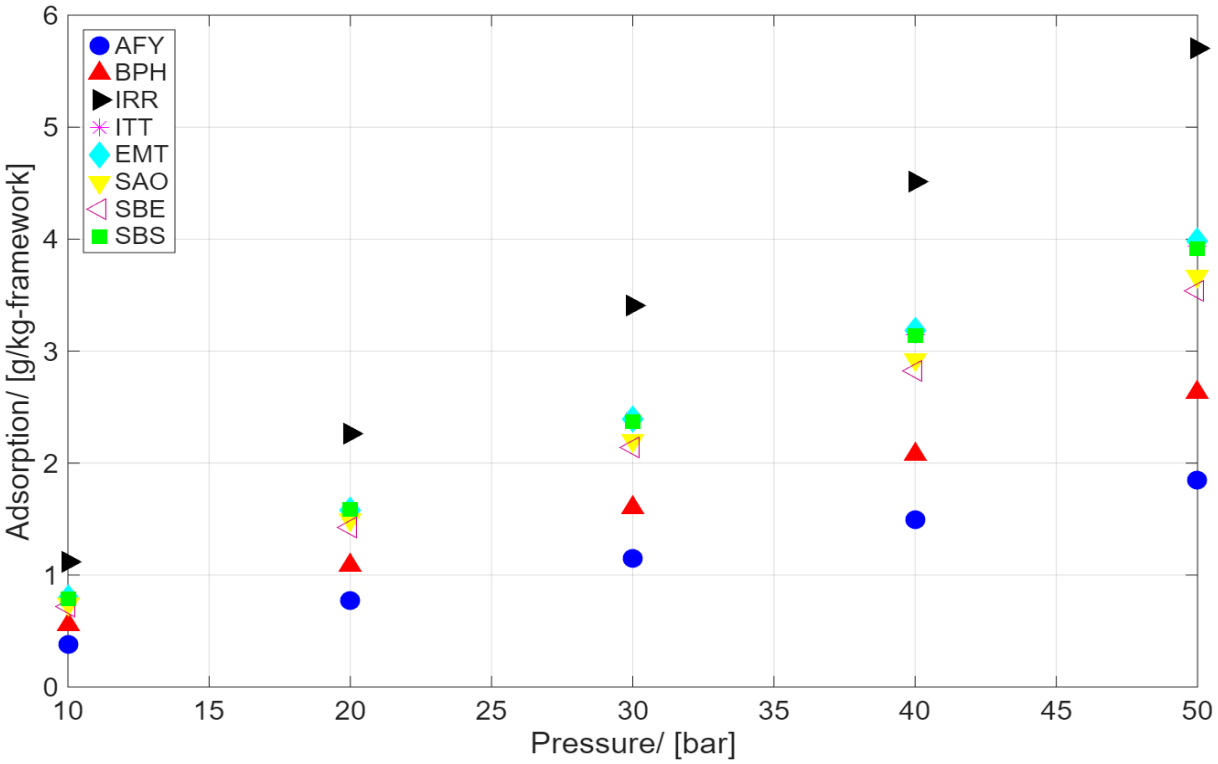

Figure 5.11: Adsorption of H_2O in zeolites that have large external pores and both large in- and external pores in the pressure range 10 - 50 bar at T = 635 K.

5.2.2. Adsorption isotherm of CH_4

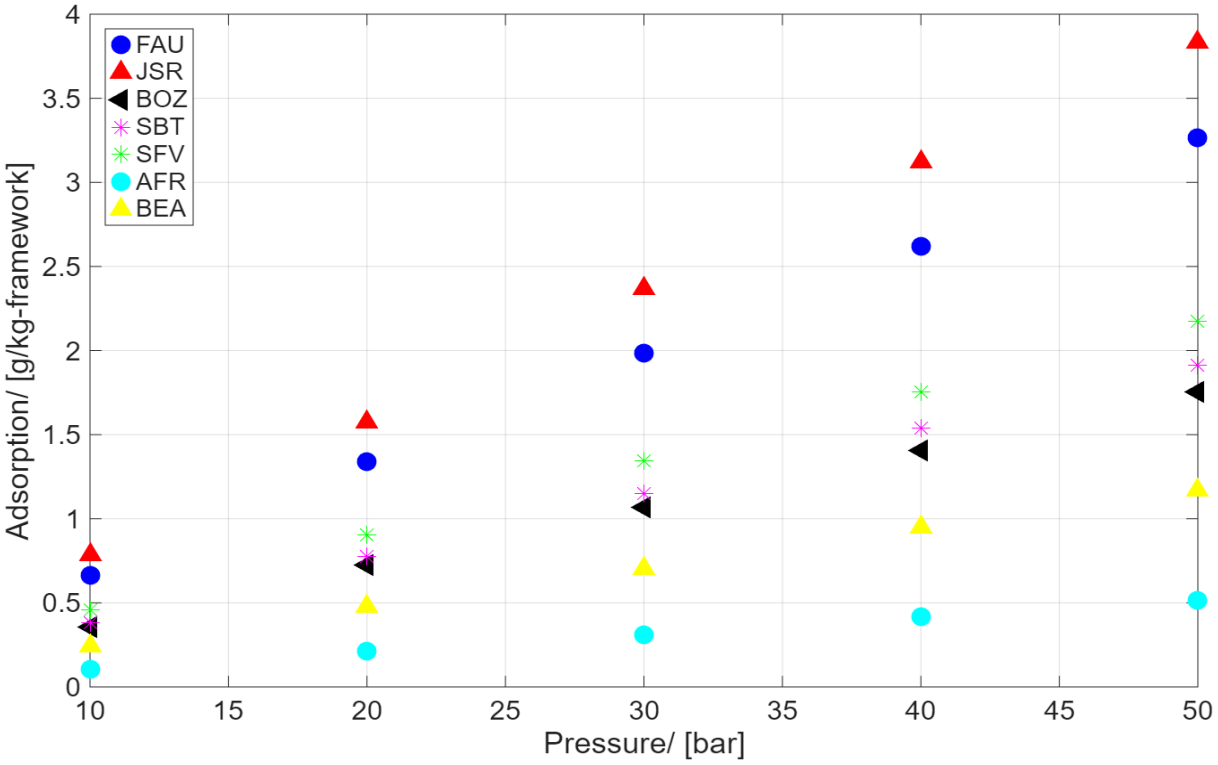

Figure 5.12: Adsorption of CH_4 in zeolites that have similar properties as FAU and large internal pores in the pressure range 10 - 50 bar at T = 635 K.

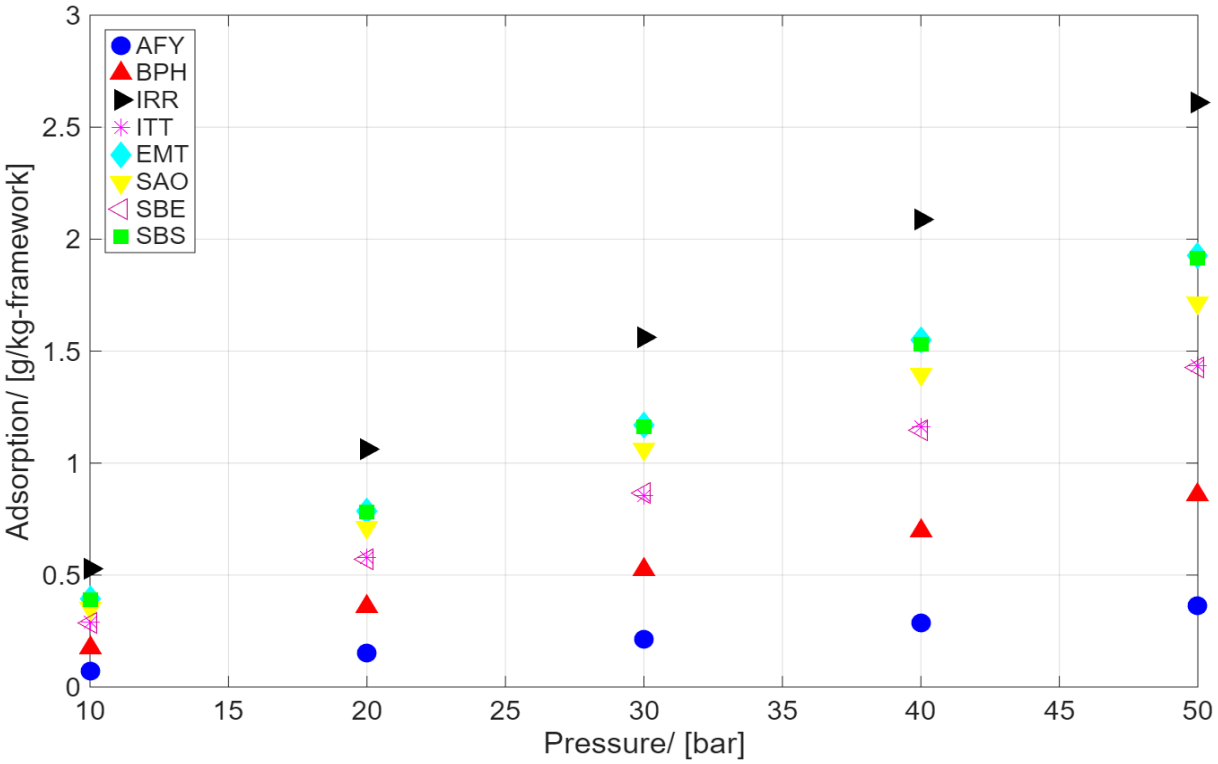

Figure 5.13: Adsorption of CH_4 in zeolites that have large external pores and both large in- and external pores in the pressure range 10 - 50 bar at T = 635 K.

5.2.3. Adsorption isotherms of CO_2

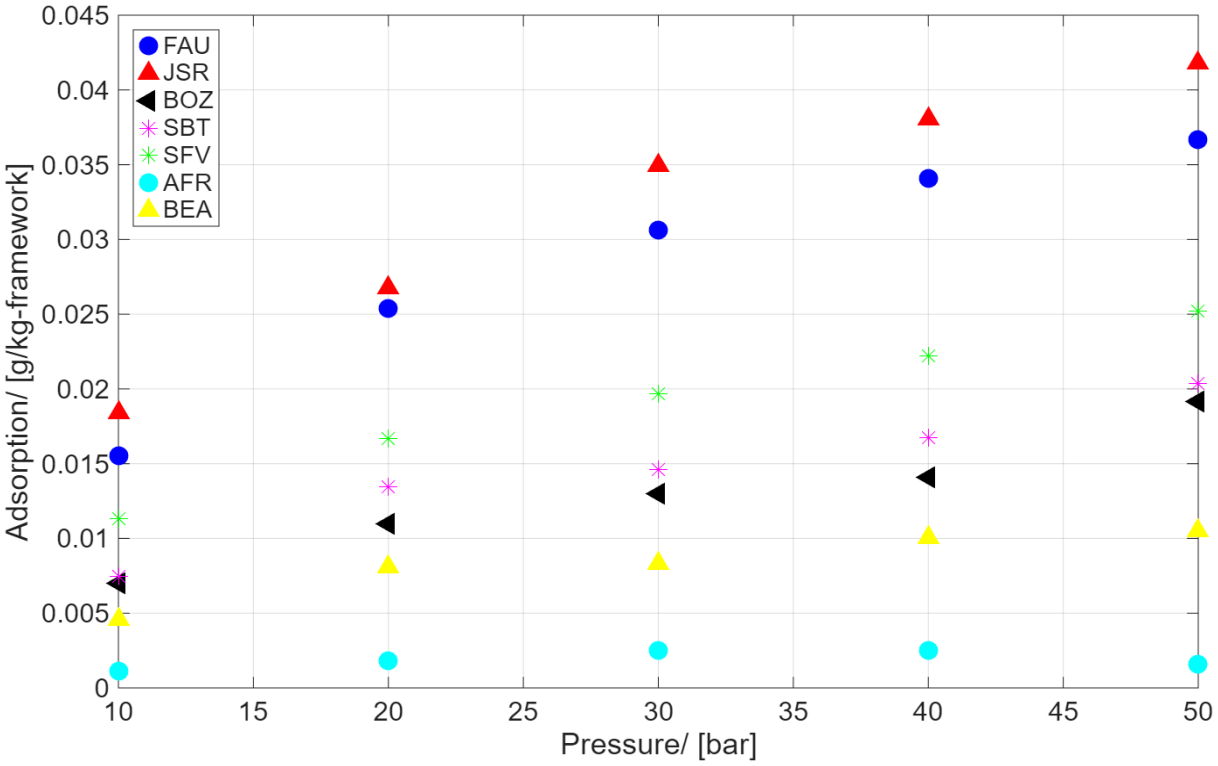

Figure 5.14: Adsorption of CO_2 in zeolites that have similar properties as FAU and large internal pores in the pressure range 10 - 50 bar at T = 635 K.

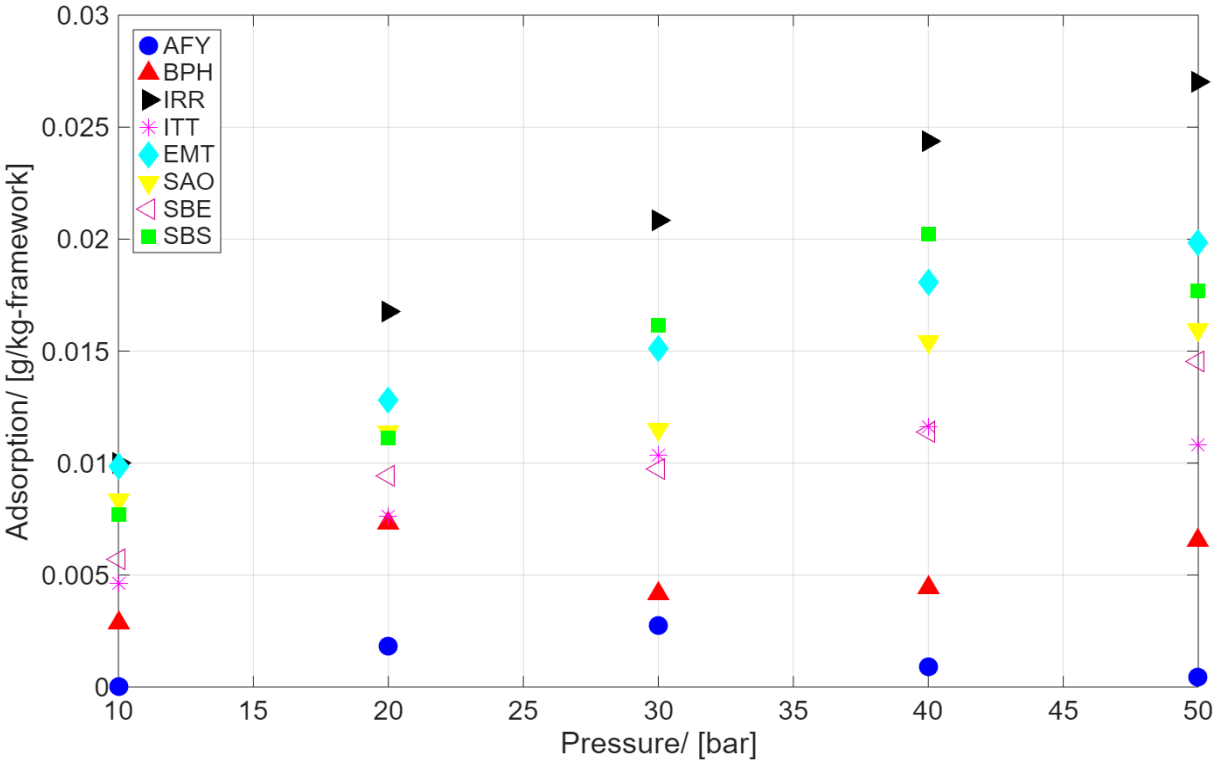

Figure 5.15: Adsorption of CO_2 in zeolites that have large external pores and both large in- and external pores in the pressure range 10 - 50 bar at T = 635 K.

5.2.4. Adsorption isotherms of H_2

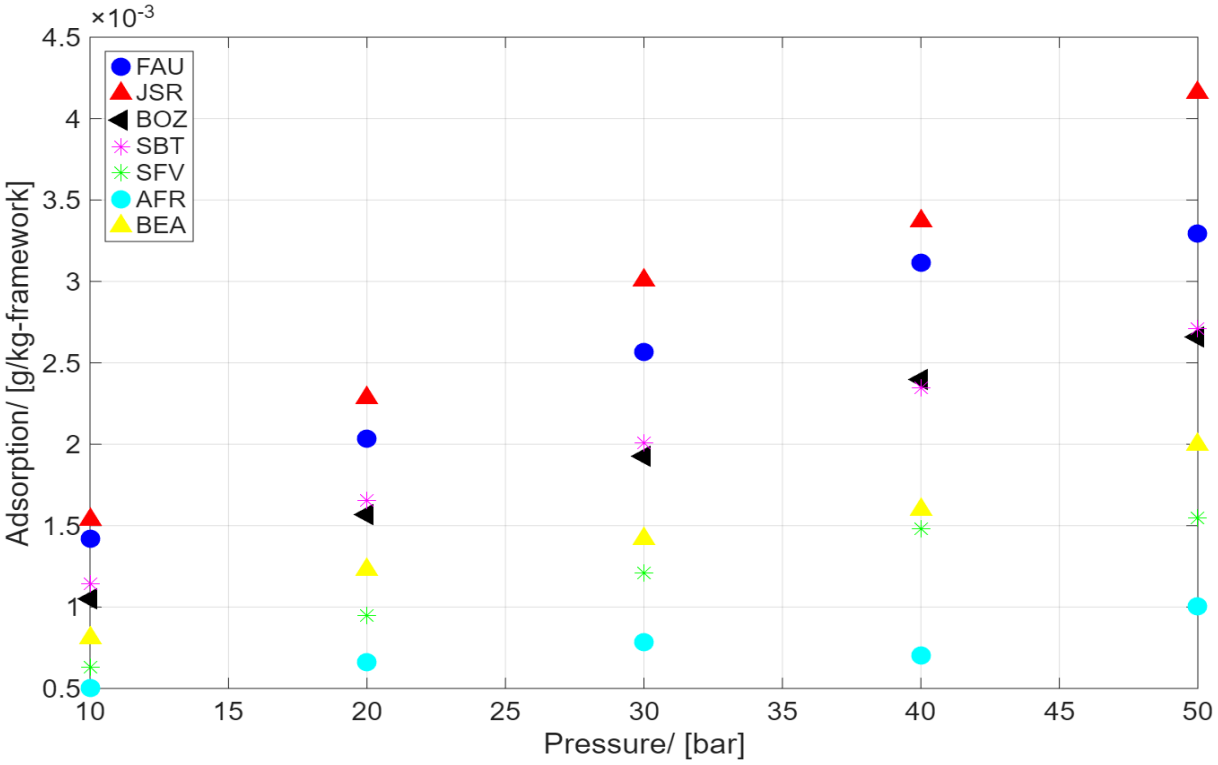

Figure 5.16: Adsorption of H_2 in zeolites that have similar properties as FAU and large internal pores in the pressure range 10 - 50 bar at T = 635 K.

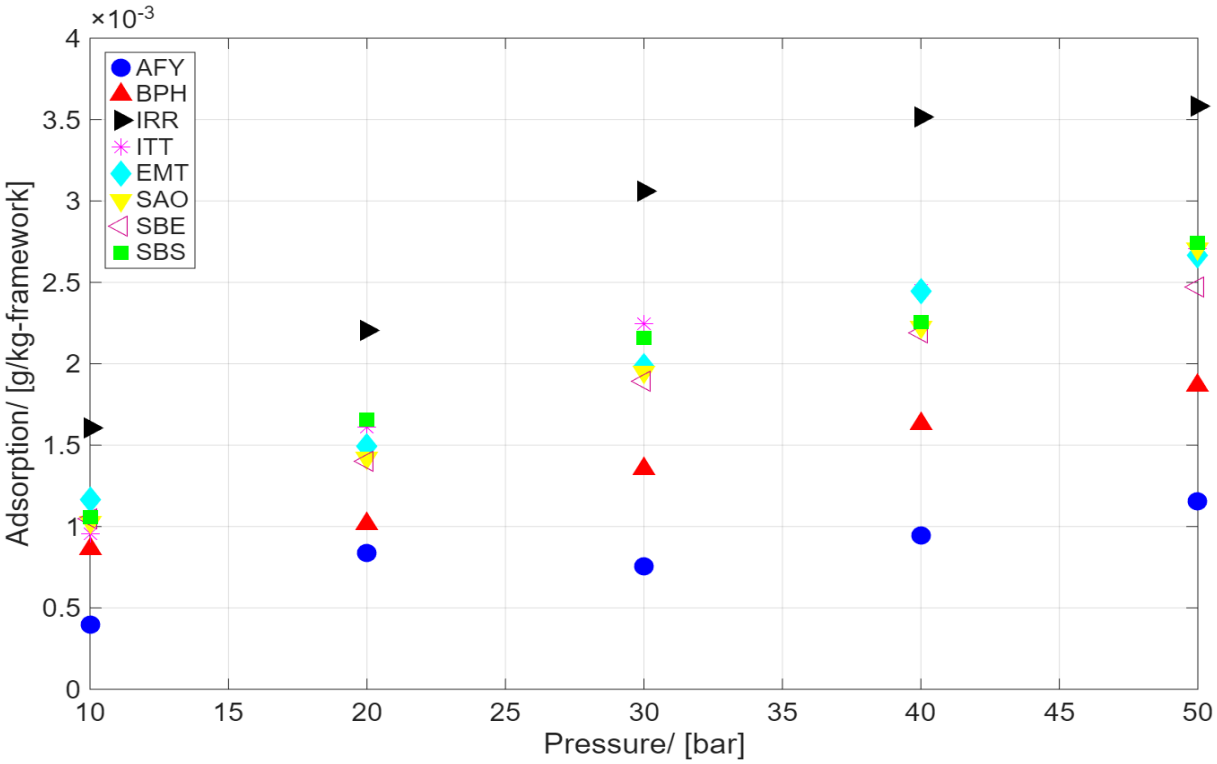

Figure 5.17: Adsorption of H_2 in zeolites that have large external pores and both large in- and external pores in the pressure range 10 - 50 bar at T = 635 K.

As can be seen in the figures 5.10 and 5.11 the water adsorption decreases rapidly as a result of the temperature increase. The reason for this is that adsorption is an exothermic process, so increasing the temperature will lead to an adsorption decrease, according to Le Chatelier's principle. It should be noticed that the zeolites that have a high water adsorption at T = 455 K, such as FAU and EMT, now have a lower adsorption than some other zeolites, such as IRR. This is because at low adsorption, the polar effects of water are less dominant. There is less water in the zeolite, so other water molecules are also less attracted towards the surface and the stable structure in the cages cannot be created. This is also the reason that the other components don't experience the same large decrease in adsorption. Since the water is less dominant, the other components have a higher chance of being adsorbed. Similar to the lower temperatures, the adsorption increase as the pressure increases is also clearly visible in the figures.

5.3. Adsorption in zeolites including aluminum

This section shows the adsorption isotherms of H_2O, CH_4, CO_2 and H_2 in several zeolite types at 455 K, respectively. The zeolites have a Si/Al ratio between 15 and 27. Table 3.4 shows the exact ratio for each zeolite.

5.3.1. Adsorption isotherm of H_2O

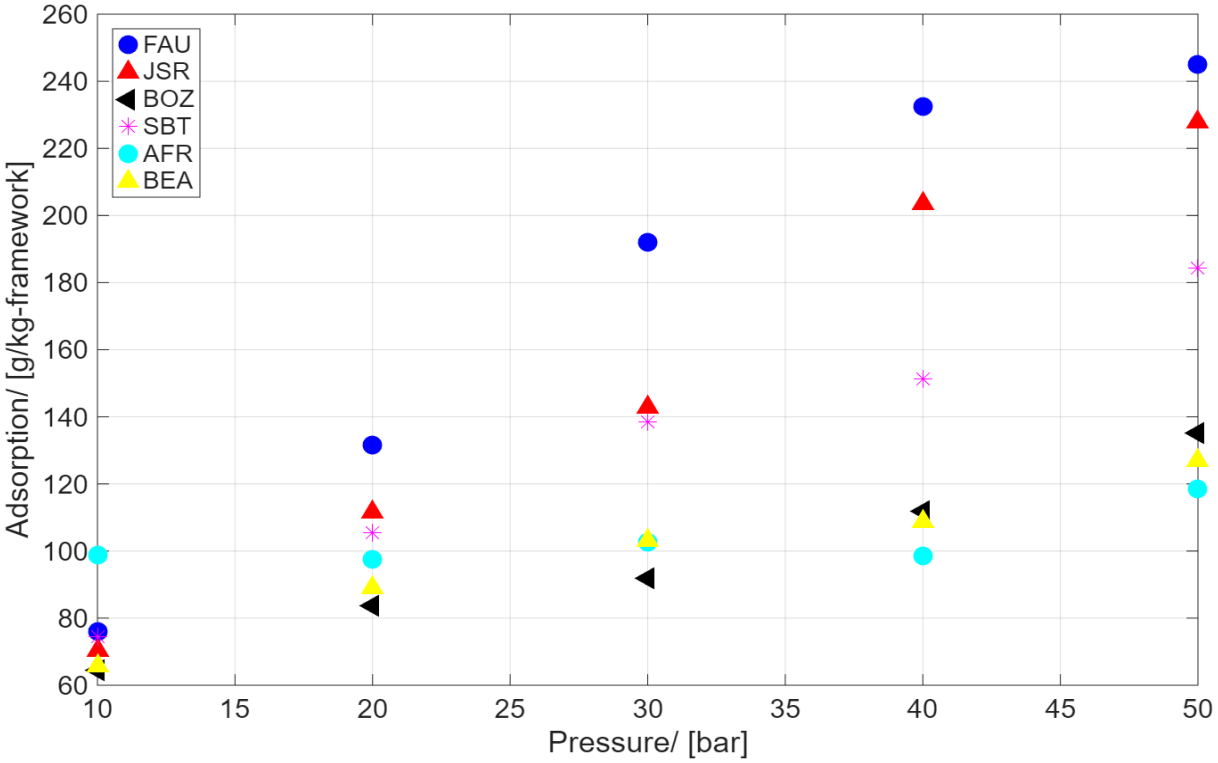

Figure 5.18: Adsorption of H_2O in zeolites that have similar properties as FAU and large internal pores in the pressure range 10 - 50 bar at T = 455 K and Si/Al ratio between 15-25.

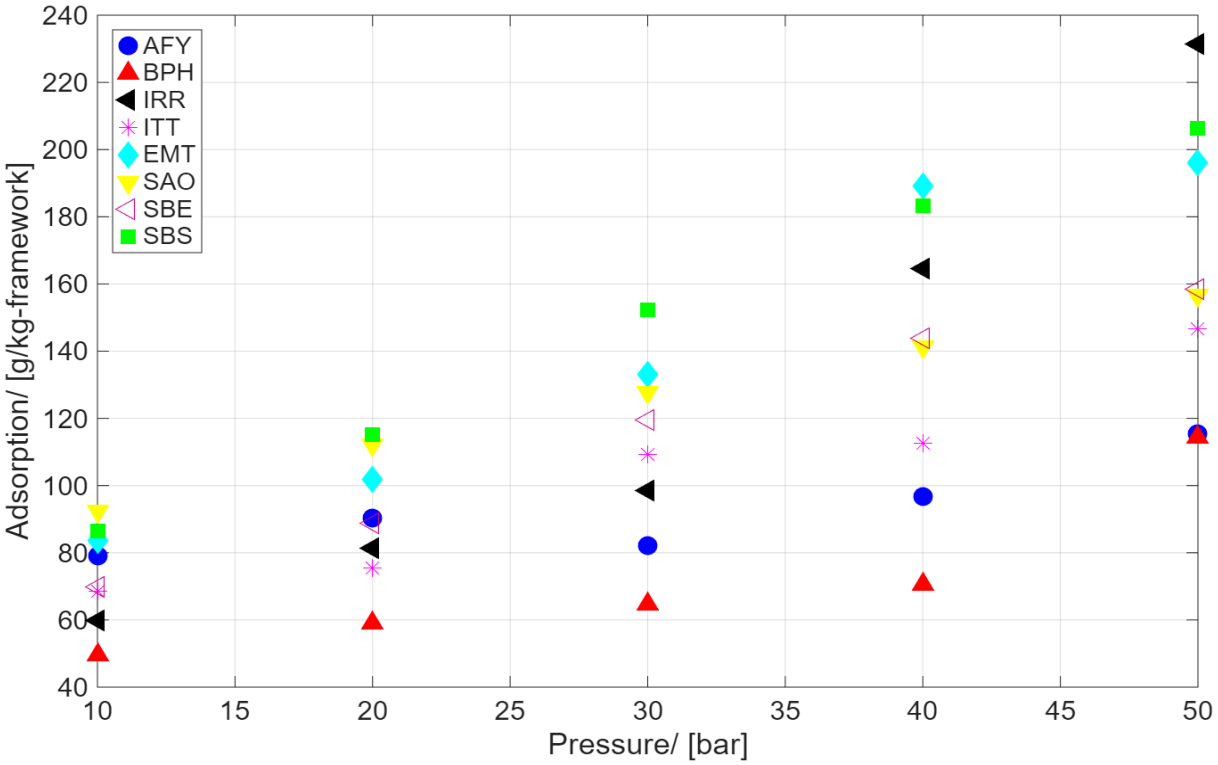

Figure 5.19: Adsorption of H_2O in zeolites that have large external pores and both large in- and external pores in the pressure range 10 - 50 bar at T = 455 K and Si/Al ratio between 15-25.

5.3.2. Adsorption isotherm of CH_4

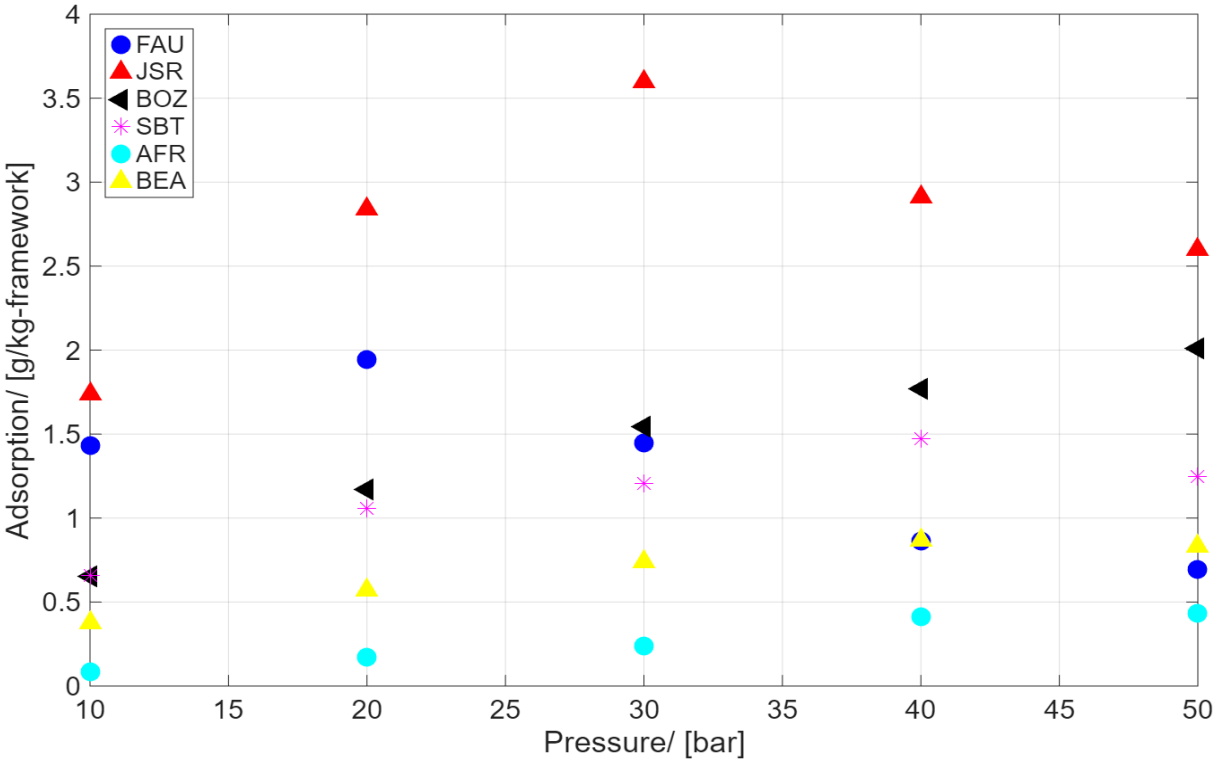

Figure 5.20: Adsorption of CH_4 in zeolites that have similar properties as FAU and large internal pores in the pressure range 10 - 50 bar at T = 455 K and Si/Al ratio between 15-25.

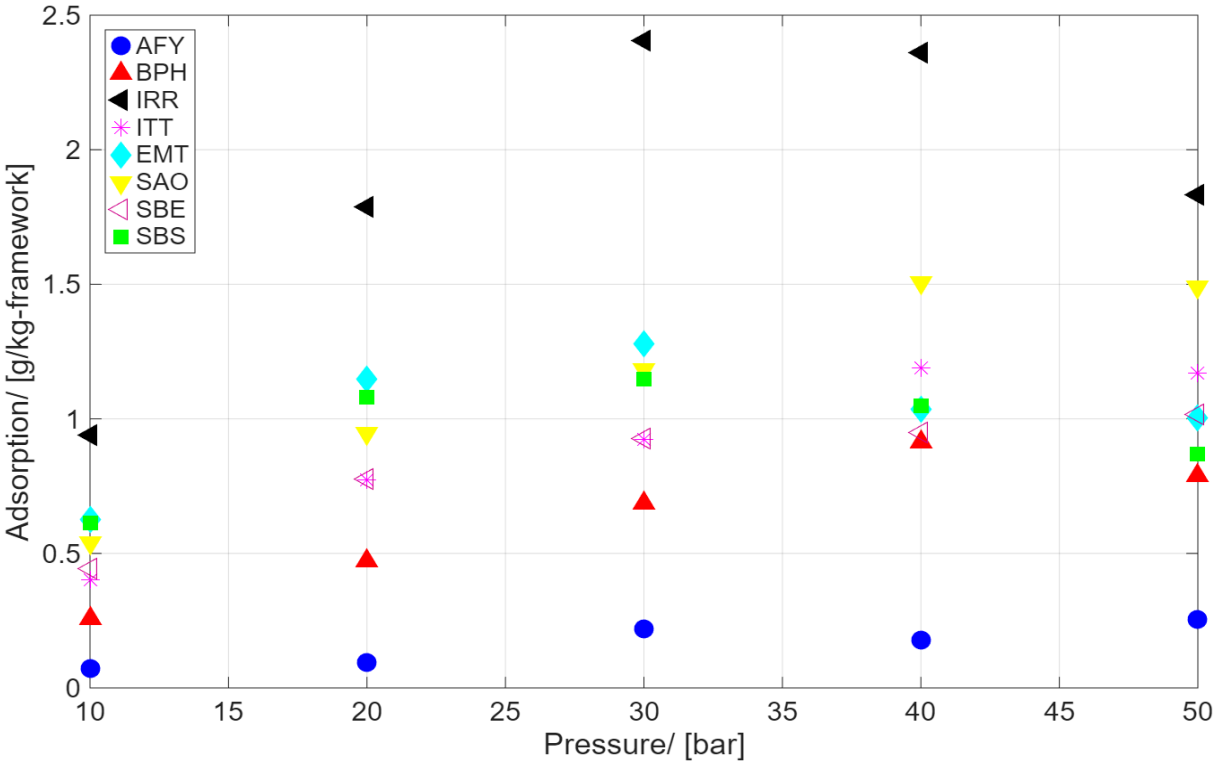

Figure 5.21: Adsorption of CH_4 in zeolites that have large external pores and both large in- and external pores in the pressure range 10 - 50 bar at T = 455 K and Si/Al ratio between 15-25.

5.3.3. Adsorption isotherms of CO_2

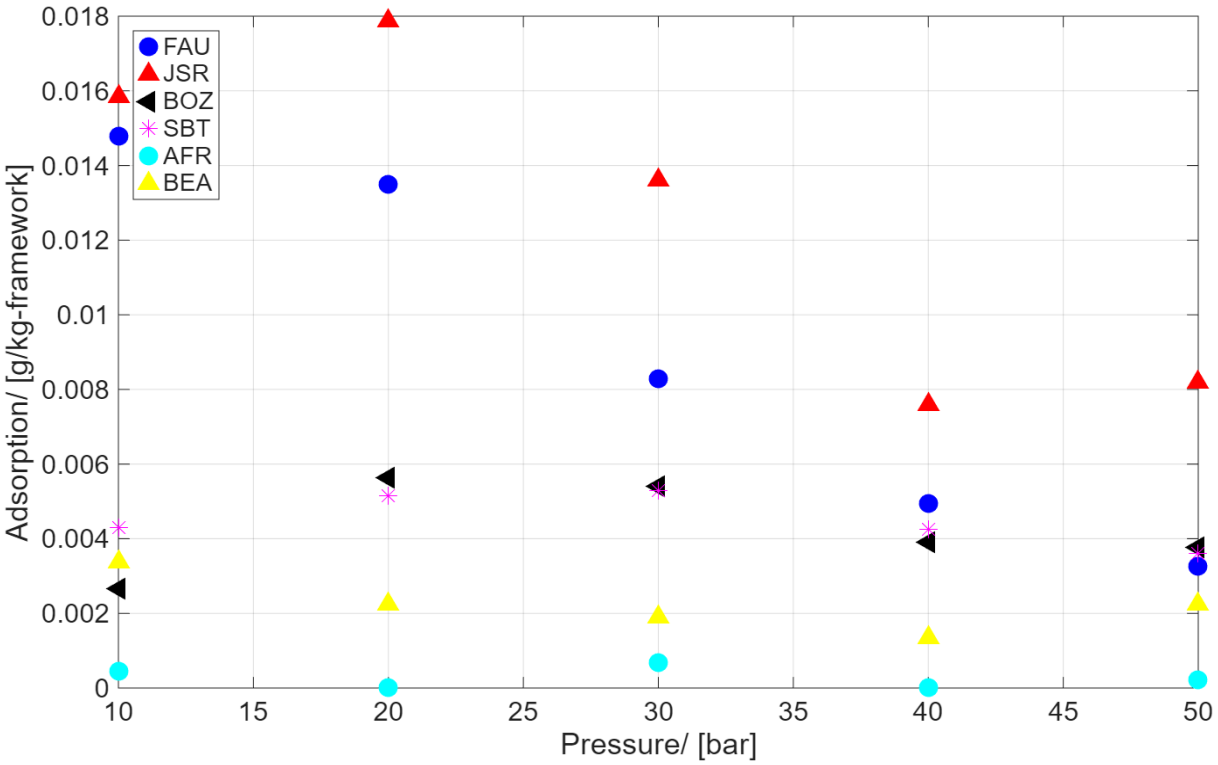

Figure 5.22: Adsorption of CO_2 in zeolites that have similar properties as FAU and large internal pores in the pressure range 10 - 50 bar at T = 455 K and Si/Al ratio between 15-25.

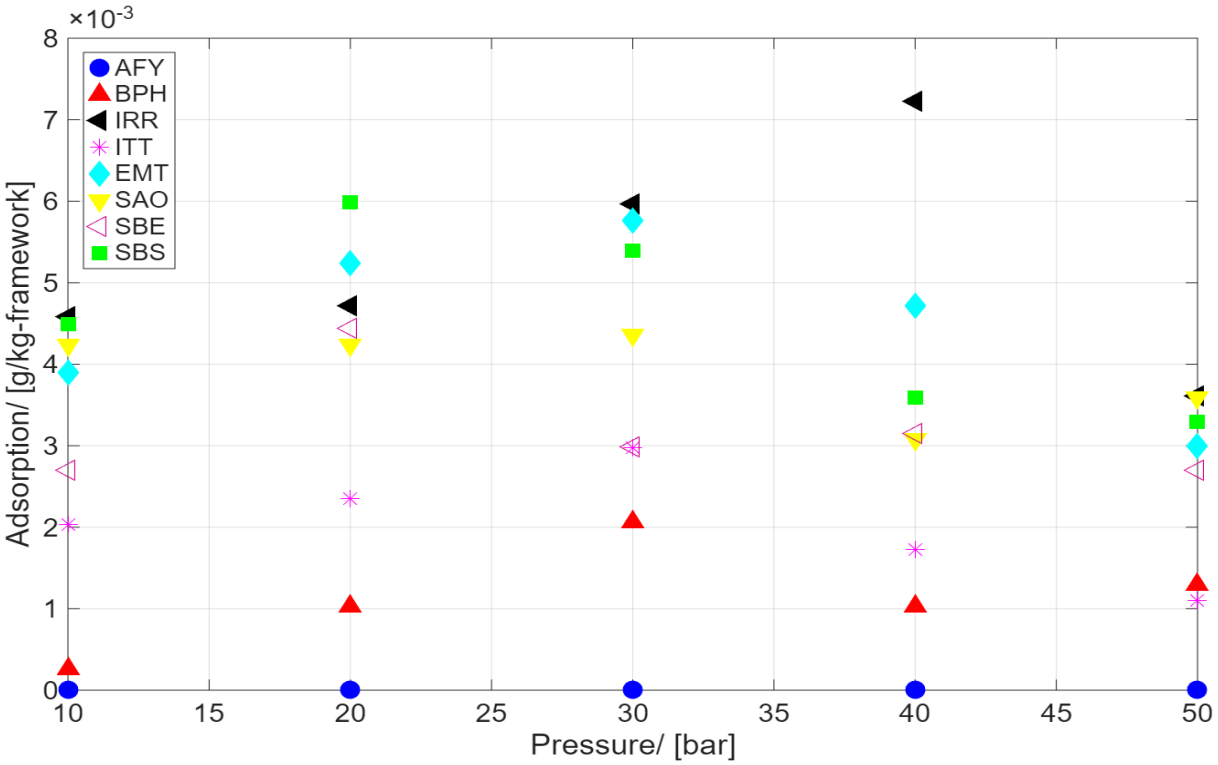

Figure 5.23: Adsorption of CO_2 in zeolites that have large external pores and both large in- and external pores in the pressure range 10 - 50 bar at T = 455 K and Si/Al ratio between 15-25.

5.3.4. Adsorption isotherms of H_2

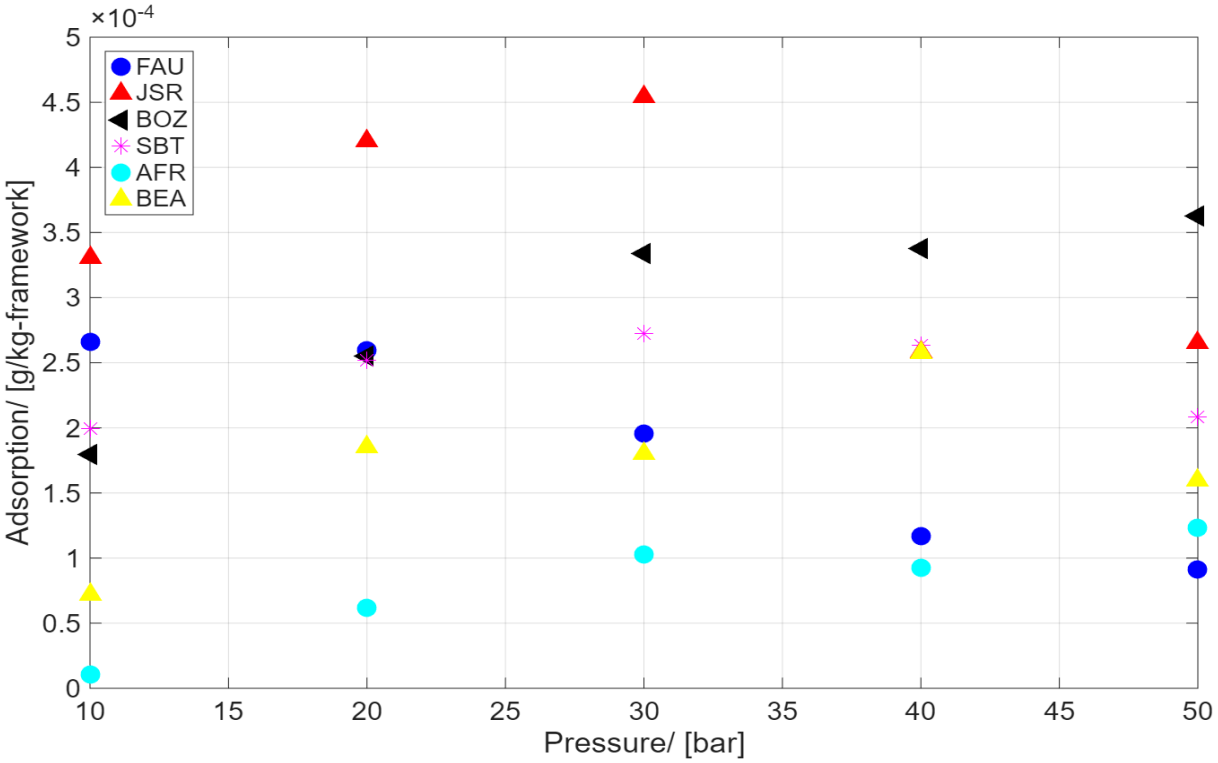

Figure 5.24: Adsorption of H_2 in zeolites that have similar properties as FAU and large internal pores in the pressure range 10 - 50 bar at T = 455 K and Si/Al ratio between 15-25.

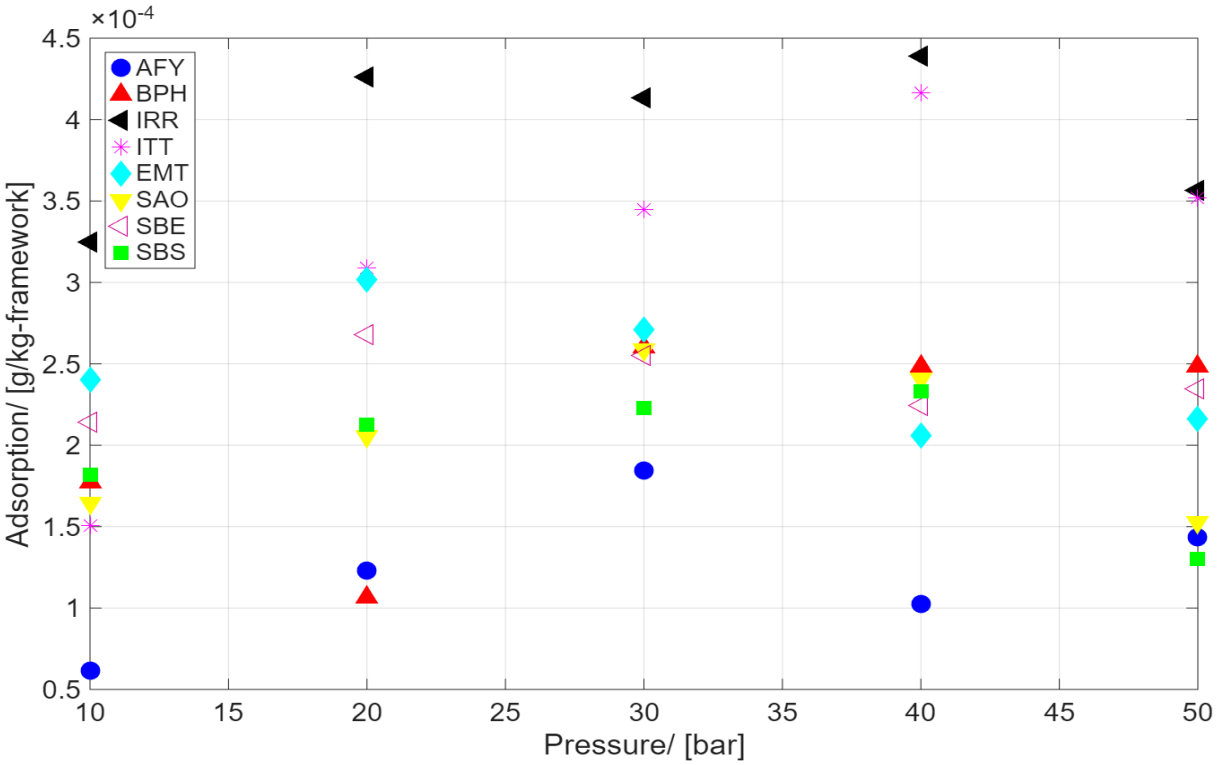

Figure 5.25: Adsorption of H_2 in zeolites that have large external pores and both large in- and external pores in the pressure range 10 - 50 bar at T = 455 K and Si/Al ratio between 15-25.

The figures 5.18 and 5.19 show that adding aluminum drastically increases the water adsorption capacity for each zeolite. This corresponds to expectations, since it introduces a negative framework charge, which is compensated by adding cations. This creates strong electrostatic fields that attract water, since water has a large dipole moment and is highly polar. Additionally, Al-O bonds are more polar than Si-O bonds and thus attract water as well. Water molecules attract other molecules and form stable structures, so the adsorption increases further. As explained in chapter 5.1.4, other components are excluded from adsorption as the water adsorption increases, which is shown in figures 5.20 to 5.25 where a decrease in adsorption can be seen for certain zeolites, such as FAU and JSR.

5.4. Enthalpy of adsorption

This section shows the enthalpy of adsorption for each zeolite at both temperatures. The enthalpy of adsorption is the amount of energy released when molecules attach to the surface. Usually, $\Delta H < 0$, since adsorption is an exothermic process. A large enthalpy of adsorption means a strong attachment to the surface, which is an indication that desorption is difficult. As explained in chapter 3.7, an enthalpy of adsorption between -8 to -40 kJ/mol indicates that the component can be adsorbed easily. Figures 5.26 to 5.33 show the enthalpy of adsorption for each zeolite at T = 455 K and T = 635 K. Each zeolite has an enthalpy of adsorption in the range -8 to -40 kJ/mol, denoted as the green area, which indicates that adsorption is possible for each type. The yellow area indicates where desorption becomes moderate to hard and the red area indicates where desorption becomes very hard to nearly impossible.

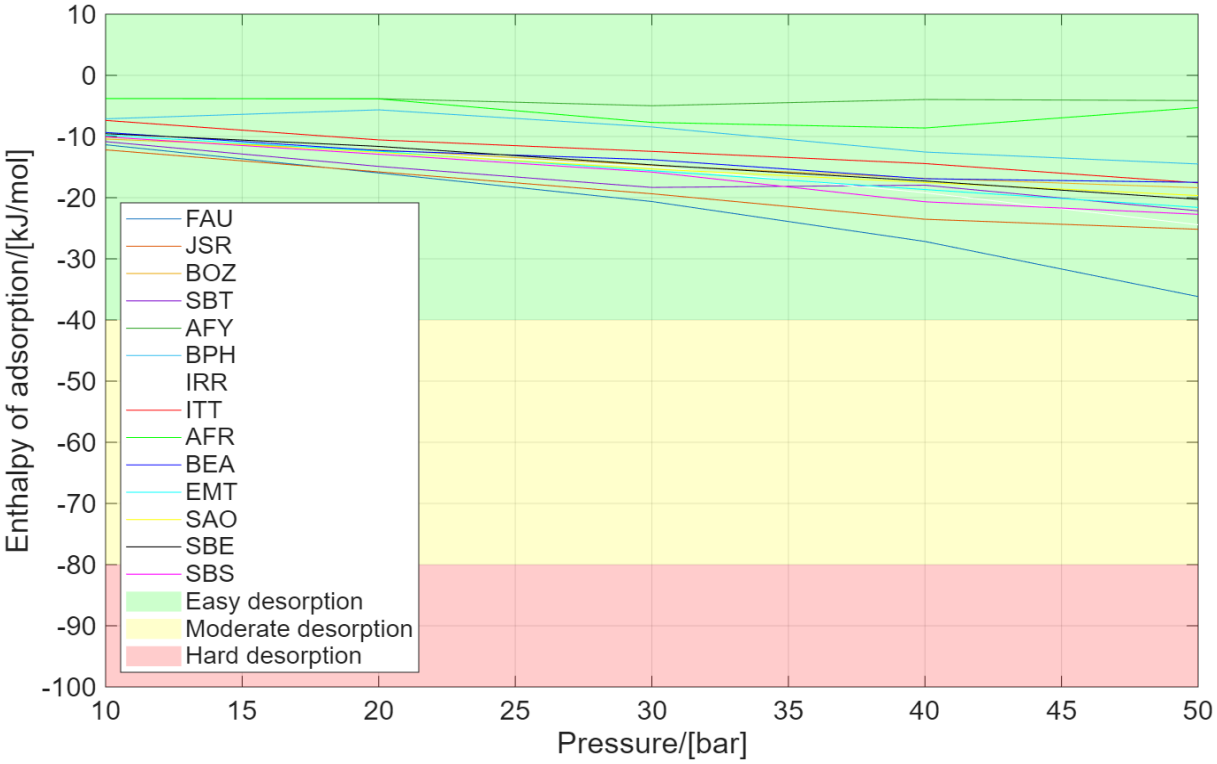

Figure 5.26: Enthalpy of adsorption of H_2O in the pressure range 10 - 50 bar at T = 455 K.

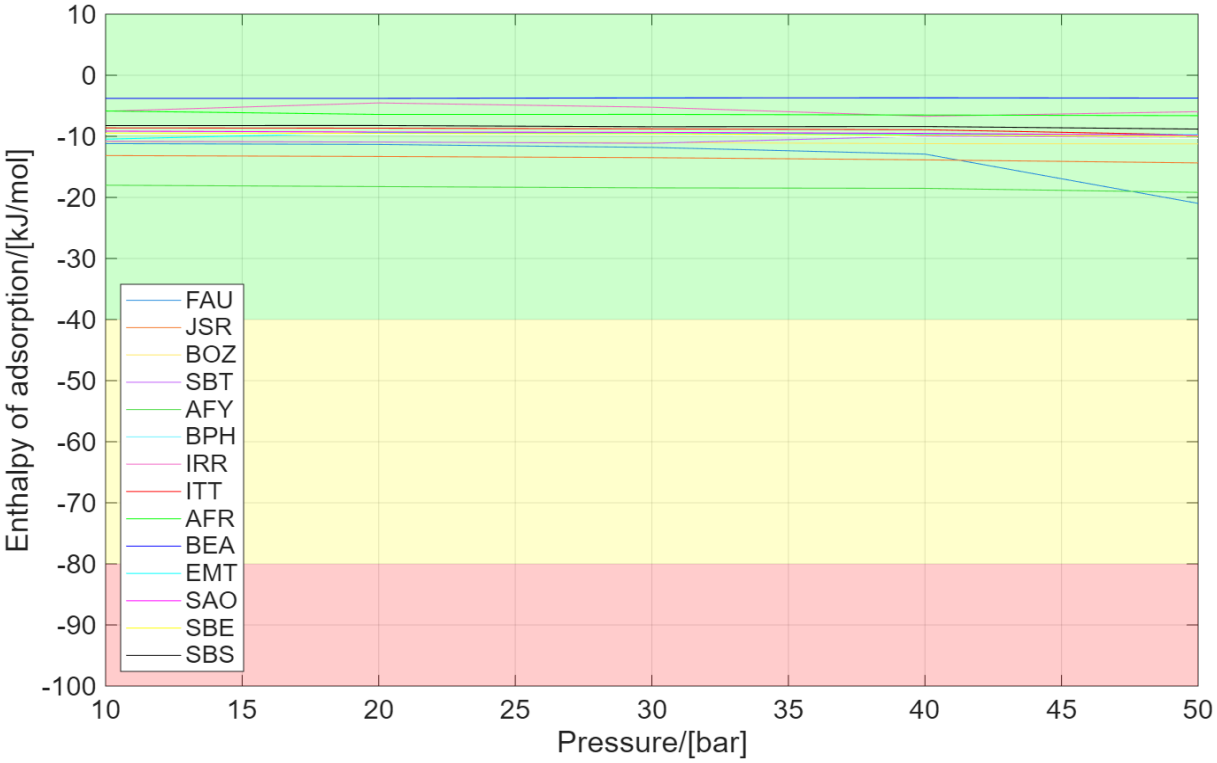

Figure 5.27: Enthalpy of adsorption of CH_4 in the pressure range 10 - 50 bar at T = 455 K. For the green-yellow-red region, see Figure 5.26.

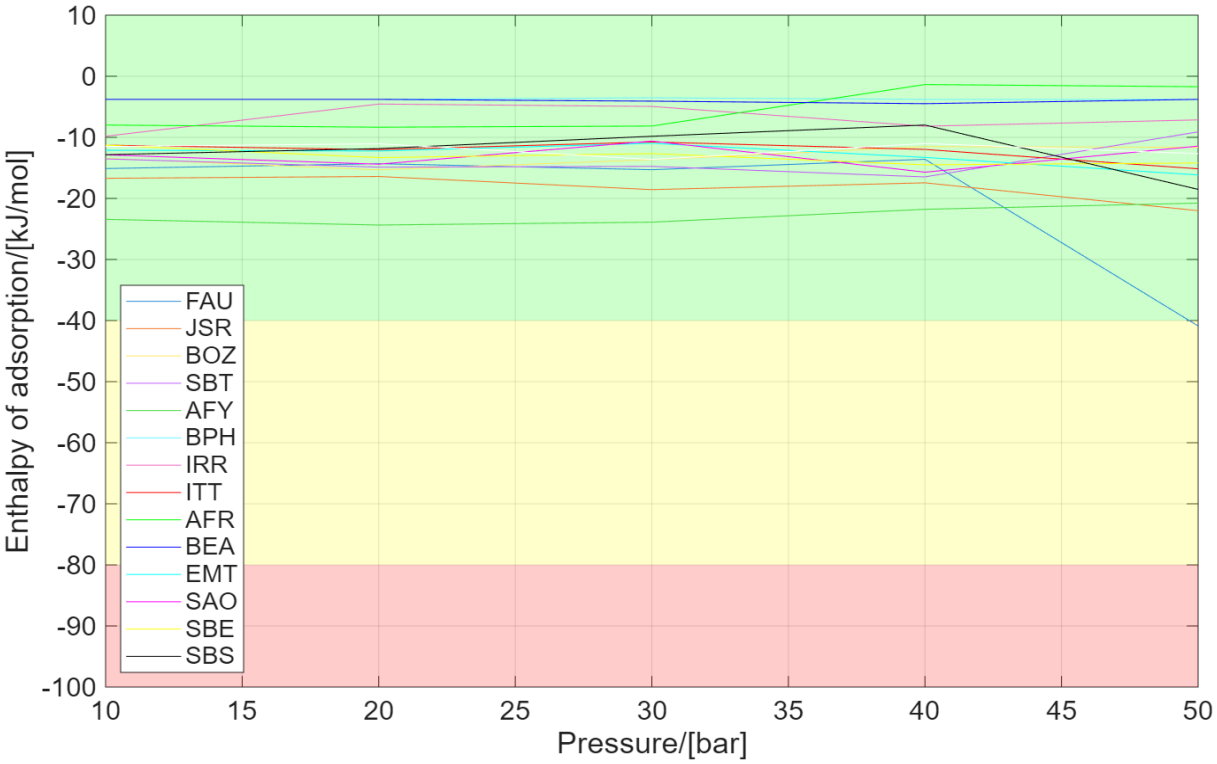

Figure 5.28: Enthalpy of adsorption of CO_2 in the pressure range 10 - 50 bar at T = 455 K. For the green-yellow-red region, see Figure 5.26.

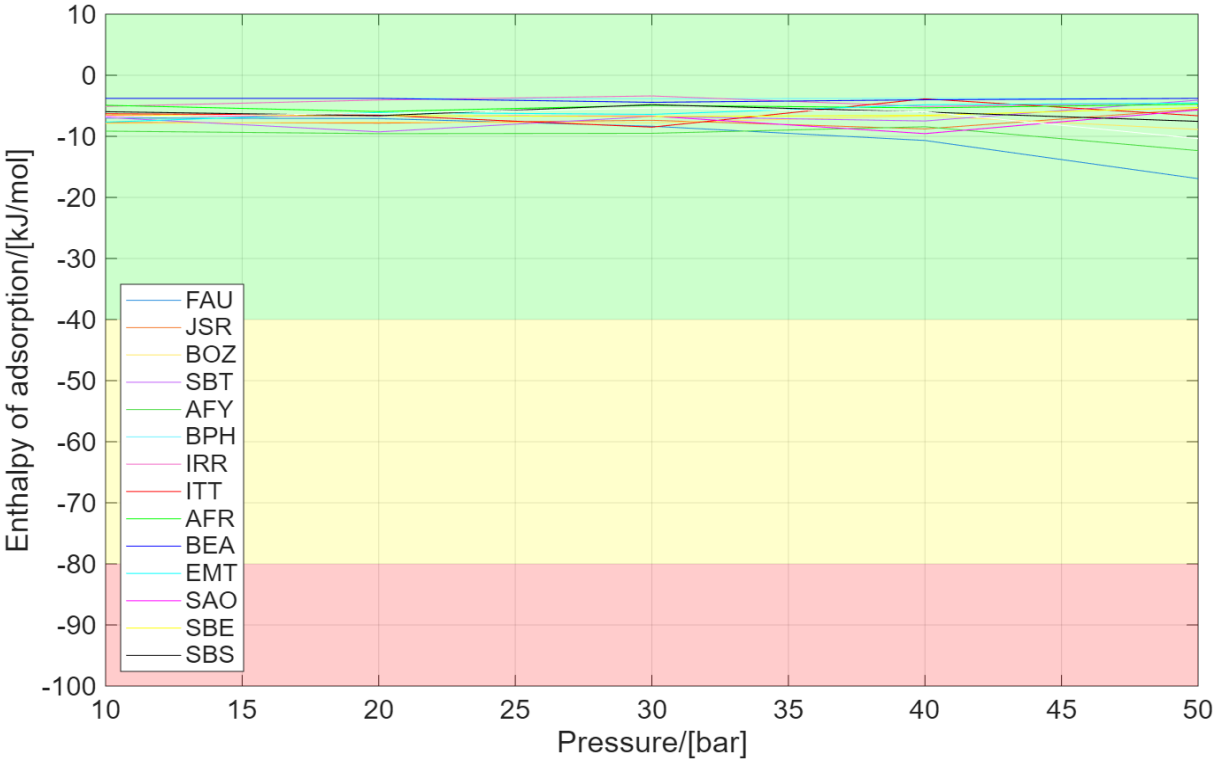

Figure 5.29: Enthalpy of adsorption of H_2 in the pressure range 10 - 50 bar at T = 455 K. For the green-yellow-red region, see Figure 5.26.

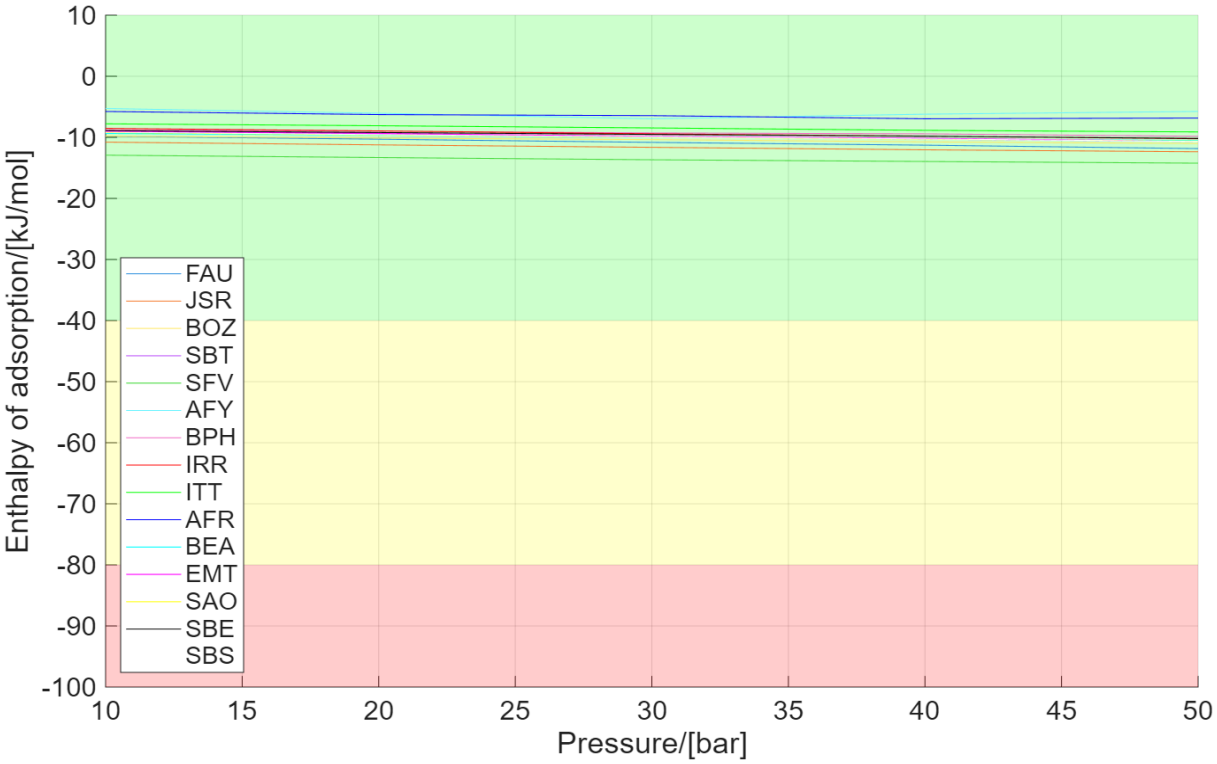

Figure 5.30: Enthalpy of adsorption of H_2O in the pressure range 10 - 50 bar at T = 635 K. For the green-yellow-red region, see Figure 5.26.

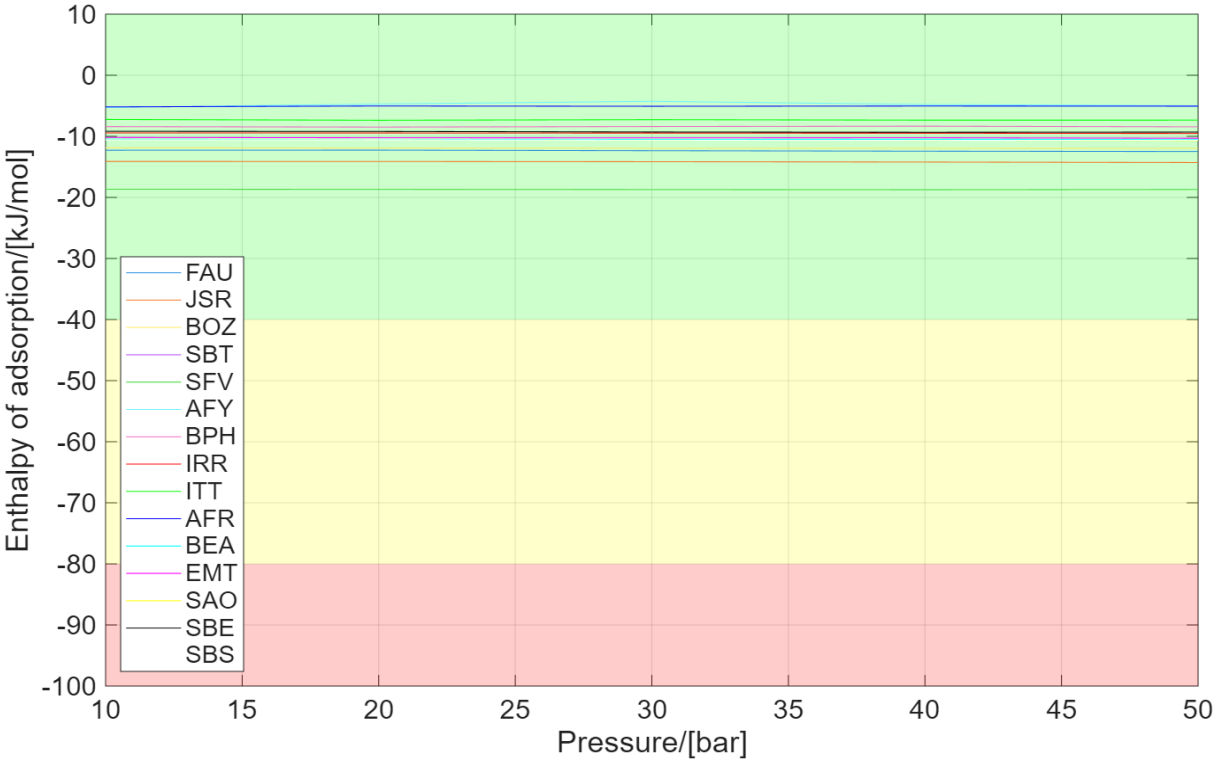

Figure 5.31: Enthalpy of adsorption of CH_4 in the pressure range 10 - 50 bar at T = 635 K. For the green-yellow-red region, see Figure 5.26.

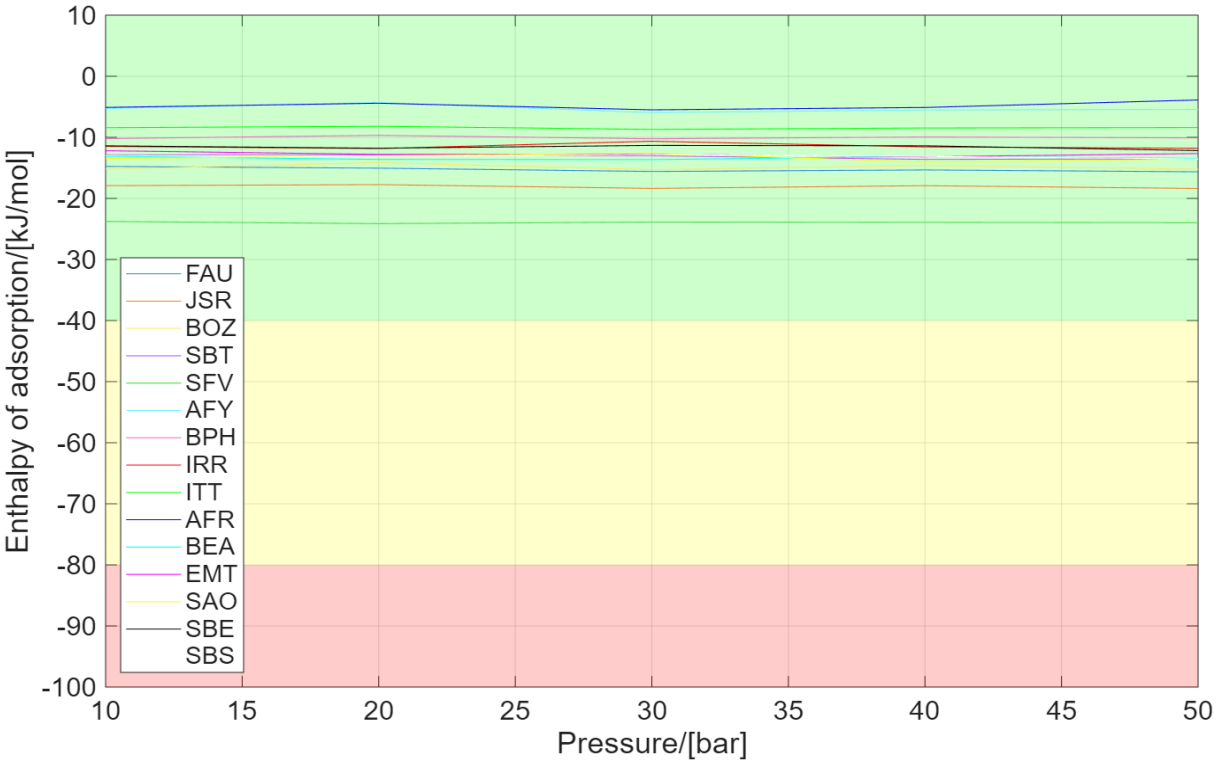

Figure 5.32: Enthalpy of adsorption of CO_2 in the pressure range 10 - 50 bar at T = 635 K. For the green-yellow-red region, see Figure 5.26.

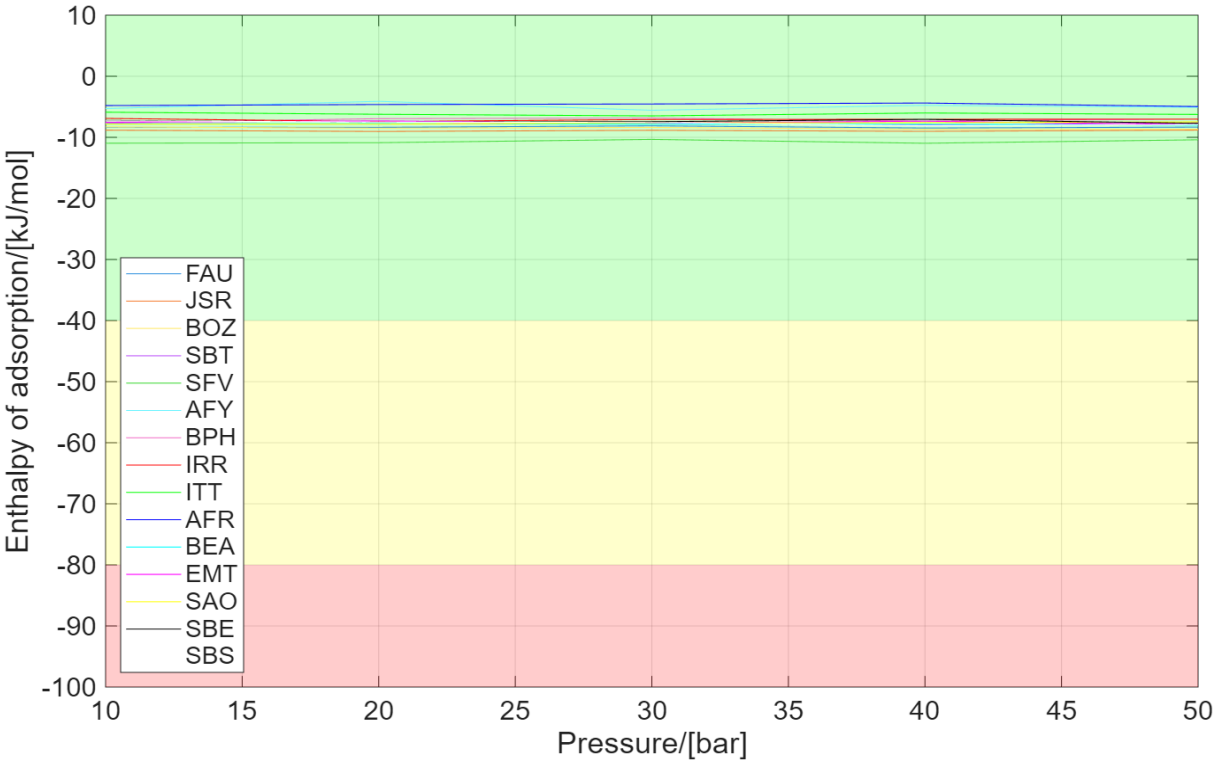

Figure 5.33: Enthalpy of adsorption of H_2 in the pressure range 10 - 50 bar at T = 635 K. For the green-yellow-red region, see Figure 5.26.

5.5. Co-adsorption of CH_4 & CO_2

Figures 5.34 and 5.35 shows the ratio between H_2O and CH_4 adsorbed in each zeolite at 455 K and a pressure of 10 and 50 bar, respectively.

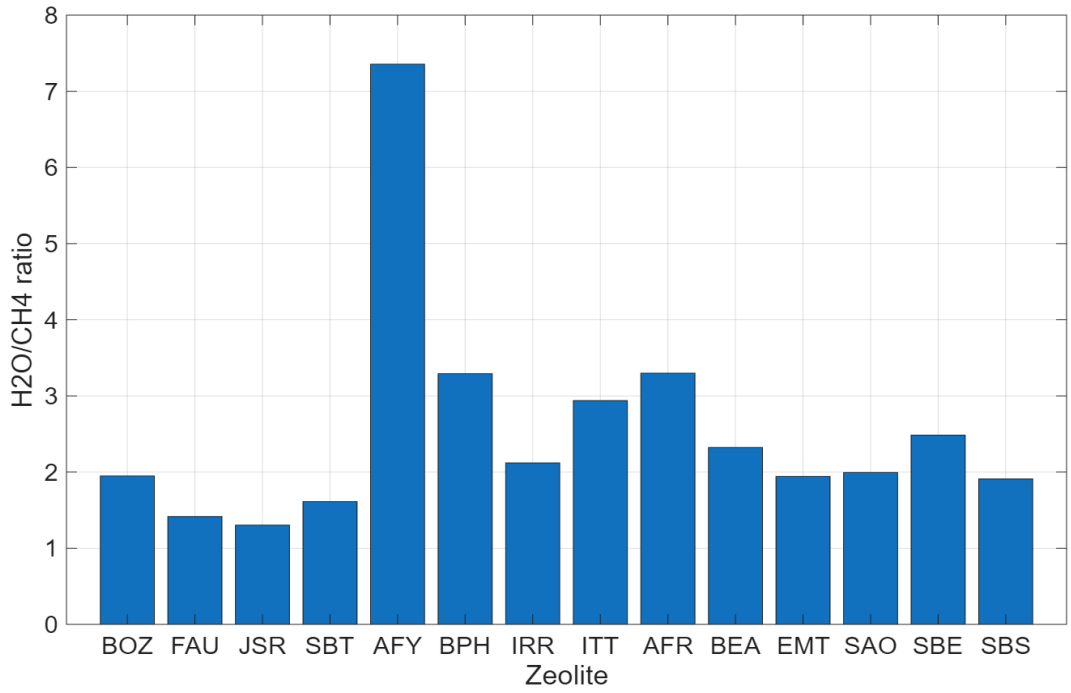

Figure 5.34: Ratio of H_2O and CH_4 adsorbed in each zeolite at 455 K and 10 bar.

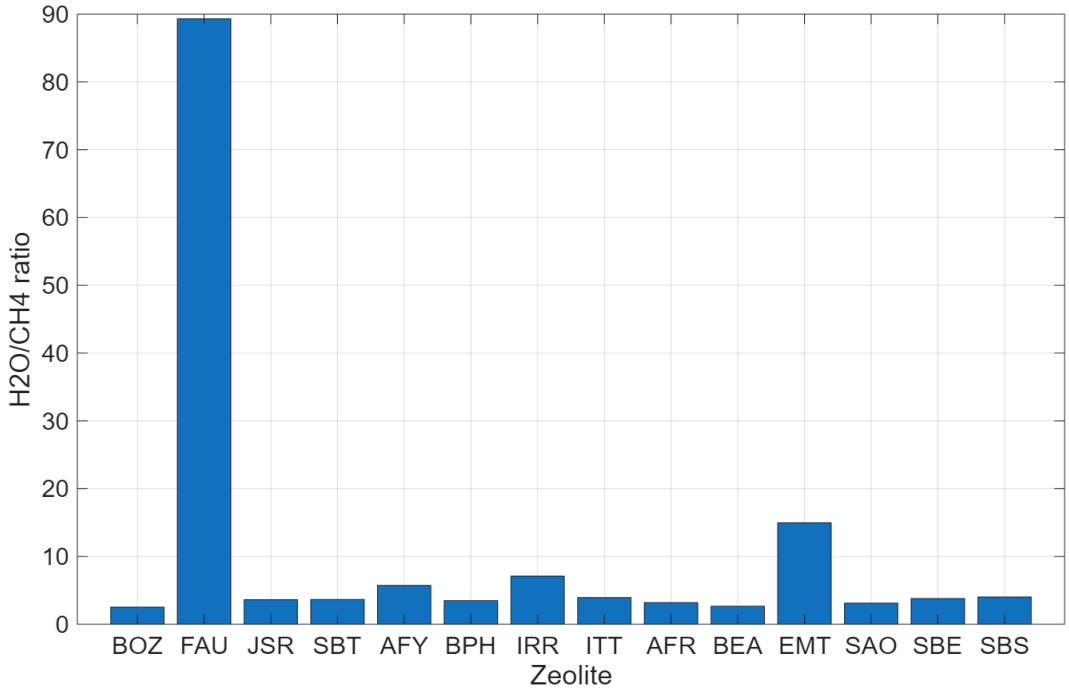

Figure 5.35: Ratio of H_2O and CH_4 adsorbed in each zeolite at 455 K and 50 bar.

The figures show that for all zeolites, the adsorption of water is higher than methane. When increasing the pressure, the ratio increases for EMT, IRR and FAU. For the other zeolites, the ratio remains roughly the same or increases slightly. This shows that for certain zeolites, the increase in water adsorption excludes the adsorption of other components. It also shows that at higher pressures FAU, EMT and IRR are the most suitable zeolites when a low co-adsorption of methane is desired.
Figures 5.36 and 5.37 shows the ratio between H_2O and CO_2 adsorbed in each zeolite at 455 K and a pressure of 10 and 50 bar, respectively.

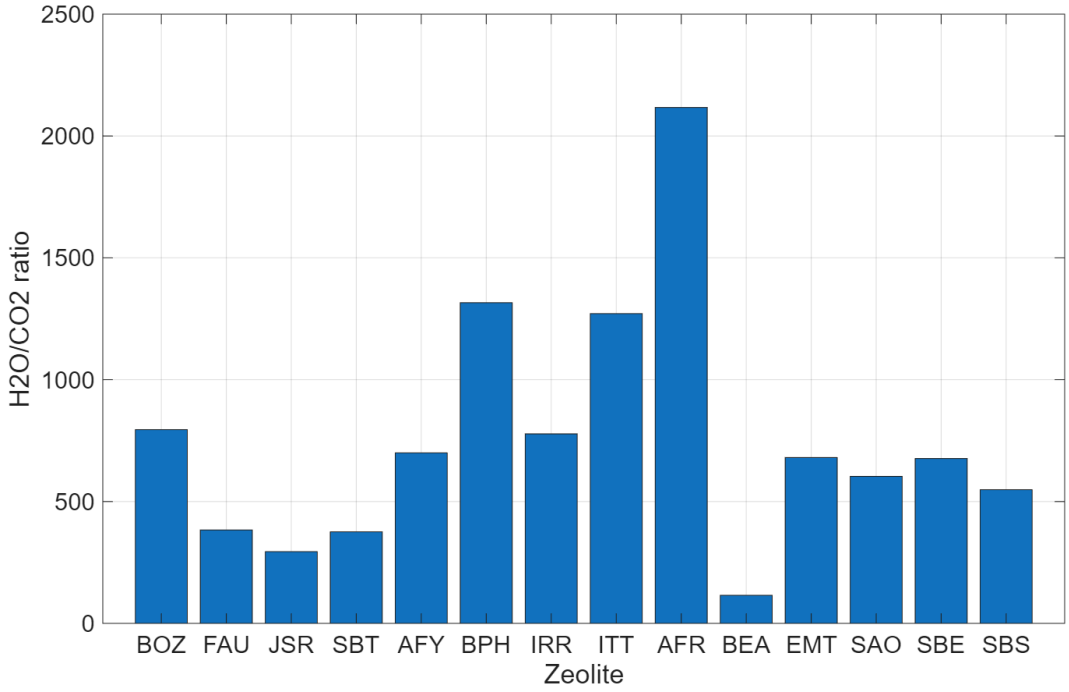

Figure 5.36: Ratio of H_2O and CO_2 adsorbed in each zeolite at 455 K and 10 bar.

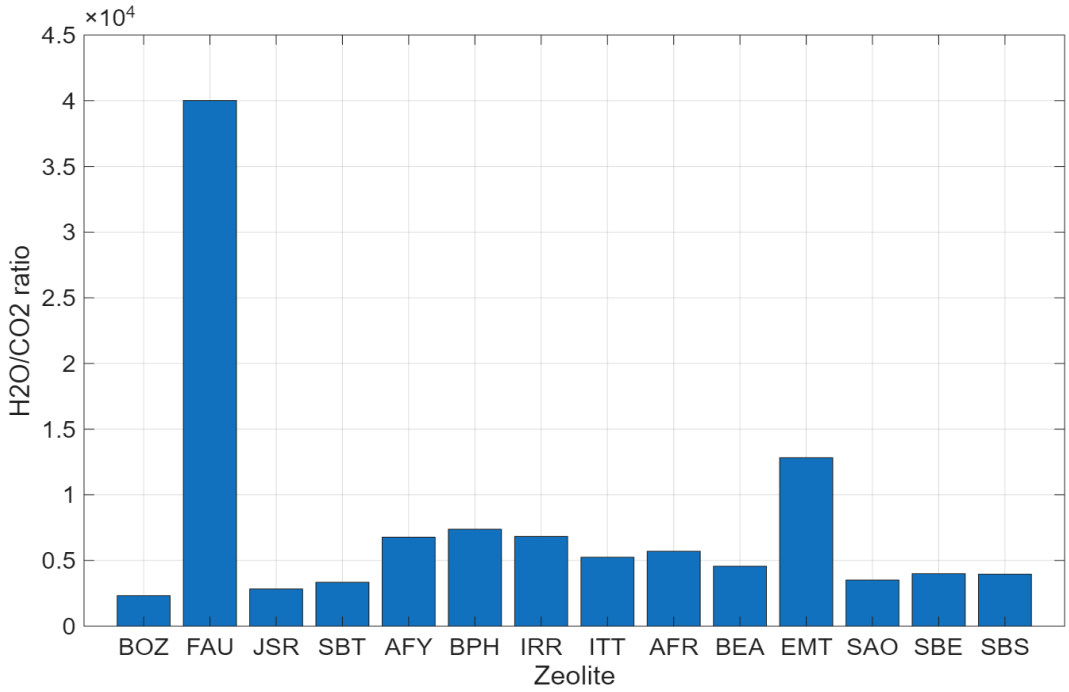

Figure 5.37: Ratio of H_2O and CO_2 adsorbed in each zeolite at 455 K and 50 bar.

The figures show that at both low and high pressures, the co-adsorption of CO_2 is very low and the H_2O/CO_2 ratio is incredibly high, especially for FAU and EMT at 50 bar. Under these simulation circumstances and composition of the mixture, the adsorption of CO_2 can be considered negligible and will not shift the reaction equilibrium to the reactant side, according to Le Chatelier's Principle.

5.6. Evaluation of results

The figures 5.1 to 5.25 show that the hypotheses from chapter 2.1.5 stands. The adsorption in the zeolites increases with increasing pressure and decreases with increasing temperature. Since the lower temperature clearly shows better results than the higher temperature, the results will be evaluated at the lower temperature, which is 455 K. Table 5.1 shows the properties of the zeolites, corresponding to Table 1.1, but in the order of their adsorption capacity. In Table 5.2, two more properties are added, namely restricting channel diameter and the number of cages. The restricting channel diameter is the largest diameter with which a molecule can move through the zeolite. Certain molecules are small enough for the cavities in a zeolite, but too large for its channels. The restricting channel diameter denotes this limit. The number of cages is the number of cavities of the zeolite that are larger than its channels. Each zeolite has a largest cavity diameter, but some of those have the same size as their adjacent channels and are therefore not seen as cages.

The figures for the all-silica zeolites show that FAU has a high adsorption capacity for water, which is 174 g/kg-framework at 50 bar, followed by EMT (48 g/kg), JSR (35 g/kg) and IRR (35 g/kg). The other zeolites have an adsorption capacity below 20 g/kg-framework and nine of them around or below 10 g/kg-framework. At 40 bar, both JSR and IRR have a somewhat higher adsorption capacity than EMT. FAU still has the highest adsorption capacity. At lower pressures FAU, JSR and IRR start to have roughly the same adsorption capacity, followed by EMT and SBS.
The figures for the zeolites containing aluminum show a large increase in the adsorption capacity of water for all zeolites. FAU, IRR, JSR, SBS and EMT again have the highest capacity, and AFR, AFY, BPH and BEA the lowest. It can be seen that the rest of the order of adsorption capacity is also roughly equal to the one for the zeolites containing only silicon.

When evaluating this results, certain conclusions can be drawn. Firstly, whether zeolites have similar properties to FAU or internal and/or external pores does not seem decisive for their adsorption

capacity, since zeolites from all categories appear at random places in the order of Tables 5.1 and 5.2. Additionally, the restricting pore diameter is not crucial for the adsorption capacity. The tables show that larger diameters appear at the bottom of the adsorption capacity order, such as AFR, and smaller ones at the top, such as JSR. Secondly, large cavity diameters seem to play a role in the adsorption capacity, since zeolites with larger cavities (> 10 Å) appear at the top while the ones with smaller cavities (< 10 Å) appear at the bottom, with the exception of SAO and JSR. The almost exact same situation can be seen for the restricting channel diameter. It should be mentioned however, that some zeolites have narrow channels, even though their restricting channel diameter is large enough for the molecules to move through. For some cases, the molecules can move through the zeolites in one dimension, but not in the other because the channels are too narrow. Therefore, not all channels are accessible from every direction. This is the case for AFR, BEA, BOZ, SBE and SBS, which have some large channels, but also channels that are significantly smaller and therefore difficult or even impossible for the molecules to move through. Additionally, accessible pore volume is also important, since the zeolites where this property is low (AFR, BEA, BPH), appear at the bottom of the list and the ones where it is higher (JSR, IRR, FAU) appear at the top.
It is also noticeable that the zeolites with a large number of cages, such as FAU and JSR, have a high adsorption capacity, whilst the types that have few or no distinguishable cages have a low adsorption capacity, for example AFY and BPH. The size of the cage, so a large cavity diameter, seems to further enhance this trend. The exception on this is IRR, which has no cages but still a relatively high adsorption capacity, most likely due to its large channel size and large accessible pore volume.
When considering desorption, figures 5.26 to 5.33 show that all zeolites have an enthalpy of adsorption between -8 and -40 kJ/mol, which indicates that desorption is possible. For some zeolites, such as FAU, the enthalpy of adsorption decreases with increasing pressure, making desorption harder, but not impossible.

Table 5.1: Zeolite types for which the adsorption isotherms will be generated with RASPA simulations. The table shows the total volume, accessible pore volume, largest cavity diameter and restricting pore diameter for each zeolite.

Zeolites	**Vol. [Å^3]**	**Access. Pore Vol. [cm^3/g]**	**Largest Cavity D. [Å]**	**Restrict. Pore D. [Å]**
FAU	14428.771	0.3723	10.696	6.950
EMT	7207.302	0.3711	11.001	6.967
IRR	4422.866	0.4838	13.915	11.716
JSR	7815.473	0.4221	7.431	4.542
SBS	6997.151	0.3422	10.977	6.867
SBT	10501.091	0.3410	10.397	6.944
SAO	3948.063	0.3371	8.214	6.298
SBE	9320.777	0.3386	12.097	6.835
BOZ	7112.097	0.3558	8.305	4.518
ITT	3586.511	0.4094	12.771	11.602
BEA	4178.433	0.2716	6.118	5.634
BPH	1914.802	0.3023	9.108	5.614
AFY	1132.679	0.3380	7.422	5.502
AFR	2109.810	0.2618	7.816	6.573

Table 5.2: Zeolite types for which the adsorption isotherms will be generated with RASPA simulations. The table shows the total volume, accessible pore volume, largest cavity diameter and restricting pore diameter for each zeolite.

Zeolites	Restrict. Channel D. [Å]	Cages -	H_2O ad. 50 bar, 455 K [g/kg-framework]	H_2O ad. 50 bar, 455 K, Al [g/kg-framework]
FAU	10.696	8	174.011	244.988
EMT	11.001	6	47.946	196.116
IRR	13.915	0	34.641	231.436
JSR	7.431	8	34.592	227.742
SBS	10.977	2	16.329	206.434
SBT	10.397	4	14.769	184.213
SAO	8.206	0	11.499	156.674
SBE	12.097	1	10.751	158.534
BOZ	8.305	2	10.549	135.229
ITT	12.771	0	10.034	146.538
BEA	6.118	0	6.796	127.078
BPH	9.108	0	5.790	114.319
AFY	7.422	0	2.982	115.542
AFR	7.816	2	2.511	118.561

6
Conclusion

This study has examined which synthetic zeolites exhibit the highest suitability for water adsorption in the Sabatier reaction, and the specific properties that account for their superior performance. From the evaluation of the simulation results, several conclusions can be drawn in order to answer this question. Firstly, the increase of pressure increases the adsorption capacity of water in each zeolite. The capacity of other components increases until water becomes dominant and excludes the other components from the framework, after which their adsorption starts to decrease. The results show that in the pressure range of 10-50 bar, a pressure of 50 bar yields the highest water adsorption capacity for each zeolite type.
The increase of temperature from 455 K to 635 K has a negative effect on the adsorption of water in the zeolites, as it decreases rapidly. The other components experience a slight decrease in adsorption, but not as much as water. This is because water is less dominant in the framework and other component can therefore be adsorbed more easily.
Adding aluminum to the framework rapidly increases the adsorption of water compared to the all-silica frameworks. This is because the Al-O bonds and added cations create strong electrostatic fields that attract water, since it has a large dipole moment and is highly polar. This research shows that zeolites with an Si/Al ratio between 15-27 experience a large water adsorption increase with respect to their all-silica frameworks.
Additionally, all zeolites have an enthalpy of adsorption that indicates that desorption is possible.
The results show that the zeolites FAU, EMT, JSR, IRR and SBS have the highest adsorption capacity for water for all-silica frameworks and frameworks including aluminum. Of these five zeolite types, FAU shows the highest adsorption capacity for water. The zeolites AFR, AFY, BPH and BEA have the lowest water adsorption capacity.

The zeolite properties show that the restricting pore diameter is not crucial for the adsorption capacity, once the pores are large enough (> 5 Å) for each component to enter the zeolite. The combination of large cavity diameters and a high accessible pore volume seem to increase a zeolites water adsorption capacity. Furthermore, in some zeolites, molecules can move through the framework in one dimension, since the restricting channel size is larger than the molecule. However, in another direction, these channels are too narrow, which restricts the movement of molecules and has a decreasing effect on the water adsorption capacity. Additionally, the position of the channels, internal or external, is not crucial for the water adsorption capacity, since zeolites from each category show both higher and lower water adsorption capacities. Lastly, the number and size of cages in the zeolite is important for the water adsorption capacity. Zeolites that have many large cages show the highest adsorption capacity, such as FAU and JSR. This is because the adsorption of water attracts other water molecules, which leads to large stable water structures in the zeolites, excluding other components and attracting more water.
Based on these results, zeolites that have a high accessible pore volume, large channels and many large cages are expected to have a high water adsorption capacity. This can be further enhanced by adding aluminum up to an Si/Al ratio between 15-25, applying a pressure of 50 bar and a temperature of 455 K.

7
Recommendations

This chapter will give some recommendations for improvements on this and future research regarding zeolites and adsorption capacity, especially with regards to the Sabatier reaction.

Firstly, the results are acquired through computer simulations. Experimental research may give different results. Certain circumstances, such as pressure and temperature, are fixed in a simulation and cannot fluctuate. In an experimental set-up these circumstances might fluctuate due to the surroundings. Additionally, zeolite samples in an experiment can show irregularities that are not present in a simulation. The simulation uses the zeolite structure from iRASPA, which is the most ideal structure with no irregularities. This can also have an impact on the adsorption capacity of the zeolite. An experimental test to examine the adsorption capacity of the zeolites in this research can therefore lead to new insights or improvements on these results.

Secondly, this research is limited to certain types of zeolites, pressures and temperatures. A wider range of tests can show different results, in which certain zeolites that are not tested in this research could also have a high adsorption capacity. Also, different Si/Al ratios might prove that there is a limit to the number of aluminum atoms in the zeolite after which the water adsorption does no longer increase, or perhaps a limit to the pressure increase. Simulations or experiments that examine other pressures, temperatures, Si/Al ratios and zeolites can build upon the insights from this research.

Additionally, in this research the Sabatier reaction itself is not simulated, only the gas composition of the products. It can be interesting to see if or how both the composition and adsorption change if the reaction takes places inside the zeolite. The dispersion of the nickel catalyst in the framework could also have an influence on this. These aspects can be examined in an experimental set-up.

In conclusion, it is recommended to conduct the tests in this report in an experimental set-up, to see how it differs from the simulations. Additionally, certain properties such as pressure, temperature, Si/Al ratio and the zeolite types can be extended in future research. Also, artificial zeolites can be created using the most beneficial properties found in this research for water adsorption for application in the Sabatier reaction.

References

[1] Ck-12. *What is the molar mass of H2O?* URL: https://www.ck12.org/flexi/chemistry/molar-mass/what-is-the-molar-mass-of-h2o/#:~:text=Step%206%3A%20Calculate%20%2D%20Using%20the,is%20approximately%2018.016%20g%2Fmol..

[2] Aristizabal-González et al. "Ammonia Adsorption at High Temperature and Pressure Using Sodium Containing Aluminosilicates: Selectivity over Nitrogen and Multicycle Working Capacities". In: *Industrial & Engineering Chemistry Research* 64.7 (2025), pp. 4027–4039. DOI: 10.1021/acs.iecr.4c04621. URL: https://doi.org/10.1021/acs.iecr.4c04621.

[3] International Zeolite Association. *Database of Zeolite Structures*. 2017. URL: https://www.iza-structure.org/databases/.

[4] M H Azad. "Sorption enhanced Methanation of Carbon Dioxide Experimental research of nickel modified zeolites for sorption enhanced CO2 methanation". MA thesis. URL: http://repository.tudelft.nl/..

[5] Peng Bai, Michael Tsapatsis, and J. Ilja Siepmann. "TraPPE-zeo: Transferable potentials for phase equilibria force field for all-silica zeolites". In: *Journal of Physical Chemistry C* 117 (46 Nov. 2013), pp. 24375–24387. ISSN: 19327447. DOI: 10.1021/jp4074224.

[6] Rachael L. Baumann and John L. Falconer. *Peng-Robinson Equation of State for Mixtures*. 2016. URL: https://demonstrations.wolfram.com/PengRobinsonEquationOfStateForMixtures/.

[7] Rachael L. Baumann, John L. Falconer, and Nick Bongiardina. *Fugacity from Equation of State for Water*. 2015. URL: https://demonstrations.wolfram.com/FugacityFromEquationOfStateForWater/.

[8] Alison Biester, Sébastien Dementin, and Catherine L Drennan. *Visualizing the gas channel of a monofunctional carbon monoxide dehydrogenase*. URL: https://pmc.ncbi.nlm.nih.gov/articles/PMC9093221/#:~:text=The%20kinetic%20diameters%20for%20xenon,to%20CO2%20%5B33%5D..

[9] Chemical Book. *1318-02-1(Zeolite) Product Description*. 2017. URL: https://www.chemicalbook.com/ChemicalProductProperty_US_CB6330194.aspx.

[10] Ecyclopeadia Britannica. *Zeolite*. June 2025. URL: https://www.britannica.com/science/zeolite.

[11] *Chemical Properties of Hydrogen*. 2007. URL: https://www.chemeo.com/cid/17-951-7/Hydrogen.

[12] LibreTexts Chemistry. *Lennard-Jones Potentail*. URL: https://chem.libretexts.org/Bookshelves/Physical_and_Theoretical_Chemistry_Textbook_Maps/Supplemental_Modules_(Physical_and_Theoretical_Chemistry)/Physical_Properties_of_Matter/Atomic_and_Molecular_Properties/Intermolecular_Forces/Specific_Interactions/Lennard-Jones_Potential.

[13] Grevil Colaco. *A Monte Carlo Simulation Study on Adsorption of Nitrogen Oxides (NOx) in zeolites*. Tech. rep. 2020. URL: http://repository.tudelft.nl/..

[14] Larry Coleman. *Critical Properties and Acentric Factor*. URL: https://eng.libretexts.org/Bookshelves/Chemical_Engineering/Distillation_Science_(Coleman)/03%3A_Critical_Properties_and_Acentric_Factor#:~:text=The%20term%20%E2%80%9Cacentric%20factor%E2%80%9D%20comes,has%20an%20%CF%89%20of%200.248..

[15] Coolprop. *CarbonDioxide*. URL: https://coolprop.org/fluid_properties/fluids/CarbonDioxide.html.

[16] Coolprop. *Water*. URL: https://coolprop.org/fluid_properties/fluids/Water.html.

[17] *Critical Points for some substances*. 2005. URL: https://www.engineeringtoolbox.com/critical-point-d_997.html.

[18] R Delmelle et al. *Development of improved nickel catalysts for sorption enhanced CO2 methanation*. Tech. rep. 2016. URL: https://www.elsevier.com/open-access/userlicense/1.0/.

[19] Ron Dror. *Energy functions and their relationship to molecular conformation*. Tech. rep. 2019. URL: https://web.stanford.edu/class/archive/cs/cs279/cs279.1202/lectures/lecture3-annot.pdf.

[20] Shuo Duan et al. "Comparative analysis of CO2 and N2 adsorption on zeolite 4A: Thermodynamics parameters and site energy distribution investigations". In: *Journal of Environmental Chemical Engineering* 12 (3 June 2024). ISSN: 22133437. DOI: 10.1016/j.jece.2024.112870.

[21] David Dubbeldam et al. "RASPA: Molecular simulation software for adsorption and diffusion in flexible nanoporous materials". In: *Molecular Simulation* 42 (2 Jan. 2016), pp. 81–101. ISSN: 10290435. DOI: 10.1080/08927022.2015.1010082.

[22] Rachel E. Fletcher, Sanliang Ling, and Ben Slater. "Violations of Löwenstein's rule in zeolites". In: *Chemical Science* 8 (11 2017), pp. 7483–7491. ISSN: 20416539. DOI: 10.1039/c7sc02531a.

[23] Daan Frenkel and Berend Smit. *Understanding Molecular Simulation From Algorithms to Applications*. University of Amsterdam, 2023.

[24] Friend, Ely, and Ingham. *Tables for the Thermodphysical properties of Methane*. Tech. rep. 1989.

[25] Almudena García-Sánchez et al. "Transferable force field for carbon dioxide adsorption in zeolites". In: *Journal of Physical Chemistry C* 113 (20 May 2009), pp. 8814–8820. ISSN: 19327447. DOI: 10.1021/jp810871f.

[26] Fatemeh Gholipour and Masoud Mofarahi. "Adsorption equilibrium of methane and carbon dioxide on zeolite 13X: Experimental and thermodynamic modeling". In: *Journal of Supercritical Fluids* 111 (May 2016), pp. 47–54. ISSN: 08968446. DOI: 10.1016/j.supflu.2016.01.008.

[27] Michael A. Gottlieb and Rudolf Pfeiffer. *Electrostatic Energy*. 2013. URL: https://www.feynmanlectures.caltech.edu/II_08.html.

[28] G Granitsiotis. "Methanation of Carbon Dioxide Experimental research of separation en-hanced methanation of CO 2". MA thesis. TU Delft, 2017. URL: http://repository.tudelft.nl/..

[29] G Granitsiotis. “Methanation of Carbon Dioxide Experimental research of separation en-hanced methanation of CO 2”. MA thesis. URL: http://repository.tudelft.nl/..

[30] David Herring and Rebecca Lindsay. *What evidence exists that Earth is warming and that humans are the main cause?* Oct. 2022. URL: https://www.climate.gov/news-features/climate-qa/what-evidence-exists-earth-warming-and-humans-are-main-cause.

[31] J. van Kampen. “Efficient carbon utilization to dimethyl ether by steam adsorption enhancement”. PhD thesis. TU Eindhoven, 2021.

[32] *KNMI broeikasgassen*. URL: https://www.knmi.nl/kennis-en-datacentrum/uitleg/broeikasgas-kooldioxide.

[33] Computational Research Division of the Lawrence Berkeley National laboratory. *Zeo++*. URL: https://www.zeoplusplus.org/about.html.

[34] Sarah Lee. *Grand Canonical Ensemble Essentials*. June 2025. URL: https://www.numberanalytics.com/blog/essentials-grand-canonical-ensemble-thermodynamics.

[35] E. W. Lemmon et al. *NIST Standard Reference Database 23: Reference Fluid Thermodynamic and Transport Properties-REFPROP, Version 10.0, National Institute of Standards and Technology*. 2018. DOI: https://doi.org/10.18434/T4/1502528. URL: https://www.nist.gov/srd/refprop.

[36] Grazia Leonzio. “Process analysis of biological Sabatier reaction for bio-methane production”. In: *Chemical Engineering Journal* 290 (Apr. 2016), pp. 490–498. ISSN: 13858947. DOI: 10.1016/j.cej.2016.01.068.

[37] Xianfeng Li et al. “Adsorption and desorption characteristics of hydrophobic hierarchical zeolites for the removal of volatile organic compounds”. In: *Chemical Engineering Journal* 411 (May 2021). ISSN: 13858947. DOI: 10.1016/j.cej.2021.128558.

[38] Rebecca Lindsay. *Climate change: atmospheric carbon dioxide*. May 2025. URL: https://www.climate.gov/news-features/understanding-climate/climate-change-atmospheric-carbon-dioxide.

[39] Marcus G. Martin, Aidan P. Thompson, and Tina M. Nenoff. “Effect of pressure, membrane thickness, and placement of control volumes on the flux of methane through thin silicalite membranes: A dual control volume grand canonical molecular dynamics study”. In: *Journal of Chemical Physics* 114 (16 Apr. 2001), pp. 7174–7181. ISSN: 00219606. DOI: 10.1063/1.1360256.

[40] Masterclass. *What Is the Sabatier Reaction? Learn How Astronauts Create Water and Oxygen in Space*. Sept. 2021. URL: https://www.hydrogennewsletter.com/methanation-of-co2-to-ch4-using-h2-through-sabatier-reaction/.

[41] Adam Merril. *Zeolites Statistics and Information*. URL: https://www.usgs.gov/centers/national-minerals-information-center/zeolites-statistics-and-information#:~:text=Zeolites%20are%20hydrated%20aluminosilicates%20of,services%20page%20for%20more%20information..

[42] *Methane*. URL: https://globalmethane.org/methane/index.aspx.

[43] Moran et al. *Principles of Engineering Thermodynamics*. 8th ed. Wiley, 2012.

[44] Moran et al. *Property tables and charts (SI units)*.

[45] Manash Protim Mudoi, Pushpa Sharma, and Abhimanyu Singh Khichi. *A review of gas adsorption on shale and the influencing factors of CH4 and CO2 adsorption*. Oct. 2022. DOI: 10.1016/j.petrol.2022.110897.

[46] Hydrogen Newsletter. *Methanation of CO2 to CH4 Using H2 through Sabatier Reaction: A Comprehensive Technical Guide*. Oct. 2023. URL: https://www.masterclass.com/articles/what-is-the-sabatier-reaction.

[47] NIST. *REFPROP Documentation*. Tech. rep. 2018. URL: https://www.nist.gov/system/files/documents/2018/05/23/refprop10a.pdf.

[48] PubChem. *Methane*. URL: https://pubchem.ncbi.nlm.nih.gov/compound/Methane.

[49] Y. A. Ran et al. “RASPA3: A Monte Carlo code for computing adsorption and diffusion in nanoporous materials and thermodynamics properties of fluids”. In: *The Journal of Chemical Physics* 161 (11 Sept. 2024). ISSN: 0021-9606. DOI: 10.1063/5.0226249. URL: https://pubs.aip.org/jcp/article/161/11/114106/3312873/RASPA3-A-Monte-Carlo-code-for-computing-adsorption.

[50] Michael Ruth. *Le Chatelier’s principle*. 2023. URL: https://www.ebsco.com/research-starters/history/le-chateliers-principle#:~:text=Le%20Chatelier's%20principle%20is%20a,scientific%20inquiry%20and%20practical%20applications..

[51] Shrinjay Sharma et al. “Understanding shape selectivity effects of hydroisomerization using a reaction equilibrium model”. In: *Journal of Chemical Physics* 160 (21 June 2024). ISSN: 10897690. DOI: 10.1063/5.0209210.

[52] TES. *Molecules, mass, and finding the right energy balance: A deeper look into the methanation process*. Feb. 2024. URL: https://tes-h2.com/blog/molecules-mass-and-finding-the-right-energy-balance-a-deeper-look-into-the-methanation-process.

[53] The Engineering Toolbox. *Methane (CH4): Thermophysical Properties and Phase Diagram*. 2008. URL: https://www.engineeringtoolbox.com/methane-d_1420.html.

[54] The Engineering Toolbox. *Water vs. Steam - Critical and Triple Points*. 2008. URL: https://www.engineeringtoolbox.com/critical-point-water-steam-d_834.html.

[55] Robert Virta. *Mineral Resource of the Month: Zeolites*. Oct. 2014. URL: https://www.earthmagazine.org/article/mineral-resource-month-zeolites/.

[56] Liangyuan Wei et al. “Can bi-functional nickel modified 13X and 5A zeolite catalysts for CO2 methanation be improved by introducing ruthenium?” In: *Molecular Catalysis* 494 (Oct. 2020). ISSN: 24688231. DOI: 10.1016/j.mcat.2020.111115.

[57] Liangyuan Wei et al. “Influence of nickel precursors on the properties and performance of Ni impregnated zeolite 5A and 13X catalysts in CO2 methanation”. In: *Catalysis Today* 362 (Feb. 2021), pp. 35–46. ISSN: 09205861. DOI: 10.1016/j.cattod.2020.05.025.

[58] Chris Woodford. *Zeolites*. Aug. 2023. URL: https://www.explainthatstuff.com/zeolites.html.

[59] Ke Zhang et al. “Adsorption of water and ethanol in MFI-type zeolites”. In: *Langmuir* 28 (23 June 2012), pp. 8664–8673. ISSN: 07437463. DOI: 10.1021/la301122h.

A

Gas composition & Fugacity coefficients

This appendix shows the fugacity coefficients for each component at T = 455 K and T = 635 K, determined using RefProp [35].

Table A.1: Fugacity coefficient of water, methane, carbon dioxide and hydrogen at $T = 455$ K in the pressure range 10 - 50 bar [35].

Pressure [bar]	ϕ **Water (H_2O)**	ϕ **Methane (CH_4)**	ϕ **Carbon dioxide (CO_2)**	ϕ **Hydrogen (H_2)**
10	0.94674	1.0251	1.0013	1.0953
20	0.89371	1.0546	0.99951	1.2093
30	0.841	1.0891	1.0004	1.3466
40	0.7886	1.13	1.0043	1.5144
50	0.7365	1.1785	1.0117	1.7224

Table A.2: Fugacity coefficient of water, methane, carbon dioxide and hydrogen at $T = 635$ K in the pressure range 10 - 50 bar [35].

Pressure [bar]	ϕ **Water (H_2O)**	ϕ **Methane (CH_4)**	ϕ **Carbon dioxide (CO_2)**	ϕ **Hydrogen (H_2)**
10	0.98403	1.0083	1.0054	1.0275
20	0.96802	1.0173	1.0079	1.0568
30	0.95209	1.0266	1.0107	1.0876
40	0.93627	1.0363	1.0138	1.1197
50	0.92054	1.0465	1.0171	1.1534

Table A.3: Gas compositions of the mixture with water, methane, carbon dioxide and hydrogen at $T = 455$ K in the pressure range 10 - 50 bar [35].

Pressure [bar]	y **Water (H_2O)**	y **Methane (CH_4)**	y **Carbon dioxide (CO_2)**	y **Hydrogen (H_2)**
10	0.6657	0.33280089	0.00029911	0.0012
20	0.666	0.33297042	0.00020592	0.00082366
30	0.66611	0.33310126	0.00015775	0.00063099
40	0.6662	0.33317219	0.00012556	0.00050225
50	0.6663	0.33319231	0.00010154	0.00040615

Table A.4: Gas composition for the mixture with water, methane, carbon dioxide and hydrogen at $T = 635$ K in the pressure range 10 - 50 bar [35].

Pressure [bar]	y **Water (H_2O)**	y **Methane (CH_4)**	y **Carbon dioxide (CO_2)**	y **Hydrogen (H_2)**
10	0.659	0.3295	0.0023	0.0092
20	0.661	0.3305	0.0017	0.0068
30	0.662	0.331	0.0014	0.0056
40	0.6626	0.3313	0.0012	0.0049
50	0.6631	0.3315	0.0011	0.0043

B
Peng-Robinson Equation of State

This appendix shows the Peng-Robinson Equation of State for mixtures [6].

For a component i in a mixture:

$$a_i(T) = 0.45724 \frac{R^2 T_{c,i}^2}{P_{c,i}} \alpha_i(T) \tag{B.1}$$

$$b_i = 0.0778 \frac{R T_{c,i}}{P_{c,i}} \tag{B.2}$$

$$\alpha_i(T) = [1 + m_i(1 - \sqrt{T_{r,i}})]^2 \tag{B.3}$$

With:

$$T_{r,i} = \frac{T}{T_{c,i}} \tag{B.4}$$

And:

$$m_i = 0.37464 + 1.54226\omega_i - 0.26992\omega_i^2 \tag{B.5}$$

Then the mixing rules are:

$$a_{\text{mix}} = \sum_i \sum_j x_i x_j a_{ij} \tag{B.6}$$

With:

$$a_{ij} = (1 - k_{ij})\sqrt{a_i a_j} \tag{B.7}$$

$$b_{\text{mix}} = \sum_i x_i b_i \tag{B.8}$$

The Peng-Robinson Equation of State is:

$$P = \frac{RT}{V_m - b_{\text{mix}}} - \frac{a_{\text{mix}}}{V_m(V_m + b_{\text{mix}}) + b_{\text{mix}}(V_m - b_{\text{mix}})} \tag{B.9}$$

Working with compressibility factor Z:

$$Z = \frac{PV_m}{RT} \tag{B.10}$$

And defining reduced EoS parameters A & B:

$$A = \frac{a_{\text{mix}} P}{R^2 T^2} \tag{B.11}$$

$$B = \frac{b_{\text{mix}} P}{RT} \tag{B.12}$$

Then Z is determined using the cubic equation:

$$Z^3 - (1 - B)Z^2 + (A - 3B^2 - 2B)Z - (AB - B^2 - B^3) = 0 \tag{B.13}$$

The fugacity coefficient ϕ_i for component i can then be determined using:

$$\ln \phi_i = \frac{b_i}{b_{\text{mix}}}(Z - 1) - \ln(Z - B) - \frac{A}{2\sqrt{2}B}\left(\frac{2\sum_j x_j a_{ij}}{a_{\text{mix}}} - \frac{b_i}{b_{\text{mix}}}\right)\ln\left(\frac{Z + (1 + \sqrt{2})B}{Z + (1 - \sqrt{2})B}\right) \tag{B.14}$$

C
Enthalpy & Entropy

Table C.1: Thermodynamic properties for each component at T = 455 K. $\overline{h_f^\circ}$ is evaluated at T = 298.15 K and P = 1 atm [44] [24].

Property	**Component**			
	CH_4	H_2O	CO_2	H_2
$\overline{h_f^\circ}$ [kJ/kmol]	-74850	-241820	-393520	0
$\Delta\overline{h}$ [kJ/kmol]	16208	15254	15699.5	13032.75
$\overline{s}$ [kJ/kmol·K]	202.94	203.116	230.669	142.862

Table C.2: Thermodynamic properties for each component at T = 635 K. $\overline{h_f^\circ}$ is evaluated at T = 298.15 K and P = 1 atm [44] [24].

Property	**Component**			
	CH_4	H_2O	CO_2	H_2
$\overline{h_f^\circ}$ [kJ/kmol]	-74850	-241820	-393520	0
$\Delta\overline{h}$ [kJ/kmol]	24931	21678.5	23949.5	18306.375
$\overline{s}$ [kJ/kmol·K]	219.19	214.996	245.903	152.626

D

Python script silicon to aluminum

```
from porran import PORRAN
# Create a PORRAN object
prn = PORRAN()


# Read the input file. We will use the zeolite method to create the structure graph
# This will create a graph of the structure based on Si-O-Si bonds.
prn.init_structure('BEA.cif', graph_method='zeolite', mask_method='zeolite')


# Random structures obeying the Löwenstein rule
random_strcts = prn.generate_structures(n_structures=2, n_subs=3, replace_algo='random_lowenstein',
create_algo='zeolite', write=True, writepath='Structures/random_lowenstein')

# Rename one of the new structure files to 'Zeolite_2.cif'


from ase.io import read, write
import numpy as np


# ====== USER INPUT ======
input_cif = "BEA_2.cif" # Input CIF file name
output_cif = "zeolite_relabelled.cif" # Output CIF file name
cutoff = 2.1 # Maximum Al–O bond length (in Å)

# ==========================

# Read structure
atoms = read(input_cif)
symbols = atoms.get_chemical_symbols()


# Identify indices of Al and O atoms
al_indices = [i for i, s in enumerate(symbols) if s.lower() == "al"]
o_indices = [i for i, s in enumerate(symbols) if s.lower() == "o"]


# Track which O atoms are bonded to Al
o_al_bonded = set()
```

```
# Loop over all Al–O pairs and check distance
for i in al_indices:
    for j in o_indices:
        dist = atoms.get_distance(i, j, mic=True)
        if dist <= cutoff:
            o_al_bonded.add(j)



# — Build custom labels —
custom_labels = []
custom_types = []
for i, symbol in enumerate(symbols):
    if i in o_al_bonded:
        custom_labels.append(f"Oa{i+1}") # label
        custom_types.append("Oa") # type
    else:
        custom_labels.append(f"{symbol}{i+1}")
        custom_types.append(symbol)



# — Write CIF using ASE —
write(output_cif, atoms)



# — Post-process CIF to replace both type_symbol and label —
with open(output_cif, 'r') as f:
    lines = f.readlines()



with open(output_cif, 'w') as f:
    atom_index = 0
    for line in lines:
        stripped = line.strip()
        if stripped == "" or stripped.startswith("_") or stripped.startswith("loop_"):
            f.write(line)
            continue



        parts = line.split()
        if len(parts) >= 6: # assume this is an atom line
            parts[0] = custom_types[atom_index] # _atom_site_type_symbol
            parts[1] = custom_labels[atom_index] # _atom_site_label
            atom_index += 1
            f.write(" ".join(parts) + "")
        else:
            f.write(line)



print(f"Relabelled {len(o_al_bonded)} oxygen atoms as Oa.")
print(f"New CIF saved as: {output_cif}")
```

E

Simulation results

Table E.1: H_2O adsorption (g/kg-framework) at T = 455 K, all-silica frameworks.

Zeolite	Pressure [bar]				
	10	20	30	40	50
BOZ	1.645	3.458	5.557	8.045	10.553
FAU	2.282	5.721	11.707	34.594	173.996
JSR	2.853	6.660	12.113	21.911	34.603
SBT	1.834	4.203	7.850	9.213	14.771
AFY	0.641	1.273	1.853	2.481	2.981
BPH	1.033	2.168	3.357	4.597	5.793
IRR	2.192	4.906	8.474	14.581	34.647
ITT	1.417	3.052	4.843	6.836	10.038
AFR	0.485	0.985	1.592	2.186	2.511
BEA	0.554	2.389	3.664	5.483	6.799
EMT	1.558	3.514	6.073	9.758	47.932
SAO	1.500	3.291	5.437	8.166	11.505
SBE	1.394	2.991	4.979	7.381	10.759
SBS	1.590	3.590	6.082	10.301	16.338

Table E.2: CH_4 adsorption (g/kg-framework) at T = 455 K, all-silica frameworks.

Zeolite	Pressure [bar]				
	10	20	30	40	50
BOZ	0.845	1.680	2.510	3.332	4.156
FAU	1.611	3.209	4.708	5.561	1.949
JSR	2.189	4.289	6.338	8.113	9.551
SBT	1.138	2.239	3.289	3.313	4.041
AFY	0.087	0.190	0.287	0.398	0.521
BPH	0.314	0.645	0.966	1.306	1.663
IRR	1.033	2.103	3.113	4.144	4.868
ITT	0.483	0.986	1.499	1.997	2.541
AFR	0.147	0.286	0.443	0.615	0.787
BEA	0.238	1.001	1.504	2.013	2.553
EMT	0.802	1.627	2.443	3.218	3.201
SAO	0.752	1.486	2.220	2.957	3.682
SBE	0.561	1.126	1.689	2.270	2.829
SBS	0.833	1.649	2.481	3.279	4.052

Table E.3: CO_2 adsorption (g/kg-framework) at T = 455 K, all-silica frameworks.

Zeolite	Pressure [bar]				
	10	20	30	40	50
BOZ	$2.07 \cdot 10^{-3}$	$3.34 \cdot 10^{-3}$	$5.81 \cdot 10^{-3}$	$3.98 \cdot 10^{-3}$	$4.54 \cdot 10^{-3}$
FAU	$5.95 \cdot 10^{-3}$	$1.01 \cdot 10^{-2}$	$1.05 \cdot 10^{-2}$	$9.77 \cdot 10^{-3}$	$4.35 \cdot 10^{-3}$
JSR	$9.69 \cdot 10^{-3}$	$9.69 \cdot 10^{-3}$	$1.21 \cdot 10^{-2}$	$1.55 \cdot 10^{-2}$	$1.22 \cdot 10^{-2}$
SBT	$4.88 \cdot 10^{-3}$	$5.70 \cdot 10^{-3}$	$5.95 \cdot 10^{-3}$	$3.31 \cdot 10^{-3}$	$4.42 \cdot 10^{-3}$
AFY	$9.15 \cdot 10^{-4}$	$1.00 \cdot 10^{-10}$	$4.58 \cdot 10^{-4}$	$4.40 \cdot 10^{-4}$	$4.40 \cdot 10^{-4}$
BPH	$7.85 \cdot 10^{-4}$	$2.62 \cdot 10^{-4}$	$5.23 \cdot 10^{-4}$	$1.57 \cdot 10^{-3}$	$7.85 \cdot 10^{-4}$
IRR	$2.82 \cdot 10^{-3}$	$3.94 \cdot 10^{-3}$	$5.49 \cdot 10^{-3}$	$2.68 \cdot 10^{-3}$	$5.07 \cdot 10^{-3}$
ITT	$1.12 \cdot 10^{-3}$	$1.91 \cdot 10^{-3}$	$2.23 \cdot 10^{-3}$	$1.91 \cdot 10^{-3}$	$1.91 \cdot 10^{-3}$
AFR	$2.29 \cdot 10^{-4}$	$6.87 \cdot 10^{-4}$	$6.87 \cdot 10^{-4}$	$4.58 \cdot 10^{-4}$	$4.40 \cdot 10^{-4}$
BEA	$4.81 \cdot 10^{-3}$	$2.06 \cdot 10^{-3}$	$2.29 \cdot 10^{-3}$	$2.63 \cdot 10^{-3}$	$1.49 \cdot 10^{-3}$
EMT	$2.29 \cdot 10^{-3}$	$3.36 \cdot 10^{-3}$	$3.97 \cdot 10^{-3}$	$4.12 \cdot 10^{-3}$	$3.74 \cdot 10^{-3}$
SAO	$2.49 \cdot 10^{-3}$	$4.06 \cdot 10^{-3}$	$4.32 \cdot 10^{-3}$	$3.40 \cdot 10^{-3}$	$3.27 \cdot 10^{-3}$
SBE	$2.06 \cdot 10^{-3}$	$2.75 \cdot 10^{-3}$	$2.98 \cdot 10^{-3}$	$3.26 \cdot 10^{-3}$	$2.69 \cdot 10^{-3}$
SBS	$2.90 \cdot 10^{-3}$	$3.51 \cdot 10^{-3}$	$4.12 \cdot 10^{-3}$	$3.82 \cdot 10^{-3}$	$4.12 \cdot 10^{-3}$

Table E.4: H_2 adsorption (g/kg-framework) at T = 455 K, all-silica frameworks.

Zeolite	Pressure [bar]				
	10	20	30	40	50
BOZ	$2.15 \cdot 10^{-4}$	$3.79 \cdot 10^{-4}$	$4.20 \cdot 10^{-4}$	$5.77 \cdot 10^{-4}$	$5.73 \cdot 10^{-4}$
FAU	$3.51 \cdot 10^{-4}$	$4.82 \cdot 10^{-4}$	$5.88 \cdot 10^{-4}$	$6.04 \cdot 10^{-4}$	$2.48 \cdot 10^{-4}$
JSR	$4.34 \cdot 10^{-4}$	$6.15 \cdot 10^{-4}$	$7.27 \cdot 10^{-4}$	$7.62 \cdot 10^{-4}$	$9.44 \cdot 10^{-4}$
SBT	$2.63 \cdot 10^{-4}$	$3.80 \cdot 10^{-4}$	$4.92 \cdot 10^{-4}$	$5.76 \cdot 10^{-4}$	$5.55 \cdot 10^{-4}$
AFY	$1.05 \cdot 10^{-4}$	$6.29 \cdot 10^{-5}$	$1.05 \cdot 10^{-4}$	$3.15 \cdot 10^{-4}$	$2.52 \cdot 10^{-4}$
BPH	$1.44 \cdot 10^{-4}$	$2.76 \cdot 10^{-4}$	$3.23 \cdot 10^{-4}$	$3.35 \cdot 10^{-4}$	$2.76 \cdot 10^{-4}$
IRR	$4.26 \cdot 10^{-4}$	$5.16 \cdot 10^{-4}$	$5.10 \cdot 10^{-4}$	$7.74 \cdot 10^{-4}$	$7.23 \cdot 10^{-4}$
ITT	$1.90 \cdot 10^{-4}$	$2.92 \cdot 10^{-4}$	$3.36 \cdot 10^{-4}$	$4.60 \cdot 10^{-4}$	$6.05 \cdot 10^{-4}$
AFR	$6.29 \cdot 10^{-5}$	$7.35 \cdot 10^{-5}$	$1.68 \cdot 10^{-4}$	$1.68 \cdot 10^{-4}$	$1.78 \cdot 10^{-4}$
BEA	$8.02 \cdot 10^{-4}$	$2.52 \cdot 10^{-4}$	$3.51 \cdot 10^{-4}$	$3.98 \cdot 10^{-4}$	$4.25 \cdot 10^{-4}$
EMT	$2.97 \cdot 10^{-4}$	$3.57 \cdot 10^{-4}$	$3.92 \cdot 10^{-4}$	$4.37 \cdot 10^{-4}$	$4.89 \cdot 10^{-4}$
SAO	$2.04 \cdot 10^{-4}$	$3.12 \cdot 10^{-4}$	$5.33 \cdot 10^{-4}$	$5.39 \cdot 10^{-4}$	$5.22 \cdot 10^{-4}$
SBE	$1.76 \cdot 10^{-4}$	$3.83 \cdot 10^{-4}$	$4.07 \cdot 10^{-4}$	$4.59 \cdot 10^{-4}$	$6.03 \cdot 10^{-4}$
SBS	$2.34 \cdot 10^{-4}$	$4.13 \cdot 10^{-4}$	$4.79 \cdot 10^{-4}$	$5.45 \cdot 10^{-4}$	$5.73 \cdot 10^{-4}$

Table E.5: H_2O adsorption (g/kg-framework) at T = 635 K, all-silica frameworks.

Zeolite	Pressure [bar]				
	10	20	30	40	50
BOZ	0.789	1.572	2.368	3.138	3.851
FAU	1.043	2.093	3.179	4.245	5.305
JSR	1.222	2.464	3.661	4.843	6.033
SBT	0.780	1.560	2.341	3.124	3.941
AFY	0.378	0.774	1.151	1.497	1.849
BPH	0.555	1.086	1.599	2.076	2.628
IRR	1.120	2.261	3.405	4.512	5.703
ITT	0.787	1.580	2.392	3.147	3.939
AFR	0.314	0.623	0.893	1.179	1.480
BEA	0.542	1.101	1.644	2.178	2.705
EMT	0.797	1.578	2.390	3.184	3.982
SAO	0.744	1.491	2.199	2.922	3.668
SBE	0.719	1.425	2.137	2.824	3.536
SBS	0.785	1.588	2.370	3.135	3.915

Table E.6: CH_4 adsorption (g/kg-framework) at T = 635 K, all-silica frameworks.

Zeolite	Pressure [bar]				
	10	20	30	40	50
BOZ	0.356	0.723	1.070	1.404	1.752
FAU	0.664	1.339	1.987	2.622	3.267
JSR	0.786	1.576	2.369	3.124	3.832
SBT	0.384	0.777	1.151	1.539	1.915
AFY	0.073	0.150	0.214	0.287	0.362
BPH	0.174	0.360	0.526	0.696	0.857
IRR	0.527	1.061	1.561	2.086	2.608
ITT	0.290	0.578	0.855	1.160	1.436
AFR	0.104	0.211	0.311	0.418	0.516
BEA	0.241	0.478	0.702	0.950	1.171
EMT	0.394	0.784	1.170	1.550	1.927
SAO	0.350	0.711	1.060	1.397	1.714
SBE	0.288	0.571	0.867	1.146	1.427
SBS	0.389	0.780	1.160	1.533	1.916

Table E.7: CO_2 adsorption (g/kg-framework) at T = 635 K, all-silica frameworks.

Zeolite	Pressure [bar]				
	10	20	30	40	50
BOZ	$7.00 \cdot 10^{-3}$	$1.10 \cdot 10^{-2}$	$1.30 \cdot 10^{-2}$	$1.41 \cdot 10^{-2}$	$1.92 \cdot 10^{-2}$
FAU	$1.55 \cdot 10^{-2}$	$2.54 \cdot 10^{-2}$	$3.06 \cdot 10^{-2}$	$3.41 \cdot 10^{-2}$	$3.67 \cdot 10^{-2}$
JSR	$1.84 \cdot 10^{-2}$	$2.68 \cdot 10^{-2}$	$3.49 \cdot 10^{-2}$	$3.81 \cdot 10^{-2}$	$4.18 \cdot 10^{-2}$
SBT	$7.48 \cdot 10^{-3}$	$1.35 \cdot 10^{-2}$	$1.46 \cdot 10^{-2}$	$1.67 \cdot 10^{-2}$	$2.03 \cdot 10^{-2}$
AFY	$1.00 \cdot 10^{-10}$	$1.83 \cdot 10^{-3}$	$2.75 \cdot 10^{-3}$	$9.15 \cdot 10^{-4}$	$4.58 \cdot 10^{-4}$
BPH	$2.88 \cdot 10^{-3}$	$7.32 \cdot 10^{-3}$	$4.18 \cdot 10^{-3}$	$4.45 \cdot 10^{-3}$	$6.54 \cdot 10^{-3}$
IRR	$1.00 \cdot 10^{-2}$	$1.68 \cdot 10^{-2}$	$2.08 \cdot 10^{-2}$	$2.44 \cdot 10^{-2}$	$2.70 \cdot 10^{-2}$
ITT	$4.62 \cdot 10^{-3}$	$7.64 \cdot 10^{-3}$	$1.03 \cdot 10^{-2}$	$1.16 \cdot 10^{-2}$	$1.08 \cdot 10^{-2}$
AFR	$1.14 \cdot 10^{-3}$	$1.83 \cdot 10^{-3}$	$2.52 \cdot 10^{-3}$	$2.52 \cdot 10^{-3}$	$1.60 \cdot 10^{-3}$
BEA	$4.58 \cdot 10^{-3}$	$8.12 \cdot 10^{-3}$	$8.35 \cdot 10^{-3}$	$1.01 \cdot 10^{-2}$	$1.05 \cdot 10^{-2}$
EMT	$9.84 \cdot 10^{-3}$	$1.28 \cdot 10^{-2}$	$1.51 \cdot 10^{-2}$	$1.81 \cdot 10^{-2}$	$1.98 \cdot 10^{-2}$
SAO	$8.37 \cdot 10^{-3}$	$1.14 \cdot 10^{-2}$	$1.15 \cdot 10^{-2}$	$1.54 \cdot 10^{-2}$	$1.60 \cdot 10^{-2}$
SBE	$5.72 \cdot 10^{-3}$	$9.44 \cdot 10^{-3}$	$9.73 \cdot 10^{-3}$	$1.14 \cdot 10^{-2}$	$1.45 \cdot 10^{-2}$
SBS	$7.70 \cdot 10^{-3}$	$1.11 \cdot 10^{-2}$	$1.62 \cdot 10^{-2}$	$2.02 \cdot 10^{-2}$	$1.77 \cdot 10^{-2}$

Table E.8: H_2 adsorption (g/kg-framework) at T = 635 K, all-silica frameworks.

Zeolite	Pressure [bar]				
	10	20	30	40	50
BOZ	$1.05 \cdot 10^{-3}$	$1.57 \cdot 10^{-3}$	$1.93 \cdot 10^{-3}$	$2.40 \cdot 10^{-3}$	$2.66 \cdot 10^{-3}$
FAU	$1.42 \cdot 10^{-3}$	$2.03 \cdot 10^{-3}$	$2.57 \cdot 10^{-3}$	$3.11 \cdot 10^{-3}$	$3.29 \cdot 10^{-3}$
JSR	$1.54 \cdot 10^{-3}$	$2.29 \cdot 10^{-3}$	$3.01 \cdot 10^{-3}$	$3.37 \cdot 10^{-3}$	$4.16 \cdot 10^{-3}$
SBT	$1.14 \cdot 10^{-3}$	$1.65 \cdot 10^{-3}$	$2.01 \cdot 10^{-3}$	$2.35 \cdot 10^{-3}$	$2.71 \cdot 10^{-3}$
AFY	$3.98 \cdot 10^{-4}$	$8.39 \cdot 10^{-4}$	$7.55 \cdot 10^{-4}$	$9.44 \cdot 10^{-4}$	$1.15 \cdot 10^{-3}$
BPH	$8.63 \cdot 10^{-4}$	$1.02 \cdot 10^{-3}$	$1.35 \cdot 10^{-3}$	$1.63 \cdot 10^{-3}$	$1.87 \cdot 10^{-3}$
IRR	$1.61 \cdot 10^{-3}$	$2.21 \cdot 10^{-3}$	$3.06 \cdot 10^{-3}$	$3.52 \cdot 10^{-3}$	$3.58 \cdot 10^{-3}$
ITT	$9.56 \cdot 10^{-4}$	$1.61 \cdot 10^{-3}$	$2.25 \cdot 10^{-3}$	$2.45 \cdot 10^{-3}$	$2.71 \cdot 10^{-3}$
AFR	$5.03 \cdot 10^{-4}$	$6.61 \cdot 10^{-4}$	$7.86 \cdot 10^{-4}$	$7.03 \cdot 10^{-4}$	$1.01 \cdot 10^{-3}$
BEA	$8.07 \cdot 10^{-4}$	$1.23 \cdot 10^{-3}$	$1.42 \cdot 10^{-3}$	$1.60 \cdot 10^{-3}$	$2.00 \cdot 10^{-3}$
EMT	$1.17 \cdot 10^{-3}$	$1.49 \cdot 10^{-3}$	$1.99 \cdot 10^{-3}$	$2.45 \cdot 10^{-3}$	$2.66 \cdot 10^{-3}$
SAO	$1.02 \cdot 10^{-3}$	$1.42 \cdot 10^{-3}$	$1.95 \cdot 10^{-3}$	$2.22 \cdot 10^{-3}$	$2.71 \cdot 10^{-3}$
SBE	$1.05 \cdot 10^{-3}$	$1.40 \cdot 10^{-3}$	$1.89 \cdot 10^{-3}$	$2.19 \cdot 10^{-3}$	$2.47 \cdot 10^{-3}$
SBS	$1.06 \cdot 10^{-3}$	$1.66 \cdot 10^{-3}$	$2.16 \cdot 10^{-3}$	$2.26 \cdot 10^{-3}$	$2.74 \cdot 10^{-3}$

Table E.9: H_2O adsorption (g/kg-framework) at T = 455 K, frameworks incl. aluminum.

Zeolite	Pressure [bar]				
	10	20	30	40	50
BOZ	64.563	83.602	91.767	111.865	135.229
JSR	70.499	111.629	142.766	203.553	227.742
FAU	76.044	131.551	192.017	232.573	244.988
SBT	74.428	105.559	138.461	151.283	184.213
AFY	79.071	90.249	82.058	96.657	115.542
BPH	49.536	59.035	64.754	70.560	114.319
IRR	59.730	81.295	98.622	164.499	231.436
ITT	68.680	75.490	109.340	112.517	146.538
AFR	98.794	97.497	102.745	98.421	118.561
BEA	65.757	89.084	103.094	108.678	127.078
EMT	83.690	101.931	133.159	189.146	196.116
SAO	92.370	112.203	127.770	141.315	156.675
SBE	69.710	88.714	119.572	143.813	158.534
SBS	86.604	115.156	152.395	183.343	206.434

Table E.10: CH_4 adsorption (g/kg-framework) at T = 455 K, frameworks incl. aluminum.

Zeolite	Pressure [bar]				
	10	20	30	40	50
BOZ	0.652	1.170	1.544	1.770	2.010
JSR	1.741	2.838	3.597	2.912	2.599
FAU	1.433	1.945	1.445	0.865	0.692
SBT	0.661	1.055	1.208	1.475	1.245
AFY	0.071	0.095	0.220	0.178	0.254
BPH	0.258	0.473	0.686	0.914	0.789
IRR	0.938	1.788	2.405	2.360	1.833
ITT	0.400	0.772	0.922	1.188	1.171
AFR	0.084	0.172	0.237	0.411	0.434
BEA	0.375	0.574	0.739	0.866	0.834
EMT	0.626	1.148	1.278	1.036	1.004
SAO	0.541	0.945	1.184	1.507	1.490
SBE	0.445	0.777	0.926	0.950	1.016
SBS	0.614	1.081	1.147	1.049	0.869

Table E.11: CO_2 adsorption (g/kg-framework) at T = 455 K, frameworks incl. aluminum.

Zeolite	Pressure [bar]				
	10	20	30	40	50
BOZ	$2.664 \cdot 10^{-3}$	$5.642 \cdot 10^{-3}$	$5.407 \cdot 10^{-3}$	$3.918 \cdot 10^{-3}$	$3.761 \cdot 10^{-3}$
JSR	$1.585 \cdot 10^{-2}$	$1.788 \cdot 10^{-2}$	$1.360 \cdot 10^{-2}$	$7.589 \cdot 10^{-3}$	$8.190 \cdot 10^{-3}$
FAU	$1.477 \cdot 10^{-2}$	$1.350 \cdot 10^{-2}$	$8.287 \cdot 10^{-3}$	$4.950 \cdot 10^{-3}$	$3.262 \cdot 10^{-3}$
SBT	$4.297 \cdot 10^{-3}$	$5.147 \cdot 10^{-3}$	$5.297 \cdot 10^{-3}$	$4.247 \cdot 10^{-3}$	$3.598 \cdot 10^{-3}$
AFY	$1.00 \cdot 10^{-10}$	$1.00 \cdot 10^{-10}$	$1.00 \cdot 10^{-10}$	$1.00 \cdot 10^{-10}$	$1.00 \cdot 10^{-10}$
BPH	$2.582 \cdot 10^{-4}$	$1.033 \cdot 10^{-3}$	$2.065 \cdot 10^{-3}$	$1.033 \cdot 10^{-3}$	$1.291 \cdot 10^{-3}$
IRR	$4.583 \cdot 10^{-3}$	$4.722 \cdot 10^{-3}$	$5.972 \cdot 10^{-3}$	$7.222 \cdot 10^{-3}$	$3.611 \cdot 10^{-3}$
ITT	$2.037 \cdot 10^{-3}$	$2.351 \cdot 10^{-3}$	$2.977 \cdot 10^{-3}$	$1.724 \cdot 10^{-3}$	$1.097 \cdot 10^{-3}$
AFR	$4.475 \cdot 10^{-4}$	$1.00 \cdot 10^{-10}$	$6.712 \cdot 10^{-4}$	$1.0 \cdot 10^{-10}$	$2.237 \cdot 10^{-4}$
BEA	$3.375 \cdot 10^{-3}$	$2.250 \cdot 10^{-3}$	$1.912 \cdot 10^{-3}$	$1.350 \cdot 10^{-3}$	$2.250 \cdot 10^{-3}$
EMT	$3.893 \cdot 10^{-3}$	$5.240 \cdot 10^{-3}$	$5.764 \cdot 10^{-3}$	$4.716 \cdot 10^{-3}$	$2.994 \cdot 10^{-3}$
SAO	$4.233 \cdot 10^{-3}$	$4.233 \cdot 10^{-3}$	$4.361 \cdot 10^{-3}$	$3.078 \cdot 10^{-3}$	$3.591 \cdot 10^{-3}$
SBE	$2.700 \cdot 10^{-3}$	$4.444 \cdot 10^{-3}$	$2.981 \cdot 10^{-3}$	$3.150 \cdot 10^{-3}$	$2.700 \cdot 10^{-3}$
SBS	$4.492 \cdot 10^{-3}$	$5.989 \cdot 10^{-3}$	$5.390 \cdot 10^{-3}$	$3.593 \cdot 10^{-3}$	$3.294 \cdot 10^{-3}$

Table E.12: H_2 adsorption (g/kg-framework) at T = 635 K, frameworks incl. aluminum.

Zeolite	Pressure [bar]				
	10	20	30	40	50
BOZ	$1.795 \cdot 10^{-4}$	$2.549 \cdot 10^{-4}$	$3.339 \cdot 10^{-4}$	$3.375 \cdot 10^{-4}$	$3.626 \cdot 10^{-4}$
JSR	$3.305 \cdot 10^{-4}$	$4.200 \cdot 10^{-4}$	$4.545 \cdot 10^{-4}$	$2.582 \cdot 10^{-4}$	$2.651 \cdot 10^{-4}$
FAU	$2.663 \cdot 10^{-4}$	$2.594 \cdot 10^{-4}$	$1.959 \cdot 10^{-4}$	$1.168 \cdot 10^{-4}$	$9.107 \cdot 10^{-5}$
SBT	$1.992 \cdot 10^{-4}$	$2.518 \cdot 10^{-4}$	$2.725 \cdot 10^{-4}$	$2.633 \cdot 10^{-4}$	$2.083 \cdot 10^{-4}$
AFY	$6.151 \cdot 10^{-5}$	$1.230 \cdot 10^{-4}$	$1.845 \cdot 10^{-4}$	$1.026 \cdot 10^{-4}$	$1.436 \cdot 10^{-4}$
BPH	$1.774 \cdot 10^{-4}$	$1.065 \cdot 10^{-4}$	$2.602 \cdot 10^{-4}$	$2.484 \cdot 10^{-4}$	$2.484 \cdot 10^{-4}$
IRR	$3.245 \cdot 10^{-4}$	$4.263 \cdot 10^{-4}$	$4.137 \cdot 10^{-4}$	$4.391 \cdot 10^{-4}$	$3.563 \cdot 10^{-4}$
ITT	$1.508 \cdot 10^{-4}$	$3.088 \cdot 10^{-4}$	$3.447 \cdot 10^{-4}$	$4.164 \cdot 10^{-4}$	$3.518 \cdot 10^{-4}$
AFR	$1.025 \cdot 10^{-5}$	$6.151 \cdot 10^{-5}$	$1.026 \cdot 10^{-4}$	$9.227 \cdot 10^{-5}$	$1.230 \cdot 10^{-4}$
BEA	$7.216 \cdot 10^{-5}$	$1.856 \cdot 10^{-4}$	$1.804 \cdot 10^{-4}$	$2.577 \cdot 10^{-4}$	$1.598 \cdot 10^{-4}$
EMT	$2.401 \cdot 10^{-4}$	$3.018 \cdot 10^{-4}$	$2.710 \cdot 10^{-4}$	$2.058 \cdot 10^{-4}$	$2.161 \cdot 10^{-4}$
SAO	$1.646 \cdot 10^{-4}$	$2.057 \cdot 10^{-4}$	$2.586 \cdot 10^{-4}$	$2.410 \cdot 10^{-4}$	$1.528 \cdot 10^{-4}$
SBE	$2.140 \cdot 10^{-4}$	$2.680 \cdot 10^{-4}$	$2.552 \cdot 10^{-4}$	$2.242 \cdot 10^{-4}$	$2.346 \cdot 10^{-4}$
SBS	$1.818 \cdot 10^{-4}$	$2.127 \cdot 10^{-4}$	$2.230 \cdot 10^{-4}$	$2.332 \cdot 10^{-4}$	$1.303 \cdot 10^{-4}$